

MICRO RAMAN/PL INVESTIGATIONS OF MATERIALS FOR IR AND PV
APPLICATIONS (III-V TYPE II SUPERLATTICES AND II-VI COMPOUNDS)

by

Henan Liu

A dissertation submitted to the faculty of
The University of North Carolina at Charlotte
in partial fulfillment of the requirements
for the degree of Doctor of Philosophy in
Optical Science and Engineering

Charlotte

2015

Approved by

Dr. Yong Zhang

Dr. Vasily Astratov

Dr. M. Yasin Akhtar Raja

Dr. Sheng-Guo Wang

©2015
Henan Liu
ALL RIGHTS RESERVED

ABSTRACT

HENAN LIU. Micro Raman/PL investigations of materials for IR and PV applications
(III-V type II superlattices and II-VI compounds).
(Under the direction of DR. YONG ZHANG)

Raman and photoluminescence (PL) spectroscopy are two of the major spectroscopic techniques that are currently used in studies on solid state materials. Raman spectroscopy, which is based on Raman scattering process, is widely used in characterizing structures, determining compositions, and probing various types of excitations of the material, etc. On the other hand, PL spectroscopy is closely related to the generation and re-combination of photo-generated carriers, thus usually used in determining electronic structure near the fundamental band gap, studying impurities and defects, and so on. Apparently, these two techniques enable material research regarding different aspects, which are both vital for understanding the material properties. Despite the difference in physical principles on which they are based, these two techniques share the same feature of being invasive, which is preferable or mandatory in many of the applications. Furthermore, these two techniques are usually integrated in a single experimental instrument which is commercially available: for instance, a Raman spectroscopy microscope system. These days, the spatial resolution of a confocal optical system can reach the sub-micron range with appropriately choosing excitation wavelength, thus making micro-Raman and micro-PL measurements available. Apparently, this high resolution is making the Raman and PL measurements more effective when studying materials, which also enables related analyses with a sub-micron spatial accuracy.

In our work, we conduct micro-Raman or micro-PL spectroscopic investigations on several types of solid state materials, which are all playing significant roles in IR detection and/or PV applications. These materials, in general, fall into three categories: (1) Type II Superlattices (T2SLs) based on InAs/GaSb; (2) T2SLs based on InAs/InAsSb; and (3) CdTe single crystalline epilayers with varying defect density levels. The first two types of materials could be regarded to form one material system, since these two T2SLs are both model systems from the aspect of lattice vibrational properties of semiconductor SLs, where the study of their phonon modes is far from adequate and completed. On the other hand, CdTe, by itself, form another material system. Although being a rather “well-known” semiconductor material when compared to the two T2SLs, the study on defects in CdTe is still developing and far from being complete. In short, for these materials, investigations regarding structural properties and defect behaviors are of great interest, for either theory or application field. These related studies are vital in understanding the physics of the material or assessing the material quality. Correspondingly, micro-Raman and micro-PL technique are extraordinarily suitable for these investigations: the former is a powerful tool in structural characterization, while the latter is extensively used in defect-related studies.

In the study of InAs/GaSb and InAs/InAsSb T2SLs, micro-Raman spectroscopy is used as the major tool to study the lattice vibrations and explore the phonon modes. Several new phonon modes have been observed, which for the first time confirms the existence of three distinctly different types of phonon modes (confined, quasi-confined, and extended modes) that have long been predicted theoretically but never experimentally identified. In the study of CdTe, spatially resolved micro-PL spectroscopy is used to investigate the effects of extended defects in the epilayers with high density defects. By comparison with

XRD and chemical etching method, the PL method have generally show consistent results, and also exhibiting higher sensitivity in revealing defects that are actually detrimental to radiative recombination of photo-generated carriers. For the first time, we have been able to make direct comparison between etch pits and PL dark spots, and identified three different scenarios when correlating the results of the two characterization tools.

DEDICATION

This dissertation is dedicated to my father and mother.

ACKNOWLEDGEMENTS

I am very grateful to Prof. Yong Zhang for his academic supervision through all my PhD study. During these years of study, I am always inspired by his rigorous thinking, as well as the great enthusiasm in material research work. I appreciate very much the valuable suggestions and advices from my committee members, Prof. Vasily Astratov, Prof. Yasin Raja, and Prof. Sheng-Guo Wang. I would like to thank all of our collaborators, from University of Illinois at Urbana–Champaign (Prof. Shun Lien Chuang’ group), Arizona State University (Prof. Yong-Hang Zhang’s group), Georgia Institute of Technology (Prof. Russell D. Dupuis’s group), and Army Research Lab (Dr. Yuanping Chen), who have prepared the samples studied in this dissertation work. I am thankful for the financial support offered by MURI project from ARO, as well as the GASP financial award and GPSP financial support offered by University of North Carolina at Charlotte. Without the kindly encouragement and support from my family, friends and fellow group members, this dissertation work would not have been possible.

TABLE OF CONTENTS

LIST OF TABLES	xii
LIST OF FIGURES	xiii
CHAPTER 1: INTRODUCTION	1
1.1 Fundamentals of Raman Spectroscopy	1
1.1.1 Basics of Raman Spectroscopy	1
1.1.2 General Physical Principles of Raman Scattering	4
1.2 PL Technique: Fundamental Principles and Applications	11
1.3 Fundamentals of InAs/GaSb T2SLs	12
1.3.1 InAs/GaSb T2SL: A Model System	12
1.3.2 InAs/GaSb T2SL or Heterostructure: Applications	17
1.3.3 Raman Selection Rules for InAs/GaSb T2SL	18
1.3.4 Theoretical Predictions on Phonon Spectra of InAs/GaSb T2SLs	24
1.3.5 A Brief Review on Previous Raman Studies on InAs/GaSb T2SLs	25
1.4 Fundamentals of InAs/InAsSb T2SL	27
1.4.1 InAs/InAsSb T2SL: A Model System	27
1.4.2 Raman Selection Rules for InAs/InAsSb T2SLs	28
1.4.3 Previous Raman Study on InAsSb Alloys	30
1.5 Fundamentals of CdTe Epilayers	33
1.5.1 General Information and Applications	33
1.5.2 Study of Extended Defects in CdTe Epilayers	34
1.6 The Objectives of This Dissertation	37

CHAPTER 2: SAMPLES AND EXPERIMENTAL METHODS	39
2.1 Sample Information and Sample Preparation	39
2.1.1 InAs/GaSb and InAs/InAsSb T2SLs	39
2.1.2 Samples Information: CdTe Epilayers	45
2.2 Horiba LabRam HR 800 Confocal Micro-Raman Microscope	46
2.2.1 The Advantage of Confocal Microscope System	46
2.2.2 Horiba LabRam HR 800 Confocal Micro-Raman System: General Information	46
2.2.3 Detailed Information for Optics Components in Optical Compartments	49
2.3 Data Calibration and Processing	55
2.3.1 Frequency Calibration	55
2.3.2 Intensity Calibration	55
2.4 Other Techniques	59
CHAPTER 3: RAMAN STUDY ON LATTICE VIBRATION MODES IN InAs/GaSb T2SLS	61
3.1 An Overview	61
3.2 Experimental Details for Raman Measurements	62
3.3 Some General Observations and Comments	65
3.4 Micro-Raman Investigation on Lattice Vibration Modes in InAs/GaSb T2SLs	75
3.4.1 (001) Back-scattering	75
3.4.2 (110) and $(\bar{1}10)$ Cleaved Edge Back-scattering	80
3.5 High Power Effects	86
3.6 Conclusions	88

CHAPTER 4: RAMAN STUDY ON LATTICE VIBRATION MODES IN InAs/InAsSb T2SLS	90
4.1 Overview	90
4.2 General Observations and Comments	90
4.3 Micro-Raman Investigation on Lattice Vibration Modes in InAs/InAsSb T2SLs	98
4.3.1 (001) Backscattering	98
4.3.2 (110) Cleaved Edge Back-scattering	105
4.3.3 Comparison with InAs/GaSb T2SLs	110
4.4 Conclusions	111
CHAPTER 5: PL STUDY ON EXTENDED DEFECTS IN CdTe EPILAYERS	113
5.1 An Overview	113
5.2 Experimental Procedures	114
5.3 General PL Results and Discussion	115
5.4 Direct Comparison between PL Dark Spots and Etch Pits	119
5.5 Conclusions	123
CHAPTER 6: CONCLUSIONS AND FUTURE WORK	124
6.1 Conclusions	124
6.1.1 Micro-Raman Study on Lattice Vibrations in InAs/GaSb T2SLs and InAs/ InAsSb T2SLs	124
6.1.2 Micro-PL Study on Extended Defects in CdTe Epilayers	127
6.2 Future Work	128
6.2.1 Micro-Raman Study on InAs/InAsSb T2SLs	128
6.2.2 Micro-PL Study on Defects in Semiconductor Epilayers	128
REFERENCES	130

APPENDIX: LIST OF PUBLICATIONS AND PRESENTATIONS

LIST OF TABLES

TABLE 1.1: Polarization selection rules for C_{2v} Raman modes in back-scattering geometries.	21
TABLE 1.2: Polarization selection rules for T_d Raman modes in back-scattering geometries.	21
TABLE 1.3: Polarization selection rules for D_{2d} Raman modes in back-scattering geometries.	29
TABLE 2.1: Sample information for (3-2122, 3-2130, 3-2154 and 3-2155) series SL samples, grown by MOCVD.	40
TABLE 2.2: Sample information for (IFA, IFRA, and IFRB) series SL samples, grown by MBE.	42
TABLE 2.3: Sample information for (3-2287, 3-2289, 3-2295) series InAs/InAsSb SL samples, grown by MOCVD.	43
TABLE 2.4: Sample information for (B1854, B1775, B1871, B1816, B1818) series InAs/InAsSb SL samples, grown by MBE.	43
TABLE 2.5: Sample information for (B1784, B1810, B1814) series InAsSb alloy samples, grown by MBE.	44
TABLE 2.6: Characterization results of CdTe epilayers grown on Si (211) wafers.	46
TABLE 3.1: Possible polarization configurations in (001), (110) and $(\bar{1}10)$ back-scattering geometries.	63
TABLE 4.1: Anisotropy results for InAs/InAsSb T2SL and InAsSb alloy samples.	105
TABLE 5.1 Summary of characterization results of CdTe epilayers grown on Si-(211) substrates.	116

LIST OF FIGURES

FIGURE 1.1: Representative diagrams of energy transitions in Stokes Raman, anti-Stokes Raman, Resonance Raman, and Rayleigh scattering [12].	6
FIGURE 1.2: Schematic graph showing the alignments of the conduction and valence band edges at the interface for (a) AlAs/GaAs heterostructure (Type I straddling lineup), (b) InAs/GaSb heterostructure (Type II broken lineup) [32,40].	13
FIGURE 1.3: Schematic graph showing the lattice of InAs/GaSb T2SL grown along [001] direction.	15
FIGURE 1.4: Representative graph showing the state conditions for both semi-metal and semiconductor behavior of the InAs/GaSb T2SL [32].	16
FIGURE 1.5: Representative graph showing the geometric relations of the lattice planes.	19
FIGURE 1.6: Typical back-scattering Raman spectrum of InAs/GaSb T2SL from (001) plane, as reported in the literature [38].	26
FIGURE 1.7: Typical back-scattering Raman spectrum of InAs _{1-x} Sb _x alloys from (001) plane, as reported in [75].	32
FIGURE 2.1: Photo of HR 800 Raman system showing the front interface.	47
FIGURE 2.2: Schematic diagram showing light propagation inside the Raman system.	49
FIGURE 2.3: Polarization directions selected by polarizer and analyzer inside the optical compartment of the Raman system.	55
FIGURE 3.1: Polarization configurations in back-scattering polarized Raman measurements conducted on (a) (001) plane; and (b) (110) and $\bar{1}\bar{1}0$ plane.	63
FIGURE 3.2: Comparing (001) back-scattering Raman spectra of InAs/GaSb SL sample G54, under four polarization configurations: (a) $z'(x', x')\bar{z}'$ and $z'(x', y')\bar{z}'$, and (b) $z'(y', y')\bar{z}'$ and $z'(y', x')\bar{z}'$.	66
FIGURE 3.3: Comparing (001) back-scattering Raman spectra in polarization configurations $z'(x', x')\bar{z}'$ and $z'(x', y')\bar{z}'$ for bulk materials: (a) InAs, and (b) GaSb.	67

- FIGURE 3.4: Raman spectra and mapping result from the (110) cleaved edge of an InAs/GaSb SL sample grown on InAs substrate (G55). 69
- FIGURE 3.5: Comparing (110) back-scattering Raman spectra of InAs/GaSb SL sample G54, under four polarization configurations: (a) $x'(y', z')\bar{x}'$ and $x'(y', y')\bar{x}'$; and (b) $x'(z', z')\bar{x}'$ and $x'(z', y')\bar{x}'$. 70
- FIGURE 3.6: Comparing (110) back-scattering Raman spectra of InAs and GaSb bulk epilayers, in different polarization configurations: (a) InAs: $x'(y', y')\bar{x}'$ and $x'(y', z')\bar{x}'$; (b) InAs: $x'(z', y')\bar{x}'$ and $x'(z', z')\bar{x}'$; (c) GaSb: $x'(y', y')\bar{x}'$ and $x'(y', z')\bar{x}'$; (d) GaSb: $x'(z', y')\bar{x}'$ and $x'(z', z')\bar{x}'$. 72
- FIGURE 3.7: Raman spectra comparison for InAs/GaSb SL samples on the same substrate, obtained in $z'(x', x')\bar{z}'$: (a) SL on GaSb substrate, involving sample IFA, IFRA and IFRB; and (b) SL on InAs substrate, involving sample G22, G30, G54 and G55. 73
- FIGURE 3.8: (001) backscattering Raman spectra of InAs/GaSb SLs, compared with those of InAs and GaSb thick epilayers in two polarization configurations: (a) $z'(x', x')\bar{z}'$ and (b) $z'(x', y')\bar{z}'$. 75
- FIGURE 3.9: Comparison of Raman spectra measured in configuration HH and VV for (a) SL G55, (b) SL IFRA, (c) thick InAs epilayer, and (d) thick GaSb epilayer. 79
- FIGURE 3.10: Comparing (110) back-scattering Raman spectra for the same samples as in Figure 3.8, in four polarization configurations: (a) $x'(y', z')\bar{x}'$, (b) $x'(z', y')\bar{x}'$, (c) $x'(y', y')\bar{x}'$ and (d) $x'(z', z')\bar{x}'$. 81
- FIGURE 3.11: Comparison of spectra obtained in different polarization configurations, for (a) SL on InAs and (b) SL on GaSb substrate. 84
- FIGURE 3.12: Comparison of Raman spectra measured from two cleaved edges (110) and $\bar{1}10$ for: (a) SL G54, (b) SL IFA, (c) thick GaSb epilayer, and (d) SL IFRA. 85
- FIGURE 3.13: Comparing $x'(y', y')\bar{x}'$ spectra by D1 and D2 laser excitation, for (a) SL G54, (b) SL IFA, (c) InAs bulk, and (d) GaSb bulk. 87
- FIGURE 4.1: Comparing (001) back-scattering Raman spectra of InAsSb alloy (B1784), under four polarization configurations: (a) $z'(x', x')\bar{z}'$ and $z'(x', y')\bar{z}'$, and (b) $z'(y', y')\bar{z}'$ and $z'(y', x')\bar{z}'$. 91
- FIGURE 4.2: Comparing (001) back-scattering Raman spectra of InAs/InAsSb SL (B1871), under the same condition as in Figure 4.1. 92

- FIGURE 4.3: Comparing (110) back-scattering Raman spectra of InAs/InAsSb SL (B1871), in polarization configurations: (a) $x'(y', z')\bar{x}'$, (b) $x'(y', y')\bar{x}'$, (c) $x'(z', z')\bar{x}'$, and (d) $x'(z', y')\bar{x}'$. 94
- FIGURE 4.4: Comparing (110) back-scattering Raman spectra of InAs/InAsSb alloy (B1784), in configurations: (a) $x'(y', z')\bar{x}'$, (b) $x'(y', y')\bar{x}'$, (c) $x'(z', z')\bar{x}'$ and (d) $x'(z', y')\bar{x}'$. 96
- FIGURE 4.5: Comparison on Raman spectra for MBE InAs/InAsSb SL samples B1854, B1775, B1816, and B1871, in polarization configuration $x'(y', z')\bar{x}'$. 98
- FIGURE 4.6: (001) back-scattering Raman spectra of InAs/InAsSb SLs, compared with those of InAs bulk and InAsSb alloys in two polarization configurations: (a) $z'(x', x')\bar{z}'$ and (b) $z'(x', y')\bar{z}'$. 99
- FIGURE 4.7: Frequency for the LO mode resolved in InAs/InAsSb SL and InAsSb alloy samples, in (001) back-scattering geometry. 101
- FIGURE 4.8: Comparing (001) back-scattering Raman spectra of InAs/InAsSb SLs, among sample B1775, B1816 and B1818 in polarization configurations: (a) $z'(x', x')\bar{z}'$ and (b) $z'(x', y')\bar{z}'$. 103
- FIGURE 4.9: Comparing Raman spectra to explore the anisotropy between $[110]$ and $[\bar{1}10]$, for: (a) SL B1775 and (b) SL B1816. 104
- FIGURE 4.10: Comparing (110) back-scattering Raman spectra for the same samples as in Figure 4.6, in four polarization configurations: (a) $x'(y', z')\bar{x}'$, (b) $x'(z', y')\bar{x}'$, (c) $x'(y', y')\bar{x}'$ and (d) $x'(z', z')\bar{x}'$. 106
- FIGURE 4.11: Mode frequency for the TO mode due to InAs and InSb alloying, resolved in InAs/InAsSb SL samples and InAsSb alloy samples, in (110) back-scattering geometry. 107
- FIGURE 4.12: Comparing (110) back-scattering Raman spectra of InAs/InAsSb SLs, among SL samples B1775, B1816 and B1818 in polarization configurations: (a) $x'(y', z')\bar{x}'$, (b) $x'(z', y')\bar{x}'$, (c) $x'(y', y')\bar{x}'$ and (d) $x'(z', z')\bar{x}'$. 110
- FIGURE 5.1: PL intensity maps of CdTe epilayers with different annealing cycles N : (a) $N=0$, (b) $N=2$, (c) $N=4$, (d) $N=6$, (e) $N=8$, and (f) $N=10$. 115
- FIGURE 5.2: Optical image for samples with different annealing cycles N : (a) $N=0$, (b) $N=2$, (c) $N=4$, (d) $N=6$, (e) $N=8$, and (f) $N=10$. 117

FIGURE 5.3: Histogram plots of the PL mapping data shown in Figure 5.1.	118
FIGURE 5.4: Optical image (under 100× objective lens) for sample 32607.	119
FIGURE 5.5: Comparison of PL intensity mapping (before etching) with SEM image (after etching) for sample 032607 ($N=8$).	120

CHAPTER 1: INTRODUCTION

In this chapter, we present background information regarding Raman and PL techniques, as well as the materials under investigation. In section 1.1, we present background information for Raman spectroscopy, introducing its physical principle and Raman selection rules. In section 1.2, we present background information for PL spectroscopy. The basic information of the three types of materials under examination is presented in sections 1.3 – 1.5. In section 1.6, we briefly present the objectives of this dissertation.

1.1 Fundamentals of Raman Spectroscopy

1.1.1 Basics of Raman Spectroscopy

(1) A first glimpse

Raman scattering, by which Raman spectroscopy is based on, refers to one type of inelastic scattering of photons. This scattering process was named after Chandrasekhra Venkata Raman, who discovered the phenomenon in liquids in 1928 [1]. Compared with Rayleigh scattering, which is an elastic scattering process, the intensity of Raman scattering is much weaker: the intensity is usually $\sim 10^{-5}$ of the incident light. Nevertheless, efforts have never been discontinued, which intend to better understand this process, as well as develop related techniques such that people can utilize the phenomenon to study and examine materials more efficiently. Today, Raman spectroscopy has become one of the major spectroscopic techniques that is being used to investigate materials of varying

complexities. Generally, Raman spectroscopy could work on any types of materials that consist of molecules. Thus, there is no limitation on the phase of the material to be examined: by carefully preparation and processing, Raman signals could be obtained from solids, powders, liquids, and even gases [2-6].

(2) Energy transition in Raman scattering process

When photon, or light is incident at a material, interaction happens between the two. During this light-matter interaction, energy transfers take place: the energy could either transfer from the photon to the material, or vice versa. Usually, the energy transfer corresponds to an energy transition inside the material. In other words, an excitation inside the material is created or absorbed by those incident photons. In Raman spectroscopy, we are able to observe various types of excitations such as phonons, excitons [7], polaritons, [8-11] etc. By tracking the energy transfer between light and material, we obtain fingerprint information regarding the excitations, thus reach the aim of investigating the material.

The energy transfer could be described by formula (1.1), where E_1 and E_2 represents energy state of the material before and after the light-material interaction, respectively. On the other hand, E_i and E_s represents the energy of the incident and scattered photon, respectively.

$$\Delta E = E_2 - E_1 = E_i - E_s \quad (1.1)$$

If the energy difference ΔE goes to zero, then the scattering process is elastic, for which Rayleigh scattering is a typical example; otherwise, the process is inelastic, for which Raman scattering is one of its examples. In Raman spectroscopy, the quantity to be directly concerned is the one referred to as frequency shift or Raman shift, $\Delta\omega$, typically

measured in wavenumber (cm^{-1}). It shows the energy transfer during the scattering process, and is directly proportional to ΔE , with the relationship expressed by the following formula:

$$\Delta E = h\Delta\nu = h\Delta\left(\frac{c}{\lambda}\right) = hc\Delta\omega \quad (1.2)$$

In general, various kinds of commonly used spectroscopic techniques are intended to measure ΔE , in either direct or indirect ways. These techniques include Raman spectroscopy, gamma-ray spectroscopy, microwave spectroscopy, and nuclear magnetic resonance spectroscopy, etc. In actual measurements, the range of ΔE varies for different techniques. For instance, Raman spectroscopy measures $\Delta\omega$ in the range of 10^1 - 10^4 cm^{-1} , while Gamma-ray spectroscopy measures $\Delta\omega$ in the range of 10^{10} - 10^{18} cm^{-1} .

(3) Stokes Raman scattering and anti-Stokes Raman scattering

As was mentioned, energy could be transferred from material to light, or vice versa. Thus, ΔE could either be positive or negative, in Raman scattering process. By concerning the frequency change of the incident and scattered light, we have the following formula:

$$\Delta E = hc\Delta\omega = h(\nu_i - \nu_s) \quad (1.3)$$

where ν_i and ν_s represent the frequency for the incident and scattered light, respectively. If $\Delta\omega$ is positive, then energy is transferred from light to material, and the process is called Stokes scattering. On the other hand, if $\Delta\omega$ is negative, then energy is transferred from material to light, and the process is named as anti-Stokes scattering. In the former process, the scattered light is red-shifted as compared to the incident light. In the latter process, however, the scattered light is blue-shifted. According to Maxwell-Boltzmann distribution law, at room temperature, the possibility of anti-Stokes scattering is much smaller than that of Stokes scattering. As temperature increases, anti-Stokes scattering is more likely to take place.

1.1.2 General Physical Principles of Raman Scattering

Throughout this dissertation, Raman spectroscopy has been used to study the lattice vibration modes of the material. Thus, we only present fundamental results of Raman principles related to lattice vibrations, from theories based on both classical physics and quantum mechanics. Firstly, we will briefly summarize the results of quantum treatments when dealing with the vibration of a diatomic molecule, thus provide an introductory understanding of vibrations, from the perspective of quantum mechanics. Secondly, we will present general results regarding vibrations from the perspective of classical physics. This introduction of classical treatments is indispensable, as it will be helpful in understanding the molecule (or crystal lattice, in a more general sense) vibrations in a more vivid way. In addition, we will also present an introduction of Raman selection rules from the classical view [12], and the Raman tensor method [13], which are extensively used in Raman studies in this dissertation.

(1) A quantum mechanics treatment: vibrations and normal vibration modes

To start with, firstly we present the results of a molecule consisting of two atoms. In quantum mechanics, the vibration of this molecule could be regarded as the motion of a single particle [14,15]: the particle has a reduce mass of μ , and a potential as V , which are expressed in the following formulas:

$$\mu = m_1 m_2 / (m_1 + m_2) \quad (1.4)$$

$$V = 2\pi^2 \nu_0^2 \mu q_0^2 \sin^2(2\pi \nu_0 t + \varphi) \quad (1.5)$$

where m_1, m_2 refers to the mass of the two atoms, respectively. q_0 is the amplitude of vibration of the system, ν_0 is the vibration frequency, and φ as a phase constant. To work out the vibrational levels for the molecule, one need to solve the following Schrödinger

equation, where K stands for a force constant that describes the bonding of the two atoms: (the potential V given above cannot yield the energy eigenstates given below, which is valid for a harmonic oscillator with the potential given in the equation below)

$$\frac{d^2\psi}{dq^2} + \frac{8\pi^2\mu}{h^2} \left(E - \frac{1}{2}Kq^2 \right) \psi = 0 \quad (1.6)$$

The solutions are a set of eigenfunctions, each of which is associated with an eigenvalue as shown below:

$$E_v = hv(n + 1/2), n = 0,1,2, \dots \quad (1.7)$$

$$v = \frac{1}{2\pi} \sqrt{\frac{K}{\mu}} \quad (1.8)$$

where n is the vibrational quantum number, the change in which indicates an energy transition inside the material has taken place. At room temperature, the transition of $n = 0 \rightarrow 1$ corresponds to the most possible transition in Stokes Raman scattering process. During this process, it is assumed that the molecule is firstly promoted to a “virtual” state, then relaxed into the first excited vibrational state.

As a special case, Resonance Raman happens when the energy of incident light is close to the energy difference between two electronic states of the material under investigation. Compared to normal Raman process, Resonance Raman tends to give much higher intensities, thus may be beneficial for investigations of some materials, especially when the concentration of the material is relatively low [16-18]. For a comparison regarding the energy transitions in Stokes Raman, anti-Stokes Raman, Resonance Raman, as well as Rayleigh scattering, we can refer to Figure 1.1 [12], which shows the diagrammatic representations for all these four processes. Note that E_0 and E_1 represent the

ground and first excited electronic states, respectively. The Arabic numerals 0~3 label different vibrational states, while V and V' represent vibrational states for E_0 and E_1 , respectively. The “virtual” state is represented by dotted line.

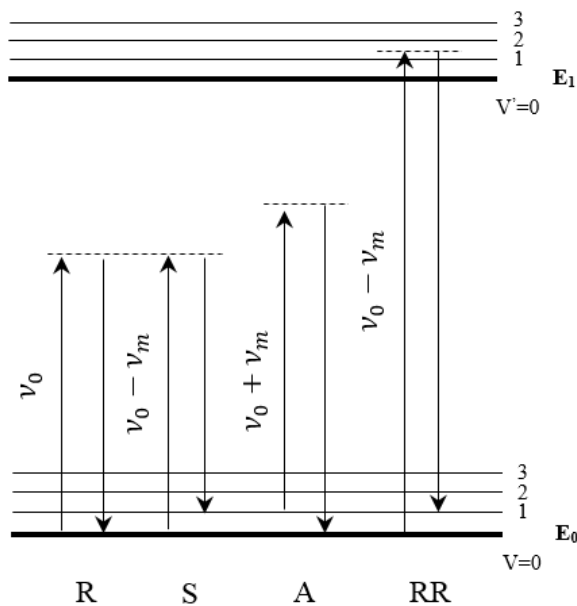


Figure 1.1: Representative diagrams of energy transitions in Stokes Raman, anti-Stokes Raman, Resonance Raman, and Rayleigh scattering [12]. In this figure, “R” represents Rayleigh scattering, “S” represents Stokes Raman, “A” represents anti-Stokes Raman, and “RR” represents Resonance Raman.

As a special case, Resonance Raman happens when the energy of incident light is close to the energy difference between two electronic states of the material under investigation. Compared to normal Raman process, Resonance Raman tends to give much higher intensities, thus may be beneficial for investigations of some materials, especially when the concentration of the material is relatively low [16-18]. For a comparison regarding the energy transitions in Stokes Raman, anti-Stokes Raman, Resonance Raman, as well as Rayleigh scattering, we can refer to Figure 1.1 [12], which shows the diagrammatic representations for all these four processes. Note that E_0 and E_1 represent the

ground and first excited electronic states, respectively. The Arabic numerals 0~3 label different vibrational states, while V and V' represent vibrational states for E_0 and E_1 , respectively. The “virtual” state is represented by dotted line.

When more atoms are added to a molecule, more bonds between the atoms are introduced, which leads to greater complexity in the vibrations of the molecule, or more generally, to the system of interest. Although the total vibration could be very complicated, it is known that any complex vibration could be taken as a superposition of several so called “normal vibration modes” which are independent of each other. Each of these normal modes corresponds to a certain type of simple vibration with a specific Raman shift. For instance, in CO_2 molecule, there are four normal modes: ν_1 , ν_{2a} , ν_{2b} , and ν_3 [12]. The Raman shift for these modes is 1340 cm^{-1} for the mode ν_1 , 667 cm^{-1} for the two modes ν_{2a} and ν_{2b} , and 2350 cm^{-1} for the mode ν_3 , respectively. Especially, the two modes ν_{2a} and ν_{2b} constitute a set of doubly degenerate vibrations, which only differs from each other by the direction of vibrations.

No further details will be presented regarding normal vibrational modes. However, we need to realize that Raman spectroscopy detects each of the normal vibrational modes that is allowed by the Raman selection rules.

(2) A classical treatment [12]

In classical physics, a vibration mode that is detected by Raman spectroscopy is interpreted as atoms inside the material going through a certain type of “forced” vibration, driven by the electric field of the incident light. Again the simple diatomic molecule is taken as the model, the vibration (q) of which is described by the following formula:

$$q = q_0 \cos(2\pi\nu_m t) \quad (1.9)$$

where ν_m is the vibrational frequency of the molecule. Suppose a monochromatic light (E) is incident on the material, with an amplitude of E_0 and frequency of ν_0 . By the light's radiation, a dipole moment (P) is induced in the material:

$$E = E_0 \cos(2\pi\nu_0 t) \quad (1.10)$$

$$P = \alpha E = \alpha E_0 \cos(2\pi\nu_0 t) \quad (1.11)$$

where α is called polarizability, which describes the proportionality between the induced dipole moment and the external electric field of light. This parameter is definitely related to the configuration of atoms in the molecule: in other words, the molecular vibration q . An approximation has been made: under small amplitudes of vibrations, α is linearly proportional to q . Thus, α could be expanded in Taylor series with respect to q in the following way:

$$\alpha = \alpha_0 + \left(\frac{\partial\alpha}{\partial q}\right)_0 q + \dots \quad (1.12)$$

where α_0 represents the polarizability when the molecule is at its equilibrium position; and $(\partial\alpha/\partial q)_0$ is the first derivative of α with respect to q , calculated at $q = 0$. Another approximation is made in the expression above: that is, the higher derivatives of α with respect to q is neglected. For example, the first neglected term should be $\frac{1}{2}(\partial^2\alpha/\partial q^2)_0 q^2$, and the next neglected term should be $\frac{1}{6}(\partial^3\alpha/\partial q^3)_0 q^3$, and so on. By plugging formula (1-12) into (1-11), we obtain the following expressions:

$$P = \alpha_0 E_0 \cos(2\pi\nu_0 t) + \left(\frac{\partial\alpha}{\partial q}\right)_0 q_0 E_0 \cos(2\pi\nu_0 t) \cos(2\pi\nu_m t) \quad (1.13)$$

$$P = \alpha_0 E_0 \cos(2\pi\nu_0 t) + \frac{1}{2} \left(\frac{\partial\alpha}{\partial q}\right)_0 q_0 E_0 \left\{ \begin{array}{l} \cos[2\pi(\nu_0 + \nu_m)t] \\ + \cos[2\pi(\nu_0 - \nu_m)t] \end{array} \right\} \quad (1.14)$$

From these formulae above, it can be deduced that the molecule could radiate light of three frequencies: (1) A radiation of ν_0 , the frequency of which is the same as the incident light, in corresponds to Rayleigh scattering, (2) A radiation of $\nu_0 - \nu_m$, the frequency of which is lower than the incident light, in corresponds to Stokes Raman scattering. (3) A radiation of $\nu_0 + \nu_m$, the frequency of which is higher than the incident light, in corresponds to anti-Stokes Raman scattering. In each of these three types of radiations, in general, only one phonon is involved during the light-matter interaction. In contrast, radiations involving more than one phonons is also possible, when we recall the terms that have been neglected in formula (1-12). These higher order derivatives are responsible for Raman scatterings of higher frequencies (in other words, larger Raman shifts), however, which also possess much lower possibilities to take place at room temperature.

On the other hand, from the viewpoint of quantum mechanics, the scattering process resulting from the vibration is considered to take place in correspondence to a transition from one state of the system to another. Thus, it involves a transition probability depending on both the initial and final states, and the dipole moment as well. This quantum mechanics discussion is out of the scope of this dissertation, and can be found in the literature such as [19,20] for further details.

(3) Raman tensor and Raman selection rules

As was mentioned above, different types of normal vibration modes are present inside the material under examination. However, we may not be able to detect all these modes in Raman spectroscopy under a specific scattering geometry. In other words, with the scattering geometry fixed, some vibration modes are allowed in Raman scattering process and thus detectable in Raman spectroscopy; on the other hand, some other modes

are forbidden and thus could not give detectable Raman signals. The former modes are said to be Raman active or Raman allowed, while the latter modes are Raman inactive or Raman forbidden. The rules that indicate whether a mode is Raman allowed or not is named as Raman selection rules. In order to work out the Raman selection rules, different methods, by using either quantum mechanics or classical physics, have been developed. In this dissertation, we have applied the results developed by Loudon based on Raman tensors [13].

In order to understand the Raman tensors, it is beneficial to firstly recall the polarizability α mentioned previously, which concerns the proportionality between the external light field E and the induced dipole P of the material. In general, the relationship between E and P is nonlinear, thus it is appropriate to rewrite formula (1-11) into the following matrix form, where the matrix is called the polarizability tensor:

$$\begin{bmatrix} P_x \\ P_y \\ P_z \end{bmatrix} = \begin{bmatrix} \alpha_{xx} & \alpha_{xy} & \alpha_{xz} \\ \alpha_{yx} & \alpha_{yy} & \alpha_{yz} \\ \alpha_{zx} & \alpha_{zy} & \alpha_{zz} \end{bmatrix} \begin{bmatrix} E_x \\ E_y \\ E_z \end{bmatrix} \quad (1.15)$$

It is apparent that each polarizability tensor corresponds to a certain type of vibration. According to quantum mechanics, a vibration mode is Raman allowed in cases where as long as one of the tensor elements changes during the vibration. For materials with simple structures, it is practical to decide this change by directly examining the vibrations of the material. However, when the material is getting more complex, for instance, the material is not a simple diatomic molecule but a semiconductor crystal or superlattice, it is not practical to conduct direct inspection on the material's vibrations anymore. Further approximations have been made to deal with the selection rules. One of the methods is by using Raman tensors [13], which also correspond to certain types of

vibrations. Unlike the polarizability tensors, for which people need to decide whether there is a change in the tensor elements, it is more straightforward to use Raman tensors to decide the Raman selection rules. For any mode, its Raman cross section (RC) is proportional to $|\mathbf{e}_i \cdot \mathbf{R} \cdot \mathbf{e}_s|^2$, where \mathbf{R} refers to the Raman tensor corresponding to this mode, while \mathbf{e}_i and \mathbf{e}_s are the polarization vectors of the incident excitation light and scattered Raman signals. By using this Raman tensor method, we can find out the Raman selection rules for InAs/GaSb and InAs/InAsSb T2SLs, as well as the related materials. These details are to be presented in section 1.3 and 1.4, respectively.

1.2 PL Technique: Fundamental Principles and Applications

PL refers to the radiative re-emission by material after light-material interaction [21]. As a usual case in this process, a photon of the incident light is absorbed by the material, which promotes an electron of the material into a higher level than the original one. Correspondingly, pairs of carriers consisting of electrons and holes are generated. This energy transition is usually followed by the energy relaxation of the system, which leads the electron drop down from the excited level to a lower one. Finally, the photo-generated carriers (electrons and holes) recombine with each other and photons are re-emitted by the material, with a frequency same as or lower than the incident light. PL is a general description of this photon re-emission process excited by light.

These days, PL spectroscopy is one of the major spectroscopic methods used for material research. Due to the intimate relationship between PL and photo-carrier generation and recombination, PL spectroscopy has been extensively used in investigations of recombination mechanisms of materials. For instance, PL has been used to study the recombination channels in carbon nanotubes which are DNA-wrapped [22], or to analyze

the recombination mechanism of Amine-Functionalized organic/inorganic hybrids [23]. On the other hand, PL spectroscopy is also a significant tool in defect-related studies, such as establishing a correlation between the PL lifetime and defect density in ZnO [24], monitoring the defect distribution in multi-crystalline silicon [25], etc. Especially, in our dissertation, micro-PL spectroscopy also is used as the major tool to analyze the behaviors of defects in CdTe epilayers. Aside from these applications, PL spectroscopy is also used in studies on band gaps [26,27], and explorations of surface effects [28-30].

1.3 Fundamentals of InAs/GaSb T2SLs

1.3.1 InAs/GaSb T2SL: A Model System

(1) InAs/GaSb heterostructure

InAs and GaSb, which are both significant compounds based on III-V group elements, share the same structure of zincblende and both belong to T_d group. Besides, they are also roughly latticed matched: at room temperature, InAs has a lattice constant of 6.06 Å [31], while GaSb has a lattice constant of 6.10 Å [32]. At room temperature, InAs has a band gap of 0.36eV, and GaSb has a band gap of 0.78eV. By stacking these two materials together to form a heterostructure, an unusual type of band lineup appears: the valence band maximum of GaSb is higher than the conduction band minimum of InAs, ending up with a broken gap lineup of about 0.15eV [32]. This “broken” lineup has been experimentally observed in 1977, by Sakaki et al [33]. On the other hand, it has also been predicted theoretically, by either using pseudopotential theory [34] or LCAO theory to calculate heterostructure band lineups [35].

After carefully inspecting the InAs/GaSb heterostructure, and comparing it with heterostructures that have been extensively studied in previous work [36-39], such as the

GaAs/AlAs heterostructure, we found out that the InAs/GaSb heterostructure has formed a new model system, from the aspect of lattice dynamics and electronic energy band. To make the comparison brief and clear, we choose the GaAs/AlAs heterostructure as a typical example for those heterostructures which have been previously better studied and share many important similarities, and list all the significant differences between the two types of heterostructures in below.

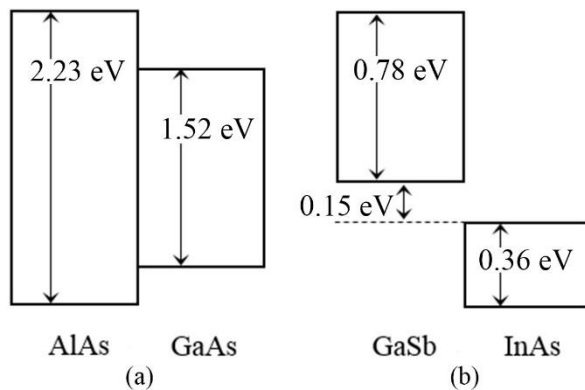


Figure 1.2: Schematic graph showing the alignments of the conduction and valence band edges at the interface for (a) AlAs/GaAs heterostructure (Type I straddling lineup), (b) InAs/GaSb heterostructure (Type II broken lineup) [32,40].

Firstly, the band alignment for the two heterostructures are different. In Figure 1.2, both the lineup for GaAs/AlAs and InAs/GaSb heterostructure is shown, thus providing a clear contrast between the two. In the GaAs/AlAs heterostructure [40], the band lineup is straddled: for GaAs, its valence band maximum and conduction band minimum both lie inside the bandgap of AlAs. This type of lineup has been named as type-I band alignment, which is shown in panel (a) of Figure 1.2. Evidently, this is very different from the situation for the InAs/GaSb heterostructure, which is shown in panel (b) of the figure: as mentioned

previously, a broken lineup appears at the interface, and this type of lineup has been named as type-II band alignment.

Secondly, in the GaAs/AlAs heterostructure, the element As is shared by both the two constituents. Therefore, layers of common atoms (in this case, As) are showing up at the interface of the heterostructure. On the other hand, in the InAs/GaSb heterostructure, no common element is shared by the two constituents. Thus, the interface is expected to be more localized as compared to the GaAs/AlAs case. Besides, two new bonds are possible: the Ga-As bond and the In-Sb bond, which do not exist in the two constituents. Therefore, two types of interfaces (IF) are expected in the InAs/GaSb heterostructure, either InSb IF or GaAs IF.

Thirdly, in the GaAs/AlAs heterostructure, the optical phonon spectra for the two constituents are not overlapping [41,42]: for longitudinal optical (LO) modes, the $\Gamma - X$ dispersion of GaAs is $284.7\text{--}240.4\text{cm}^{-1}$, while that of AlAs is $400\text{--}393\text{cm}^{-1}$; for transverse optical (TO) modes, the $\Gamma - X$ dispersion of GaAs is $267.1\text{--}251.7\text{cm}^{-1}$, while that of AlAs is $363\text{--}337\text{cm}^{-1}$. In contrast, the optical phonon spectra for InAs and GaSb is strongly overlapping [43,44]: For LO modes, the $\Gamma - X$ dispersion of InAs is $238.6\text{--}203\text{cm}^{-1}$, which encloses that of GaSb ($233.1\text{--}211.4\text{cm}^{-1}$); for TO modes, that of GaSb is $228.8\text{--}211.8\text{cm}^{-1}$, which encloses that of InAs ($217.3\text{--}216\text{cm}^{-1}$).

In summary, these differences make the InAs/GaSb heterostructure an interesting model system as compared to those better studied ones, for which the GaAs/AlAs heterostructure is a typical example. The electronic structure and vibration spectrum of InAs/GaSb heterostructures are much more complex and intriguing, but also much less

understood, which motivates great interests and enthusiasm to study the heterostructure, ever since it is proposed.

(2) 1.3.2 InAs/GaSb SL

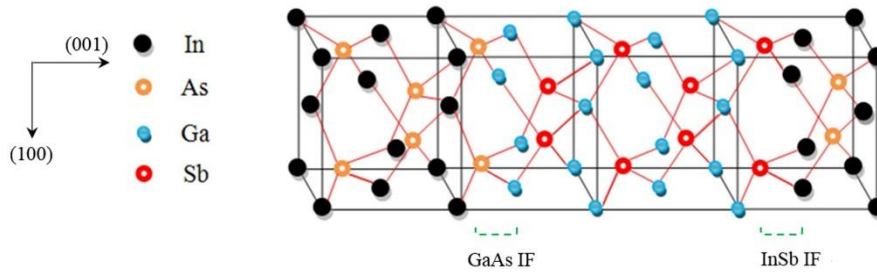


Figure 1.3: Schematic graph showing the lattice of InAs/GaSb T2SL grown along [001] direction. Both interfaces (IFs) are shown: InSb IF and GaAs IF, indicated by dotted bracket. This figure is a modified version of Figure.1 in [47], to show two types of interfaces.

When stacking the InAs and GaSb layers in a periodic way and making the thickness of each individual constituent layer go to several tens of nanometers, the InAs/GaSb T2SL is formed. Same as in the heterostructure case, two types of interfaces are possible in the SL, either InSb IF or GaAs IF [45]. Figure 1.3 shows a representative graph of InAs/GaSb T2SL grown along a [001] direction, with both types of IFs indicated. In SLs, this non-common-atom interface has another important consequence: the symmetry for the SLs is altered. For GaAs/AlAs SLs, the symmetry is D_{2d} ; whereas, the symmetry for InAs/GaSb SLs is C_{2v} [46].

As previously mentioned, the conduction band minimum of InAs lies lower than the valence band maximum of GaSb. This fact leads to a semi-metal behavior for the SL, when the thickness of each constituent layer is large enough such that the quantization effects could be reasonably neglected. However, when the layer thickness is decreased to

a certain degree, the quantization effect could not be neglected anymore. It will push the lowest electron state of the InAs layer up, and at the same time, push the highest hole state of the GaSb layer down. Finally, the highest hole state of the SL will lie lower than the lowest electron state of the SL, which makes the SL to behave as a semiconductor with a narrow bandgap. Ideally, this bandgap in the SLs could be tuned by properly engineering the thickness of each constituent layers; thus, a bandgap much smaller than that of InAs is possible.

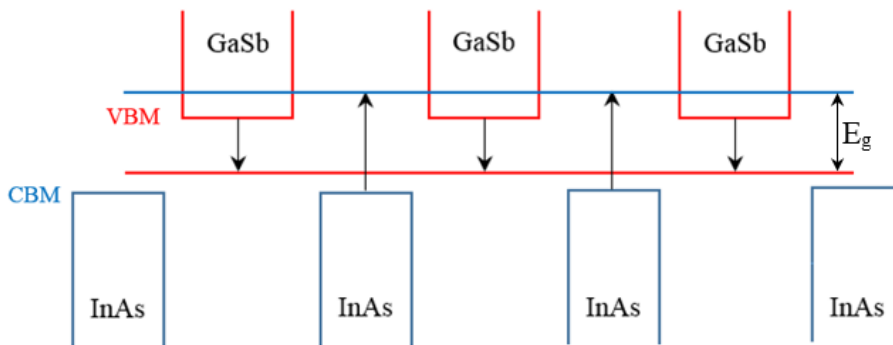


Figure 1.4: Representative graph showing the state conditions for both semi-metal and semiconductor behavior of the InAs/GaSb T2SL [32].

Figure 1.4 shows a representative graph, showing the state conditions for both semi-metal and semiconductor behavior of the InAs/GaSb T2SL. In this figure, CBM represents the conduction band minimum for InAs bulk, while VBM represents the valence band maximum for GaSb bulk. The arrows show the shifts in the highest hole state and the lowest electron state due to quantization effect, which results in a narrow bandgap E_g in the SL. For a quantitative theoretical treatment, a recent paper has applied a density functional theory to calculate the band structures of InAs/GaSb SLs [48].

1.3.2 InAs/GaSb T2SL or Heterostructure: Applications

(1) Applications in IR detections

Ever since the InAs/GaSb T2SL has been proposed, it has been regarded as one of the most promising materials for infrared (IR) applications [49]. Currently, the market-oriented IR detection generally relies on three types of materials [50]: (1) HgCdTe (MCT) alloys, (2) InSb bulks, and (3) GaAs/AlGaAs quantum wells (QWs). As a SL based on III-V compounds, one of the advantages for the InAs/GaSb-SL-based detectors over the MCT ones is that the production cost would be lower, due to the relatively mature technique in growth and fabrication. In addition, the SL-based detectors also have potential advantages over the MCT ones in aspects such as bandgap control and suppression of Auger recombination [51]. On the other hand, when compared to the InAs/GaSb T2SL, the other two IR materials based on III-V compounds also have their own shortcomings. InSb bulk is not able to cover the long wave infrared range (8~15 μm), while GaAs/AlGaAs QWs are not sensitive to surface-normal IR incidence. In contrast, the bandgap of the InAs/GaSb T2SL is tunable in a relatively wide range, which could cover both middle and long wave IR range (3~15 μm) [52,53]. In addition, it has been shown that promising improvements in dark current suppression could be obtained by engineering the SL structure, with the quantum efficiency only slightly influenced [54].

(2) Application in field of fundamental research

In addition to those IR application potentials, the InAs/GaSb heterostructures are also being explored for many fundamental research interests. For instance, the InAs/GaSb system has been considered to be a new system to study exciton condensation, and the condensed density allows further probe of Bose-Einstein to BCS crossover [55]. Besides,

the InAs/GaSb heterostructure is investigated to study quantum spin Hall effect [56], topologic insulator [57-61], or graphene-like Dirac fermion [62].

1.3.3 Raman Selection Rules for InAs/GaSb T2SL

Before we delve into the experimental details in exploration for these phonon modes, it is beneficial to analyze the Raman selection rules, which indicate whether a certain mode is allowed or forbidden, under a specific scattering geometry. Of course, once a phonon mode is determined to be Raman active, the magnitude of the RC is an important consideration, since it indicates whether or not the signal is actually detectable under the measurement conditions. By using the Raman tensor method developed by Loudon [13], we can determine whether a phonon mode is Raman allowed, as well as estimate its relative intensity by calculating its RC. According to Loudon's result, the RC for every phonon mode is generally dependent on three factors: (1) the scattering geometry that is applied in experiments, (2) the symmetry of the phonon mode under examination, and (3) the symmetry of the material under examination. Specific to this section, there are two types of materials to be examined: (1) InAs/GaSb T2SL samples with C_{2v} symmetry, and (2) InAs and GaSb bulks, both with T_d symmetry. Below, we will firstly introduce the Raman tensors for both the two symmetries, then provide the results regarding RCs of phonon modes, and finally make detailed discussions.

For C_{2v} symmetry, there are four allowed Raman modes with these Raman tensors: $A_1(z') = [(a,0,0), (0,b,0), (0,0,c)]$, $B_1(x') = [(0,0,e), (0,0,0), (e,0,0)]$, $B_2(y') = [(0,0,0), (0,0,f), (0,f,0)]$, and $A_2 = [(0,d,0), (d,0,0), (0,0,0)]$. Here x' , y' , and z' refer to the principal axes of C_{2v} with $x' \sim [110]$, $y' \sim [\bar{1}10]$, and $z' \sim [001]$, with respect to those cubic axes $x \sim [100]$, $y \sim [010]$, and $z \sim [001]$. For T_d symmetry, on the other hand, there are three allowed Raman modes

with these Raman tensors: $F_2(x) = [(0,0,0), (0,0,d), (0,d,0)]$, $F_2(y) = [(0,0,d), (0,0,0), (d,0,0)]$, and $F_2(z) = [(0,d,0), (d,0,0), (0,0,0)]$. Again, the notations x , y , and z refer to $x \sim [100]$, $y \sim [010]$, and $z \sim [001]$, respectively, which are the principal axes of T_d . The geometric relations of these lattice axes are illustrated in Figure 1.5.

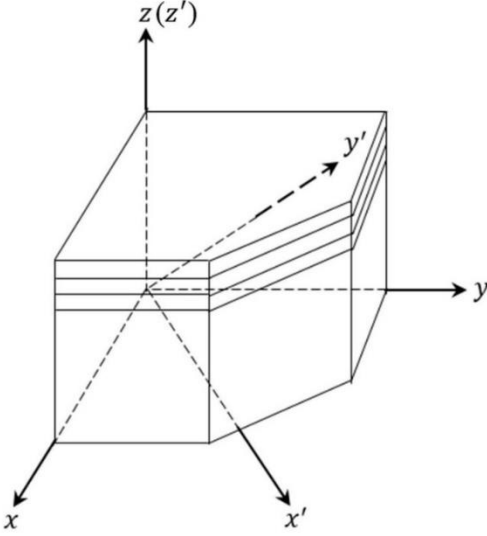


Figure 1.5: Representative graph showing the geometric relations of the lattice planes. x , y , z refers to the cubic axes $x \sim [100]$, $y \sim [010]$, and $z \sim [001]$, respectively. x' , y' , and z' refers to the principal axes of C_{2v} with $x' \sim [110]$, $y' \sim [\bar{1}10]$, and $z' \sim [001]$.

Especially, for InAs/GaSb T2SL, if one envisions that the difference between either the cations or the anions vanishes, then the C_{2v} symmetry should be altered and D_{2d} symmetry be recovered. Indeed, by letting $a = b$, $c = 0$, and $e = f$, the modes A_1 and (B_1, B_2) will become $B_2(z)$ and $E(x,y)$ belonging to D_{2d} symmetry, respectively. A_2 does not have a correspondence in D_{2d} . Thus, c and d are entirely due to the symmetry reduction from D_{2d} to C_{2v} , and their effects are expected to be small. Note that the symmetry axes of C_{2v} are different from those of D_{2d} and T_d ; on the other hand, the symmetry axes of the

latter two are the same. The discussion on D_{2d} , which is used to approximate the symmetry of InAs/InAsSb T2SL, will be presented in section 1.4.

It has been mentioned that the RC is proportional to $|\mathbf{e}_i \cdot \mathbf{R} \cdot \mathbf{e}_s|^2$, where \mathbf{R} is the Raman tensor, while \mathbf{e}_i and \mathbf{e}_s are the polarization vectors of the incident and scattered light. As will be presented in chapter two, \mathbf{e}_i and \mathbf{e}_s are determined by the polarizer and analyzer that were actually used in experiments. Thus, each set of \mathbf{e}_i and \mathbf{e}_s determines a polarization configuration. With the configuration being varied, the RC may also be altered.

Table 1.1 and Table 1.2 (to be shown on next page) summarize the calculated RC of each mode under every possible polarization configuration, for C_{2v} and T_d symmetry, respectively. These calculated RCs generally indicate the Raman selection rules for the modes, and the detailed discussions are to be presented after these tables. At this step, we need to notice that, for instance, the two entries a_{LO}^2 and a_{TO}^2 are different. In general, the tensor element, such as a or b , only concerns about the direction of the atomic displacement of phonons, while the subscript “LO” or “TO” is used to show the atomic displacement direction relative to the propagation direction of the phonon mode. Especially, in back-scattering geometry, the phonon propagation direction is anti-parallel to the propagation direction of incident excitation laser. In one word, a_{LO} and a_{TO} are different quantities, which possibly have different magnitudes. In addition, it is found out that, for C_{2v} and T_d , as well as D_{2d} to be discussed in section 1.4, within the same scattering geometry, the two cross-polarization configurations have identical results: for instance, $z'(x', y')\bar{z}'$ has the same result as $z'(y', x')\bar{z}'$ does; while $x'(y', z')\bar{x}'$ has the same result as $x'(z', y')\bar{x}'$ does. Hence, for the sake of brevity, only one cross-polarization is included in the tables.

Table 1.1: Polarization selection rules for C_{2v} Raman modes in back-scattering geometries. The photon wave vectors are along $z' \sim [001]$, $x' \sim [110]$, and $y' \sim [\bar{1}10]$, respectively. The results for two cross polarization configurations are identical, so only one is shown.

Symmetry Geometry	$A_1(z')$	$B_1(x')$	$B_2(y')$
$z'(x', x')\bar{z}'$	a^2_{LO}	0	0
$z'(y', y')\bar{z}'$	b^2_{LO}	0	0
$z'(x', y')\bar{z}'$	0	0	0
$x'(y', y')\bar{x}'$ $y'(x', x')\bar{y}'$	b^2_{TO} a^2_{TO}	0	0
$x'(z', z')\bar{x}'$ $y'(z', z')\bar{y}'$	c^2_{TO}	0	0
$x'(y', z')\bar{x}'$ $y'(x', z')\bar{y}'$	0	0 e^2_{TO}	f^2_{TO} 0

Table 1.2: Polarization selection rules for T_d Raman modes in back-scattering geometries. The photon wave vectors are along $z' \sim [001]$, $x' \sim [110]$, and $y' \sim [\bar{1}10]$, respectively. The results for two cross polarization configurations are identical, so only one is shown.

Symmetry Geometry	$F_2(x)$	$F_2(y)$	$F_2(z)$
$z'(x', x')\bar{z}'$	0	0	d^2_{LO}
$z'(y', y')\bar{z}'$	0	0	d^2_{LO}
$z'(x', y')\bar{z}'$	0	0	0
$x'(y', y')\bar{x}'$ $y'(x', x')\bar{y}'$	0	0	d_{TO}^2
$x'(y', y')\bar{x}'$ $y'(x', x')\bar{y}'$	0	0	d_{TO}^2
$x'(z', z')\bar{x}'$ $y'(z', z')\bar{y}'$	0	0	0
$x'(y', z')\bar{x}'$ $y'(x', z')\bar{y}'$	$d_{TO}^2/2$	$d_{TO}^2/2$	0

(1) Selection rules for C_{2v} symmetry, under (001) back-scattering geometry

For InAs/GaSb T2SLs with C_{2v} symmetry, only LO modes are allowed in the two parallel-polarization configurations: $z'(x', x')\bar{z}'$ and $z'(y', y')\bar{z}'$. In addition, they should have the symmetry of $A_1(z')$. However, the RCs under the two configurations are different, one goes to a_{LO}^2 while the other goes to b_{LO}^2 . Thus, one may expect to observe anisotropy between these two polarization configurations. On the other hand, the LO modes are forbidden in the remaining two cross-polarization configurations, $z'(x', y')\bar{z}'$ and $z'(y', x')\bar{z}'$. TO modes, no matter what symmetry they have, are forbidden under all the four polarization configurations.

(2) Selection rule for T_d symmetry, under (001) back-scattering geometry

For InAs and GaSb bulks, which both belong to T_d group, LO modes are only allowed in the two parallel polarization configurations: $z'(x', x')\bar{z}'$ and $z'(y', y')\bar{z}'$. They should be $F_2(z)$ modes, and share the same RCs ($\sim d_{LO}^2$). Thus, there is no anisotropy to be expected from these two directions x' and y' , under this scattering geometry. Same as in the C_{2v} case, the LO modes are also forbidden in the two cross-polarization configurations, and TO modes are forbidden under all the four polarization configurations.

(3) Selection rules for C_{2v} symmetry, under (110) and $(\bar{1}\bar{1}0)$ back-scattering geometry

These two lattice planes (110) and $(\bar{1}\bar{1}0)$, correspond to the two natural cleaved edges of a zincblende structure. Firstly, it should be noticed that under these two scattering geometries, there are eight possible polarization configurations. To make the further comparison clear, we divide them into groups, with a standard that the polarization configurations within a group should hold some similarities, or one polarization configuration could be considered as a counterpart of the other. Hence, three groups are decided: (1) Group I: $x'(y', y')\bar{x}'$ and $y'(x', x')\bar{y}'$, it is clear that the latter configuration is

the counterpart of the former one, when the laser incidence direction is altered from x' to y' ; (2) Group II: $x'(z', z')\bar{x}'$ and $y'(z', z')\bar{y}'$, these two are also counterparts for each other; and (3) Group III: $x'(y', z')\bar{x}'$, $x'(z', y')\bar{x}'$, $y'(x', z')\bar{y}'$ and $y'(z', x')\bar{y}'$. The above method of division will be applied in both C_{2v} and T_d case, as well as D_{2d} case that to be discussed in the following section.

Under either (110) or ($\bar{1}10$) scattering geometry, LO modes are forbidden under all the polarization configurations, no matter what symmetry the mode may have. On the other hand, TO modes with certain symmetries are allowed, under specific polarization configurations. Discussions will be organized based on the three groups mentioned above.

In $x'(y', y')\bar{x}'$, only $A_1(z')$ mode is allowed, with a RC $\sim b^2_{TO}$. In $y'(x', x')\bar{y}'$, similar result holds: only $A_1(z')$ mode is allowed, with a RC $\sim a^2_{TO}$. An anisotropy between the two planes (110) and ($\bar{1}10$) is expected.

In $x'(z', z')\bar{x}'$ and $y'(z', z')\bar{y}'$, only TO mode with $A_1(z')$ symmetry is allowed, with a RC $\sim c^2_{TO}$. As was mentioned, the Raman tensor element c is resulted from the symmetry reduction from D_{2d} to C_{2v} , and its magnitude should be quite small, because it is forbidden in D_{2d} . Thus, very weak Raman signals are expected from these two polarization configurations.

In the remaining four polarization configurations, TO modes with either $B_1(x')$ or $B_2(y')$ symmetries are allowed. A difference could be expected from the (110) and ($\bar{1}10$) planes, as the RC is proportional to either f^2_{TO} or e^2_{TO} in these two cases. However, the difference between e and f also results from the symmetry alteration from D_{2d} to C_{2v} . Hence, this anisotropy between the (110) and ($\bar{1}10$) plane may also be very small.

(4) Selection rules for T_d symmetry, under (110) and ($\bar{1}10$) back-scattering geometry

Similar as in C_{2v} case, under these two scattering geometries, LO modes are forbidden under all the polarization configurations. On the other hand, TO modes with certain symmetries are allowed: (1) In $x'(y', y')\bar{x}'$ and $y'(x', x')\bar{y}'$, only $F_2(z)$ mode is allowed, with the same RC $\sim d_{TO}^2$. Thus, no anisotropy between the two planes (110) and $(\bar{1}\bar{1}0)$ is expected. (2) In $x'(z', z')\bar{x}'$ and $y'(z', z')\bar{y}'$, all TO modes are forbidden, no matter the mode symmetry. (3) In the remaining four polarization configurations, TO modes with both $F_2(x)$ and $F_2(y)$ are allowed, with an equal contribution of $\sim d_{TO}^2/2$. Disregard the difference in mode symmetry, it should be noticed that the RC in these polarization configurations will be the same as in $x'(y', y')\bar{x}'$ and $y'(x', x')\bar{y}'$, since the total RC also goes to d_{TO}^2 .

1.3.4 Theoretical Predictions on Phonon Spectra of InAs/GaSb T2SLs

As was previously mentioned, the InAs/GaSb T2SL is a model system, the physics behind which is still under investigation. Since 1986, significant theoretical efforts have been made to explore the complexity in the phonon spectrum of the T2SL, and four types of phonon modes have been theoretically predicated [46,47,63,64]. (1) Confined (C) modes: these modes could propagate in one of the constituents, in a similar way as the corresponding bulk modes in that constituent. On the other hand, the lattice displacements of these modes are negligible in the other constituent. Naturally, these C modes are either InAs-like, or GaSb-like modes, with frequencies nearly the same as the corresponding bulk modes at high symmetry points. (2) Quasi-confined (QC) modes: these modes have lattice displacements which are mostly limited to one constituent, but the mode frequencies tend to be different from the bulk modes of high symmetry points. (3) Extended (EX) modes: these modes have lattice displacements with considerable magnitudes throughout the

whole SL period, i.e., involving the vibrations of almost all the atoms in the SL. (4) Interface (IF) modes: these modes only have non-negligible lattice displacements of limited number of atoms near the interfaces of the two constituents. Thus, they are considered to be localized at the interface. Due to the no-common-element interface in the SL, there are two kinds of IF modes: GaAs-like (IF1) and InSb-like (IF2), with their frequencies locating above and below the general SL modes, respectively [46,47].

1.3.5 A Brief Review on Previous Raman Studies on InAs/GaSb T2SLs

Raman spectroscopy is a very effective tool for structural characterization and probing electron-phonon coupling in semiconductor SLs [65]. For instance, the observation of confined optical phonons in GaAs/AlAs SLs not only is an important indication of the material's structural quality (e.g., the abruptness of the interface), but also provides valuable information for the vibration spectrum of the related bulk materials [65].

As for InAs/GaSb T2SL, numerous Raman studies have been reported over the past 23 years [38,45,66-71]. Among these investigations, most of the studies were performed in the (001) back-scattering geometry. Under this scattering geometry, LO modes are theoretically allowed, while TO modes are forbidden. Usually only one major Raman peak was observed at around $236\text{--}238\text{cm}^{-1}$, which has been assigned generally as a SL-LO mode. It was believed that due to the overlapping of the bulk phonon modes, it was difficult to experimentally resolve the confined and extended modes [38,67,68]. Two weak peaks close to the InAs TO mode $\sim 218\text{ cm}^{-1}$ and/or the GaSb TO mode $\sim 228\text{ cm}^{-1}$ have/have been observed [38,71]. The appearance of these forbidden modes are attributed to the possible disorder inside the SLs. Besides, two weak LO-IF modes have also been reported, which was often used to assess the interface composition [45]. To provide a general overview on

the previous Raman results, Figure 1.6 shows one typical spectrum reported in the literature [38], in which the approximate positions of the above mentioned four types of phonon modes have been marked by the authors.

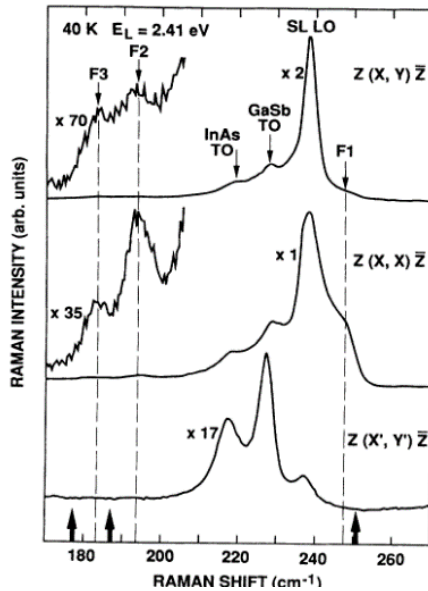


Figure 1.6: Typical back-scattering Raman spectrum of InAs/GaSb T2SL from (001) plane, as reported in the literature [38]. Four types of phonon modes have been observed: the SL LO mode, the InAs TO, the GaSb TO, the GaAs IF mode (indicated as F1 and F2), and InSb IF mode (indicated as F3).

According to the Raman selection rules mentioned in section 1.3.3, the RC varies when the scattering geometry is altered. Correspondingly, modes will be allowed under certain scattering geometries, while may be forbidden under others. Thus, performing Raman measurements on surfaces other than the (001) plane should, in principle, yield complementary information to that from the (001) plane. Such attempt has been made to perform the cleaved edge Raman study on the SL [69]. However, due to the inadequate spatial resolution of the equipment used, it was not possible to resolve the SL signals from the substrate buffer layers.

To summarize these experimental results on probing the phonon modes in the InAs/GaSb T2SL, except for the IF modes, it has not been possible to correlate the experimental results with the three types of modes that have been predicted: C modes, QC modes, and EX modes. In other words, previous efforts for the T2SL have not been able to make any unambiguous connections between the experimental observations and the theoretical predictions.

1.4. Fundamentals of InAs/InAsSb T2SL

1.4.1 InAs/InAsSb T2SL: A Model System

Like InAs/GaSb T2SLs, T2SLs based on InAs and InAsSb are also considered as promising substitutes for the widely used MCT system [72]. Currently, these InAs/InAsSb T2SLs are receiving growing interests, as devices based on these Ga-Free SLs have demonstrated advantages such as reduced dark current and increased minority carrier lifetimes [73]. These advantages have been hypothesized to be related to the fact that the density of native defects associated with GaSb is considerably reduced in these Ga-Free SLs [74].

Similar to the InAs/GaSb T2SL, the InAs/InAsSb T2SL is also a model system from the aspect of lattice vibrations. When compared to the GaAs/AlGaAs SLs and InAs/GaSb SLs, the SLs based on InAs and InAsSb have several interesting features: (1) The interfaces of the SL have type II band alignment, the same as InAs/GaSb T2SL, but different from GaAs/AlGaAs SLs. (2) Common atoms are shared by the two constituents (in this case, In), which is similar to the GaAs/AlGaAs SL, but different from the InAs/GaSb T2SL. (3) The optical phonon spectra for the two constituents will inevitably overlap, since one constituent is an alloy of the other constituent with Sb. In a word, the

InAs/InAsSb T2SL is another model system, the features of which could not be represented by either the GaAs/AlGaAs system or the InAs/GaSb system. Consequently, new features are expected, regarding the lattice vibration properties of the InAs/InAsSb T2SL.

When referring to literature, to our best knowledge, there is no systematic Raman studies regarding the phonon modes of the InAs/InAsSb T2SL by now, although InAsSb alloy has been studied [75,76]. Thus, little is known regarding the SL's lattice vibration properties, which motivates us greatly to conduct some pioneering systematic Raman studies on the SLs. In this dissertation, we want to use micro-Raman, in a similar way as for the case of the InAs/GaSb T2SL, to study the vibrational properties of the InAs/InAsSb T2SLs, and intend to compare the findings with those of the InAs/GaSb system.

1.4.2 Raman Selection Rules for InAs/InAsSb T2SLs

In this section, we derive the Raman selection rules for the InAs/InAsSb T2SL. Generally, D_{2d} symmetry could generally represent the symmetry of the SLs. However, we need to note that some deviations of the SL's actual symmetry from the ideal D_{2d} symmetry is also expected.

For D_{2d} symmetry, there are three allowed Raman modes with these Raman tensors: $B_2(z) = [(0,d,0), (d,0,0), (0,0,0)]$, $E(y) = [(0,0,e), (0,0,0), (e,0,0)]$, and $E(x) = [(0,0,0), (0,0,e), (0,e,0)]$. The notations x , y , and z refer to $x \sim [100]$, $y \sim [010]$, and $z \sim [001]$, respectively. Similar as in the previous section, we determine the RC for phonon modes of D_{2d} by using the Raman tensor method, and summarize the results in Table 1.3 (to be shown in next page).

Table 1.3: Polarization selection rules for D_{2d} Raman modes in back-scattering geometries. The photon wave vectors are along $z' \sim [001]$, $x' \sim [110]$, and $y' \sim [\bar{1}10]$, respectively. The results for two cross polarization configurations are identical, so only one is shown.

Symmetry Geometry	E(x)	E(y)	$B_2(z)$
$z'(x', x')\bar{z}'$	0	0	d_{LO}^2
$z'(y', y')\bar{z}'$	0	0	d_{LO}^2
$z'(x', y')\bar{z}'$	0	0	0
$x'(y', y')\bar{x}'$ $y'(x', x')\bar{y}'$	0	0	d_{TO}^2
$x'(z', z')\bar{x}'$ $y'(z', z')\bar{y}'$	0	0	0
$x'(y', z')\bar{x}'$ $y'(x', z')\bar{y}'$	$e_{TO}^2/2$	$e_{TO}^2/2$	0

(1) Selection rule for D_{2d} symmetry, under (001) back-scattering geometry

Under this scattering geometry, LO modes are only allowed in the two parallel polarization configurations: $z'(x', x')\bar{z}'$ and $z'(y', y')\bar{z}'$. They should be $B_2(z)$ modes, and share the same RCs ($\sim d_{LO}^2$). Thus, no anisotropy is expected between x' and y' . Same as in the cases of C_{2v} and T_d , the LO modes for D_{2d} are also forbidden in the two cross polarization configurations, while the TO modes are forbidden under all the four polarization configurations.

(2) Selection rule for D_{2d} symmetry under (110) and ($\bar{1}10$) back-scattering geometry scattering

Under these two scattering geometries, LO modes are forbidden under all the polarization configurations. On the other hand, TO modes with certain symmetries are allowed: (1) In $x'(y', y')\bar{x}'$ and $y'(x', x')\bar{y}'$, only $B_2(z)$ mode is allowed, with the same RC $\sim d_{TO}^2$. Thus, no anisotropy is expected between the two cleaved edges (110) and ($\bar{1}10$).

(2) In $x'(z', z')\bar{x}'$ and $y'(z', z')\bar{y}'$, all TO modes are forbidden, no matter what the mode symmetry is. (3) In the remaining four polarization configurations, TO modes with both $E_2(x)$ and $E_2(y)$ are allowed, with an equal contribution of $\sim e^2_{\text{TO}}/2$. Disregard the difference in mode symmetry, it should be noted that the total RCs in these polarization configurations will be $\sim e^2_{\text{TO}}$.

Now we can make a brief comment on the selection rules for the three symmetries C_{2v} , T_d and D_{2d} . By comparing the entries in Table 1.1-1.3, a general similarity is clearly observed. The differences, on the other hand, is also readily to be attributed to the symmetry reduction from one symmetry to the other. For instance, for T_d symmetry, if a TO mode is allowed, its RC will always be proportional to $\sim d^2_{\text{TO}}$, no matter in what polarization configuration. On the other hand, in D_{2d} symmetry, the RC is different when the polarization configuration alters from the cross-polarization configurations to the allowed parallel ones, with proportionalities of e^2_{TO} and d^2_{TO} , respectively. This difference, which is a new feature shown in D_{2d} symmetry as compared to T_d , is apparently related to the symmetry reduction from the latter to the former.

1.4.3 Previous Raman Study on InAsSb Alloys

As was mentioned in section 1.4.1, there is a lack of existing Raman results regarding InAs/InAsSb T2SLs. On the other hand, there are several Raman studies investigating InAsSb alloys [75,76]. Since the alloy is one of the SL constituents, it is beneficial to summarize the Raman results on the alloy. Below, we will firstly overview the Raman study on the III-V alloys, and then present the Raman results on InAsSb alloy.

Generally, for any ternary alloy based on III-V elements, we can represent it by a common notation $AB_{1-x}C_x$, where A, B and C represent the three elements involved, and x

indicate the alloy composition. It can be summarized from the literature [76-79], that the Raman behaviors of these alloys generally fall into three scenarios: (1) One-mode behavior [77]: through the whole composition range ($0 \leq x \leq 1$), only one major mode is observed. The mode frequency will be that of AB when x is 0, and shift to the frequency of AC when x goes to 1. During the transition of x from 0 to 1, the mode frequency will make a continuous transition from that of AB to that of AC. (2) Two-mode behavior [78,79]: through the whole x range, two major mode is observed. These two modes are to be related to AB and AC, and the mode frequencies will go through a continuous transition with respect to x , in a similar way as in (1). (3) one plus two-mode behavior [76]: the alloy demonstrates one-mode behavior at certain ranges of x , while displays two-mode behavior at different ranges of x . However, no matter which specific Raman behavior the alloy will follow, it could be concluded that the observed mode will always be closely related to the constituents, and continuously shift due to the composition change in x .

Specific to the InAsSb alloy, there are several Raman studies conducted in previous work, in which the measurements were conducted from the growth plane, with back-scattering geometry applied [75,76]. As a typical example, we briefly summarize the results from Li's report, with Figure 1.7 (to be shown on next page) showing the typical spectrum reported in their study [75].

By examining Figure 1.7, it is found that two mode behavior is observed with the Sb composition x changes from 0 to 1: that is, except for two special cases of $x=0$ and $x=1$, one InAs like LO mode and one InSb like LO mode are observed simultaneously. The mode frequencies of these two modes could be fitted by the equations: $\nu_{L1} = 238 - 32x$, and $\nu_{L2} = 177 + 12x$, respectively; where the subscript $L1$ refers to the InAs like LO

mode and $L2$ refers to the InSb like LO mode. In addition, an InAs like TO mode is also resolved, but with much lower intensity. The mode frequency of this TO mode could be fitted by the equations: $\nu_{T1} = 219 - 27x$, when x follows into the range $0 \leq x \leq 0.23$. These observations are consistent with the Raman selection rules, since under the scattering geometry applied, LO modes are allowed while TO modes are forbidden. Also, a shoulder was observed, with a frequency lie between that of InAs LO and TO mode. This mode has been assigned to be disorder-activated optical phonon (DAO) modes [80,81].

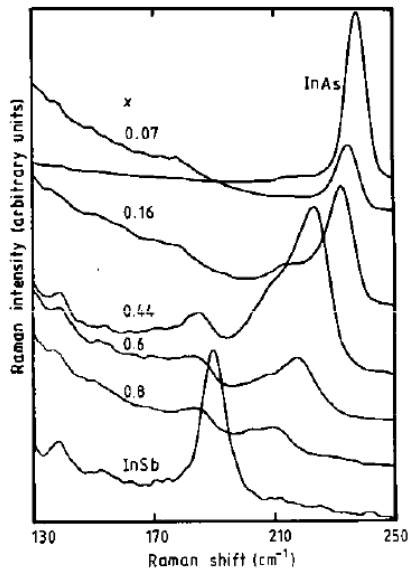


Figure 1.7: Typical back-scattering Raman spectrum of $\text{InAs}_{1-x}\text{Sb}_x$ alloys from (001) plane, as reported in [75].

Especially, it should be noted that by naming the major mode in the alloy as “InAs like LO”, for instance, the close relationship between the mode resolved in the alloy and the mode of binary compound is clearly indicated. However, due to the fact that in our work the Sb composition remains relatively small, only one mode is observed: that is, the

InAs-like LO mode. For the sake of brevity, we will refer to this mode as InAsSb alloy LO mode or simply alloy LO mode in this dissertation.

1.5 Fundamentals of CdTe Epilayers

1.5.1 General Information and Applications

CdTe is a significant compound based on II-VI group elements, with a zincblende structure. It is a direct bandgap material, with an $E_g \sim 1.5$ eV at room temperature. Currently, it is being used in various types of semiconductor applications.

Firstly, as a direct bandgap semiconductor, one of its major application is fabricating thin film photovoltaic (PV) devices [82-84]. Due to its high absorption coefficient, a CdTe thin film with a thickness of $\sim 2\mu\text{m}$ is generally enough to serve as the absorber layer of the solar cell [84]. Great efforts have been made to improve the efficiency of CdTe-based polycrystalline thin-film PV devices [85-87]. The highest reported efficiency of the CdTe based PV cell is 21.0% in 2014, which is very impressive, given the polycrystalline nature of the material being used [88]. To assess the full potential of the CdTe based PV technology, single crystalline CdTe PV research has received considerable attention in recent years [89,90].

Secondly, CdTe is playing important roles in IR optical detection applications covering several wavelength ranges. In IR detection, CdTe, together with HgTe, are the two constituents to make HgCdTe (MCT), which is a ternary alloy with a tunable direct bandgap and currently used as one of the major Mid-IR and long-IR detection materials. Besides, due to the relatively small lattice mismatch between HgCdTe and CdTe, CdTe is also frequently used as the substrate or buffer layer for HgCdTe [91]. It should be noticed that, although Si or GaAs is preferred to serve as the substrates for HgCdTe to cut

production cost, a CdTe buffer layer is still necessary to be grown between the HgCdTe layer and substrate [92-94]. Also, CdTe could be directly used to construct heterostructures with HgTe for IR detection, which have shown potential advantages over the MCT system [95].

Thirdly, CdTe is also an active semiconductor being used in many other applications. For instance, it is one of the most active compounds used in X-ray or gamma ray detectors [96-98]. The solid state detectors based on CdTe and CdZnTe are considered to have several superior qualities, which are able to provide excellent performance at room temperature [99]. Very recently, CdTe/PbTe single heterostructures are shown to form a two-dimensional electron gas (2DEG) at the heterostructure interface. More interestingly, this 2DEG exhibits quantum oscillations and is a new potential topologic insulator [100].

1.5.2 Study of Extended Defects in CdTe Epilayers

Extended defects are almost inevitable in semiconductors, and can influence the material's performance in more than one aspects. For instance, as one of the common types of extended defects in semiconductors, dislocations will drastically deplete the photo-generated carriers in its neighboring area through non-radiative recombination [101]. This will obviously bring adverse impacts on device performance when the material is the absorber layer, in either a PV or photo-detection device. In addition, dislocations may also influence other characteristics of the material, such as the polarization instability [102], junction leakage current [103], and so on.

Specific to CdTe, the study on its extended defects is indispensable when an in-depth understanding of the material is required. As mentioned in the previous section, growing attention is paid to the single crystalline CdTe PV devices, which naturally place

great necessity on the study of the crystalline defects. The situation is similar in cases where CdTe is used to construct layers to directly absorb light, with a general wavelength range from Gamma-ray to IR. Even in the case of MCT system, where CdTe is only serving as the buffer layer, these extended defects in CdTe layers will undoubtedly affect the epitaxial growth of HgCdTe, and eventually influence the IR detector's performance [104]. Additionally, in these devices, the current passes through the device usually needs to pass the buffer layer as well. Thus, defects in the buffer layer can also affect the device performance in this way. Therefore, it is concluded that the studies and analyses on the extended defects in CdTe epilayers, especially those regarding the defect behaviors in the luminescence process, are vital in understanding and evaluating the material qualities. In this dissertation, we are motivated to study the extended defects in single crystalline CdTe epilayers with varying defect density levels. The study is focused on the defects' behaviors in PL process, as well as their influences on the generation and recombination of photo-generated carriers.

There are various techniques that have been used to study the extended defects in CdTe. For instance, high resolution transmission electron microscopy (TEM), which possesses superior spatial resolution due to the small electron de-Broglie wavelength, has been used to examine the atomic structure of the defects [105]. PL spectroscopy, on the other hand, is another frequently used technique, which has long been used to study the defects in CdTe [106-110]. Other techniques, such as scanning electron microscopy (SEM), XRD, and so on, are also aiding in the study of defects in CdTe.

When reviewing the previous PL studies on defects in CdTe, it can be found that people usually focus their attention on macroscopically averaged PL spectra (acquired with

a large optical beam excitation) and intend to make discussions or comments when changes happen in PL spectra. One of the examples is that low temperature PL spectroscopy is used to investigate the compensation and passivation process in chlorine-doped CdTe epilayers [109]. On the other hand, there are some reports on spatially resolved PL study of CdTe [111], but direct spatial correlation between the defects and PL intensity variations was not established. Chemical etching has been a widely used technique to reveal dislocation-type defects in CdTe and other semiconductor materials [104,112-114]. However, it is unclear how such revealed defects manifest in the spatially resolved PL measurements, which offers a more direct probe for the carrier recombination at the defect site.

In our study, we for the first time try to establish the correlation between the etch pits (which are revealed by chemical etching and normally taken as markers for dislocations) and spatial distribution of the PL intensity. In the PL maps, we are able to observe how the PL intensity is distributed in a 2D area: some sites are showing relatively higher PL intensities, while some others showing lower intensities. Low PL intensity (resulting in a dark spot in the PL maps) usually indicates higher possibility of non-radiative recombination, thus the analysis on these PL dark spots will provide information directly related to material quality and device performance. It should be noted that although these PL dark spots could be possibly presumed to be the extended defects or in the vicinity area, there is no 100% certainty. On the other hand, although the etch pits revealed by chemical etching are reasonably considered to be the extended defects in the epilayers, there is no direct evidence showing that these etch pits would certainly influence device performance in a negative way. By correlate the PL dark spots with the etch pits revealed in the same area, we are able to (1) figure out the PL behaviors of these etch pits, and

further find out their effects on the photo-generated carriers' non-radiative recombination process; (2) explore other possible features that may not be revealed by chemical etching, but still have considerable influences on the non-radiative recombination process. This study will be especially useful when the defect density levels are relatively high, which makes the study on single defect impractical.

Especially, in our work, by using the confocal micro-PL (μ -PL) technique equipped in our Raman system, the above PL mapping analysis is enabled with a sub-micron range spatial accuracy. This sub-micron spatial resolution would not be possible if conventional macro-PL technique is used, since in macro-PL case, large area uniform illumination method is usually used. Consequently, it could only provide averaged PL intensity and fail to provide a site-to-site analysis. Confocal μ -PL technique, on the other hand, ensures that the collected PL signals originate from a well-defined volume at the excitation site [115]. Thus, it offers superior spatial resolution than the macro-PL technique [116]. Especially, in our work, the spatial resolution could be $\sim 0.36\mu\text{m}$ (by using 532nm laser), which enables the study of defects distribution and corresponding statistical analyses, with a sub-micron accuracy.

1.6 The Objectives of This Dissertation

In this dissertation, we aim to apply spatially resolved spectroscopy techniques to two different material systems, with primary focus on the first one. For material system 1, it includes two types of T2SLs based on either InAs/GaSb or InAs/InAsSb: the former one with no common atoms at the interfaces but both components are binaries, whereas the latter one with common interface atoms but with one component being a ternary alloy. The objectives are (1) to reveal and understand the unusual vibrational properties of the

InAs/GaSb T2SLs that have long been predicted but never been observed, and therefore demonstrate that Raman spectroscopy can be used as a non-invasive characterization technique to assess the quality and structure of this type of SL; (2) to study the vibrational properties of the new InAs/InAsSb T2SLs, and compared to the InAs/GaSb system. For material system 2, single crystalline CdTe epilayers, the objectives are (1) estimate the defect density levels in the epilayer and study the defect behaviors; (2) compare the PL results with those of other techniques, and correlate the PL dark spots with etch pits revealed by chemical etching.

CHAPTER 2: SAMPLES AND EXPERIMENTAL METHODS

In this chapter, we present sample information, as well as detailed experimental methods in this dissertation work. In section 2.1, we present sample information regarding the structure, composition and preparation process, covering all the three types of materials mentioned in Chapter 1: (1) various sets of InAs/GaSb T2SLs; (2) various sets of InAs/InAsSb T2SLs and InAsSb alloy; and (3) CdTe epilayers with varying defect density levels. In section 2.2, we present the information for Horiba HR 800 Raman microscope system that is the primary experimental system for this work. In section 2.3, we present methods that have been applied in data processing and calibration. In section 2.4, we present a brief description regarding other experimental techniques that have been used in this dissertation work.

2.1 Sample Information and Sample Preparation

2.1.1 InAs/GaSb and InAs/InAsSb T2SLs

There are several sets of samples investigated in this dissertation. These samples are different from each other in aspects such as growth technique, SL structure, composition, and so on. Based on similarities in structure and growth method, we divide these samples into different sets, and give the information of each set in a proper order.

(1) InAs/GaSb T2SL samples grown by MOCVD technique

This set of samples include the ones with notations G22, G30, G54 and G55, with detailed information given in Table 2.1. Throughout this dissertation work, all the MOCVD

samples were epitaxially grown in a Thomas Swan MOCVD reactor system by our collaborators, Prof. Dupuis' group at Georgia Institute of Technology [117].

Table 2.1: Sample information for (3-2122, 3-2130, 3-2154 and 3-2155) series SL samples, grown by MOCVD. The sample notations used in this dissertation is indicated in bracket in the first column.

Sample number	SL structures	SL layer thickness (μm)
3-2122 (G22)	i SL (50 \times) InAs (5nm)/GaSb (3.1 nm)	0.4
3-2130 (G30)	p SL (60 \times) (Doping: 2e18 to 1e16); i SL (200 \times); n SL (60 \times) (Doping: 1e16 to 1.5e18) InAs (4.8nm)/GaSb (3 nm)	2.5
3-2154 (G54)	p SL (60 \times) (Doping: 3.75e18 to 1e16) ; i SL (200 \times); n SL (60 \times) (Doping: 1e16 to 2e18) InAs (5.45nm)/GaSb (2.43 nm)	2.5
3-2155 (G55)	p SL (60 \times) (Doping: 3.8e18 to 1e16) ; i SL (200 \times); n SL (60 \times) (Doping: 1e16 to 2e18) InAs (5.14nm)/GaSb (2.43 nm)	2.4

According to Table 2.1, these SL samples are different from each other in the thickness of individual InAs and GaSb layers, as well as the number of total periods. Besides, some of them are p-i-n structures for the purpose of device fabrication, with different doping levels. During the growth of these SLs, there is no intentional interfacial treatment applied. Thus, both InSb and GaAs interfaces were possible, resulting in GaAs and InSb bonds in the (110) plane. This interface condition is named as “neutral” interface. Considering that the Raman microscope system possesses a spatial resolution of better than

half micron, all samples except for G22 are suitable for the Raman measurement on the cleaved edge plane (110) or $(\bar{1}10)$, since the thickness of the SL layers are 2.4-2.5 μm . For G22, the thickness of the SL layer is only 0.4 μm . Thus, when examined from the cleaved edge plane, the SL signals were affected by the substrate to some extent, with SL features still resolvable.

In addition, it benefits to consider the strain condition in the T2SLs. Because the lattice constant of GaSb is larger than that of InAs, if the SL, as a whole, remains coherently strained by the substrate, the GaSb layers in the SL are expected to be in compressive strain on the plane perpendicular to the growth direction. This is an important point to keep in mind when analyzing the Raman modes in the SL, because any GaSb-like modes will likely to be blue shifted by the strain, compared to those in a free-standing GaSb. To serve as references, two $\sim 1\mu\text{m}$ thick epilayers of pure InAs and GaSb were grown, respectively, on InAs and GaSb substrate. They can be treated as bulk samples and have been used in comparison on the Raman spectra of T2SLs in this dissertation.

(2) InAs/GaSb T2SL samples grown by MBE technique

This set of SL samples include the samples with notations IFA, IFRA and IFRB [118]. These samples were grown by IQE and provided to us by Prof. Shun-Lien Chuang's group at University of Illinois at Urbana-Champaign. Different from the previous mentioned MOCVD SLs, the substrate of this set of samples is GaSb. Thus, InAs layers in SL are expected to be under in-plane tensile strain exerted by the GaSb substrate, which tends to cause red-shifts for InAs-like Raman modes.

The sample information is summarized in Table 2.2. Generally, these three samples share the same binary InAs/GaSb structures, with the thickness of individual InAs and

GaSb layers being 4.5nm and 2.4nm, respectively. On top of the GaSb substrate, a 500 nm GaSb p-type layer (doping level $\sim 1e18$) was grown to contact directly to the SL layers. Besides, on the top of the SL layers, there is a 20nm n-type InAs layer (doping level $\sim 1e18$) and 5nm GaSb capping layer (without intentional doping).

Table 2.2: Sample information for (IFA, IFRA, and IFRB) series SL samples, grown by MBE.

Sample notation	Detailed SL structure	Interfacial treatments
IFA	n SL (80 \times) (Doping: $2e17$ to $1e18$) p- SL (300 \times) (doped by Be); p SL (80 \times) (Doping: $1e18$ to $2e17$); InAs (4.5nm)/GaSb (2.4 nm)	neutral
IFRA		Thin InSb 2.4 \AA
IFRB		Thick InSb 4.0 \AA

Nominally, the only difference among this set of samples exists at the interface. Intentional interface treatments have been applied, ending up with different IF conditions in the three samples. For IFRA, a thin InSb IF is enforced, the thickness of which is 2.4 nm. On the other hand, for IFRB, a thicker InSb IF is enforced, with a thickness of 4 nm. For IFA, no intentional IF treatment was applied, thus lead to a neutral IF in the sample.

(3) InAs/InAsSb T2SL samples grown by MOCVD technique

This set of samples include three MOCVD InAs/InAsSb SL samples labeled as G87, G89 and G95, in our dissertation. They were grown on (100) GaSb substrates, with a 210nm GaSb buffer layer grown between the SL and substrate layers. In general, the total thickness of the SL layers are relatively small, ranging from 0.28~1 μm . In addition, no intentional Ga doping is applied to these samples. The detailed sample information is listed in Table 2.3 shown on next page.

Table 2.3: Sample information for (3-2287, 3-2289, 3-2295) series InAs/InAsSb SL samples, grown by MOCVD. The sample notations used in this dissertation is indicated in bracket in the first column.

Sample number	SL structures	SL layer thickness (μm)
3-2287 (G87)	InAs _{0.74} Sb _{0.26} (5.59 nm)/InAs (13.3nm) 30 \times SL	~ 0.57
3-2289 (G89)	InAs _{0.79} Sb _{0.21} (2.27 nm)/InAs (7.04 nm) 30 \times SL	~ 0.28
3-2295 (G95)	InAs _{0.763} Sb _{0.237} (4.80 nm)/InAs (5.29 nm) 100 \times SL	$\sim 1 \mu\text{m}$

(4) InAs/InAsSb T2SL samples grown by MBE technique

This set of samples include five MBE InAs/InAsSb SL samples, labeled as B1854, B1775, B1871, B1816, and B1818. These samples were grown by Prof. Yong-Hang Zhang's group at Arizona State University. The samples were grown on n-doped GaSb substrates, and the detailed SL structure information can be referred to in Table 2.4.

Table 2.4: Sample information for (B1854, B1775, B1871, B1816, B1818) series InAs/InAsSb SL samples, grown by MBE.

Sample notation	SL structure	SL thickness (μm)
B1854	InAs _{0.795} Sb _{0.205} (2.5nm)/InAs (8.1 nm) SL (284 \times)	3.0
B1775	InAs _{0.649} Sb _{0.351} (4.7nm)/InAs (15.3 nm) SL (48 \times)	0.96
B1871	InAs _{0.761} Sb _{0.239} (4.76nm)/InAs (5.24 nm) SL (90 \times)	0.9
B1816	InAs _{0.65} Sb _{0.35} (4.5nm)/InAs (15.3 nm) SL (48 \times)	0.95
B1818	InAs _{0.65} Sb _{0.35} (4.5nm)/InAs (15.3 nm) SL (48 \times)	0.95

In samples B1775, B1871, B1816 and B1818, the SL epitaxial layers are sandwiched by a 10nm AlSb layer on one side and 10nm AlSb layer capped by a 10nm GaSb layer on the other side. In sample B1854, the SL epitaxial layers are grown directly on the GaSb buffer layer, and capped by 100nm InAs layer. In sample B1854, B1775 and B1871, Ga is not intentionally doped into the InAsSb alloy layers in the SL layers. On the other hand, in sample B1816 and B1818, Ga have been intentionally doped into the InAsSb alloy layers. In B1816, in each SL period, Ga is doped into the center layer of the overall 4.5nm alloy layer, with the doping thickness goes to 2.5nm. In B1818, a delta Ga doping was applied: that is, doping of Ga is only applied at the interface of InAs and the alloy, and the doping thickness in both layers is to 0.5nm.

(5) InAsSb alloy samples by MBE technique

Table 2.5: Sample information for (B1784, B1810, B1814) series InAsSb alloy samples, grown by MBE.

B1784	B1810	B1814
10 nm GaSb	10 nm GaSb	10 nm GaSb
10 nm AlSb	10 nm AlSb	10 nm AlSb
1000 nm Bulk InAs _{0.91} Sb _{0.09} : Ga undoped	50 nm InAs _{0.91} Sb _{0.09}	50 nm InAs _{0.91} Sb _{0.09} :Ga 1e20cm ⁻³ doped
	900 nm Bulk InAs _{0.91} Sb _{0.09} : Ga 1e20cm ⁻³ doped	900 nm Bulk InAs _{0.91} Sb _{0.09} ; lattice matched to GaSb
	50 nm InAs _{0.91} Sb _{0.09}	50 nm InAs _{0.91} Sb _{0.09} :Ga 1e20cm ⁻³ doped
10 nm AlSb	10 nm AlSb	10 nm AlSb
500 nm GaSb buffer + n-GaSb sub	500 nm GaSb buffer + n-GaSb sub	500 nm GaSb buffer + n-GaSb sub

This set of samples include three MBE InAsSb alloy samples on GaSb substrate, labeled as B1784, B1810, and B1814, which were also grown by Prof. Yong-Hang Zhang's group. The detailed sample information, including the Ga-doping condition, could be referred to Table 2.5 shown in previous page.

2.1.2 Samples Information: CdTe Epilayers

A set of six CdTe epilayers were grown on Si (211) wafers by MBE provided by Dr. Yuanping Chen at Army Research Laboratory [104,119]. After passivation and removal of the oxide layer on the Si substrate, CdTe were grown onto the wafer, with the growth rate of $\sim 0.75 \mu\text{m/h}$. During the growth, the CdTe layers were annealed to 550°C , in order to decrease the defect density of the epilayers. Different number of annealing cycles were applied to these epilayers, which is intended to identify the optimal annealing condition.

Since we aim to use PL mapping to estimate the defect density and analyze the defect behavior, it is both necessary and beneficial to compare the PL results with those obtained from other techniques. To investigate the defect densities, two techniques, chemical etching and X-ray diffraction (XRD), were conducted beforehand [104]. These measurements were conducted on a separated piece of sample cut from the same piece that was used for PL mapping. In chemical etching, some triangular pits have been exposed on the surface. These etch pits are usually assumed to be dislocations, and typically measured by a quantity called etch pit density (EPD). The defect density is also often empirically associated with the XRD linewidth (FWHM = full-width at half maximum). The sample information, together with the corresponding FWHMs and EPDs, are briefly summarized in Table 2.6 (shown in next page).

Table 2.6: Characterization results of CdTe epilayers grown on Si (211) wafers.

Sample	Thickness (μm)	Growth Temperature ($^{\circ}\text{C}$)	XRD FWHM (arcsec)	Annealing Cycles N	EPD (10^7 cm^{-2})
32207	8.95	280.0	110	0	2.7
32707	8.8	280.0	86	2	1.6
40307	9	280.0	79	4	0.98
32807	8.8	280.0	56	6	0.13
32607	8.9	280.0	61	8	0.077
32307	8.8	280.0	58	10	0.043

2.2 Horiba LabRam HR 800 Confocal Micro-Raman Microscope

2.2.1 The Advantage of Confocal Microscope System

The principle of accomplishing confocal imaging was patented by Marvin [120], which aims to achieve sample imaging and analysis on a point-by-point basis. In a conventional microscope, samples under examination are usually illuminated by a light source over a macroscopic area of the sample. Consequently, the signals to be collected are also resulting from a macroscopic area. The basic idea of confocal imaging includes two aspects: (1) Excite the sample by a point light source, thus only a limited region of the sample is excited and will finally contribute to the collected signal; (2) Place a pinhole in the conjugate focal plane of the sample plane, so that the signals from the regions beyond the excitation site are blocked by the pinhole and prevented from being collected by the detector. Therefore, by using a confocal system, better spatial resolution is achieved in measurements.

2.2.2 Horiba LabRam HR 800 Confocal Micro-Raman Microscope: General Information

This microscope system is an integrated Raman microscope system, which is manufactured by Horiba Jobin Yvon Inc., Edison, NJ. Below, we will abbreviate the system as “HR 800 Raman system” or “Micro-Raman system”. This system has a built-in

632.8nm laser as an internal excitation source, and also allows additional external lasers to be installed as extra excitation sources. Our system currently has 632.8 nm, 532 nm, 441.6 nm, 325 nm lasers as excitation sources.



Figure 2.1: Photo of HR 800 Raman system showing the front interface.

In Figure 2.1, a picture of the HR 800 Raman system is shown. On top of the microscope system is the optics compartment, where various optic components are installed to steer the excitation beam and collected signal. Additional optical components can be inserted in the optics compartment, such as a polarization rotator to control the excitation beam polarization, and an analyzer to select the polarization of the collected signal. The objective lens is located in the front of the system, under which the sample stage is installed.

Before presenting the details regarding the components inside the optical compartment, which are to be presented in the next section, we will firstly introduce the two parameters of the HR 800 Raman system that are most important to users: the spatial resolution and spectral resolution.

(1) Spatial resolution

This micro-Raman system is a confocal microscope system coupled with a spectrometer equipped with a CCD detector. The spot size of the focused laser beam can be approximated by the diffraction limit beam size given by the following equation:

$$d = 1.22 \frac{\lambda}{NA} \quad (2.1)$$

where NA is the numerical aperture of the objective lens being used, and λ is the wavelength of the excitation laser. The spatial resolution is approximately one half of the beam size or $d/2$ [121].

For instance, in most of our Raman studies, we used the 532nm green laser and a 100× objective lens with its NA being 0.9. This combination gives a spatial resolution $\sim 0.36 \mu\text{m}$ ($d/2$), which is below one half micron. Therefore, this system could unambiguously extract the Raman signals of the SL layers from the cleaved edge plane, when the total SL layer thickness is not much below $1 \mu\text{m}$. Correspondingly, the obtained Raman spectra will not be affected by signal originating from the substrate or buffer layers. Thus, by referring to the sample information presented in section 2.1, we are ensured that our Raman system is suitable to examine most of the SL samples from the cleaved edge. However, for the SL samples G87 and G89, which have relatively thin SL layers, the collected Raman signals will be a combination of those from both SL layers and substrate layers.

(2) Spectral resolution

The spectral resolution of the micro-Raman system is influenced by several factors, for instance, the wavelength of excitation laser, the grating inside the spectrometer, and so

on. In our Raman measurements, the spectra resolution is typically better than 0.5cm^{-1} , by using a $1200/\text{mm}$ grating and 532nm excitation laser.

2.2.3 Detailed Information of Optics Components in Optical Compartments

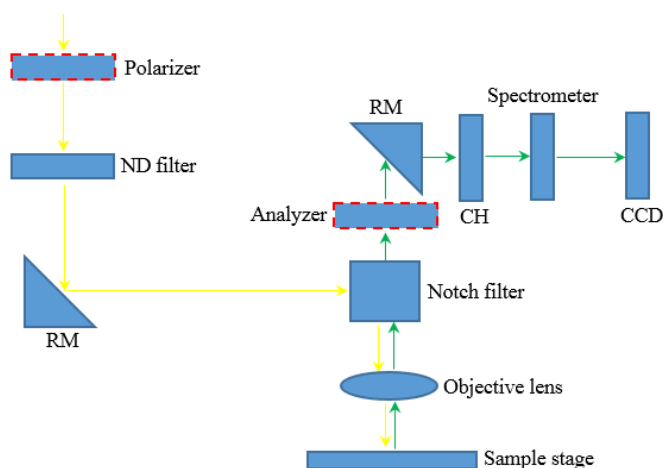


Figure 2.2: Schematic diagram showing light propagation inside the Raman system. RM stands for reflection mirror, CH stands for confocal hole. The “Polarizer” is a $\lambda/2$ plate. The dotted rectangles for polarizer and analyzer indicate that these two components will be removed when un-polarized Raman measurements are conducted.

Figure 2.2 shows schematically several key optical components that are closely related to light (either the excitation laser or the Raman signal to be collected) propagation inside the Raman system. It should be noticed that some optical components have been neglected for the sake of clarity. In the figure, the yellow arrows show the propagation of the excitation laser, while the green arrows show that of the to-be-collected signal. Below, we will track the light propagation inside the Raman system, in detail.

The linearly polarized excitation laser (shown as yellow arrows in the figure) is firstly incident on a $\lambda/2$ wave plate, which can rotate the polarization of laser to a selected direction. After this component, the laser is incident on a neutral density (ND) filter, which is supposed to reduce the laser power to a desired level. Then laser is deflected by a high-

reflection mirror, which then is incident on the notch filter corresponding to the laser line. This notch filter reflects the laser beam into the objective lens, which finally incident onto the sample stage and excite the sample through light-material interaction.

The Raman signals (indicated by green arrows), which is emitted by the sample, will firstly be collected by the objective lens, then be directed onto the notch filter. Unlike the excitation laser line, the Raman signals could transmit from the notch filter. After that, the signals will pass through the confocal hole and be incident on the grating and dispersed onto the CCD, which converts the Raman signals into digital data of a spectrum and send the data to computer for further analysis. Below, detailed information regarding each of the optical components is presented.

(1) Neutral density (ND) filter

This ND filter is intended to reduce the laser power to different levels. Filters with different attenuation levels are installed on a circular filter mount, while the selection of any specific filter can be controlled through software by the computer. The attenuation is indicated as D_x in the software interface controlling the Raman system. The power ratio between the incident laser (I_i) and the transmitted laser (I_o) is expressed by the following formula:

$$I_o = I_i/10^x \quad (2.2)$$

In our system, the installed filters offer x values of 0, 0.3, 0.6, 1, 2, 3, and 4; which provides a variety of excitation laser powers. For instance, if we choose the D1 filter, the output laser will be expected to be 1/10 of the input laser. On the other hand, if we choose the D3 filter, the output laser will be expected to be 1/1000 of the input laser, usually

resulting in excitation power in μW range. This allows power-dependent measurements, and becomes especially necessary when the damage threshold of sample is relatively low.

(2) Polarizer

The polarizer is a $\lambda/2$ wave plate that can change the polarization direction of the incident laser, which is linearly polarized in our work. The polarizer is suitable to be used with a wavelength range of 400~700nm, and the rotation range is 0~360°. In our work, we typically set the wave plate to be at 0° or 45°, which correspondingly sets the two laser polarization directions to be perpendicular to each other, in the plane of sample stage. By carefully aligning the sample, these two laser polarization directions are to be either parallel or perpendicular to one edge of the sample. For instance, in back-scattering measurements conducted at (001) plane, the samples are aligned such that one of the laser polarization direction is usually the [110] direction of the sample, while the other being the $[\bar{1}10]$ direction. In section 2.3, the polarization directions selected by the polarizer and the analyzer will be discussed in detail.

(3) Notch filter

It is mentioned in Chapter 1 that Raman signals are very weak, as compared to the excitation laser. Thus, it is important that the scattered laser signal (resulting from Rayleigh scattering) is prevented from entering into the spectrometer. The notch filter works like a reversed band-pass filter, which only blocks a small band width of light from passing through: in fact, the notch filter reflects it, and transmits the signals outside this small blocking band. Since the notch filter is wavelength specific, when we change the excitation laser, it is necessary to change the notch filter accordingly.

(4) Analyzer

Analyzer is a filter that only transmits signals of certain polarization direction and blocks signals of other polarizations. For the analyzer used in our work, it is suitable to be used in wavelength ranging from 350nm to 650nm. This analyzer has two polarization selections, which are perpendicular to each other. Since the analyzer is placed after the notch filter which only transmits the Raman signals, these two polarization selections correspond to the two possible polarizations of the collected Raman signals.

(5) Confocal hole

This confocal hole is installed to achieve confocal imaging of the system. The size of the hole is adjustable in a range from 0 to 1000 μ m, and is controlled by the computer. As the hole size is reduced, the spatial resolution may be improved to some degree (however, it is not ensured that decreasing the hole size will always lead to an improvement in spatial resolution), but the signals also become weaker as a trade-off. On the other hand, a larger hole size tends to result in stronger signals, but usually leads to a worsened spatial resolution. The usual hole size used in this dissertation is 250 μ m, if not otherwise mentioned.

(6) Grating

The grating is used to spatially disperse the collected signals of different wavelength. Two gratings are available in the system, with the groove density being 1200/mm and 2400/mm, respectively. They are installed on a motorized turret, which could be easily selected by the computer. The 2400/mm is supposed to give better spectral resolution, however, a considerable intensity decrease in the collected signals at the same time. If not otherwise mentioned, all the Raman and PL measurements are conducted by using the 1200/mm grating.

(7) Spectrometer

The spectrometer is an 800 mm focal length spectrograph, with an asymmetric Czerny-Turner configuration. Its spectral range is from 200nm to near IR.

(8) CCD

In our Raman system, the Synapse CCD detection system is installed for signal acquisition. This CCD system is manufactured by Horiba Jobin Yvon Inc., and offers two-dimensional photo-detection with high sensitivity, low noise level, and high reliability. The operating temperature is -70°C , which is achieved by thermoelectric air cooling method.

(9) Objective lens

There are several objective lens installed in the Raman system. They are different in aspects such as working distance, numerical aperture (NA), and magnification. By using different objective lens, different spatial resolutions are achieved. In this dissertation, we use a $100\times$ objective lens manufactured by Olympus. The lens' working distance is below 0.2mm and NA equals 0.9.

(10) Sample stage

The sample stage can be translated in X, Y and Z directions by software-controlled stepper motors. Thus, except for measurements conducted at any fixed site of sample, this stage also enables other types of measurements, such as mapping measurement at the sample surface (X-Y plane), or line scan measurements along X, Y or Z direction, respectively. In the X-Y plane the travel range is $100\times 100\text{ mm}^2$, with the minimum step size being $0.1\mu\text{m}$. For the Z direction, which is perpendicular to the sample stage, the travel range depends on the working distance of the objective lens, and the minimum step size is $0.5\mu\text{m}$.

(11) Software

The software used in our Raman system is LabSpec5, which provides an interface in the computer to operate the Raman system and conduct further data processing. It can conduct data acquisition under different modes, such as single spectrum acquisition, mapping acquisition and video image acquisition, etc. It also offers powerful data analysis options, such as baseline correction, peak fittings, and so on. Especially, in the mapping analysis features, it is able to present a map regarding a selected wavenumber or wavelength range. Thus, it is very convenient to conduct data analyses, such as analyzing intensity distributions for any wavenumber range of interest. Currently, a newer version of the software, LabSpec6 is available.

(12) Lasers

In our work, we use a Torus 532nm single frequency laser as the excitation source, which is manufactured by Laser quantum. This laser is a single mode (TEM00), linearly polarized laser, with a polarization ratio of >100:1. The original laser power is about 100 mW. Without using any attenuator, the laser power after the 100× microscope objective lens is ~30mW.

(13) Mechanical shutter

Stanford optical chopper (model number: SR 474) is used as an external shutter to block the laser from entering the Raman system. The shutter can be either synchronized with the data acquisition process using a TTL signal from the Raman system, or simply run independently at a set open window and duty cycle. The use of this shutter is extremely necessary when laser heating could affect the experimental results in an observable way. For instance, when it is synchronized with the CCD, it can block the laser while the CCD

is not taking data during the time interval when the sample stage is moving from one spatial point to another. When a very weak signal is to be measured, very long data collection time T_{data} is required (e.g., one minute). Setting the shutter to run at a frequency with a period $f_{\text{shutter}} \gg f_{\text{data}}$ ($f_{\text{data}} = 1/T_{\text{data}}$) will allow more time for heat dissipation, so as to reduce the sample heating effect.

2.3 Data Calibration and Processing

2.3.1 Frequency Calibration

To calibrate the frequency of our Raman system, a (100) Si wafer is used to calibrate the spectrometer so that it gives a Raman shift of 520.7 cm^{-1} , at room temperature. However, during measurements, it is observed that in single window measurements (thus there is no deliberate component moving inside the spectrometer), the Raman mode of Si may shift in a range of $\sim 0.2 \text{ cm}^{-1}$, in a duration of roughly 10 hours. This shift is attributed to (1) small mechanical drifts of the various components in the Raman system and (2) small drift of the excitation laser beam, which possibly leads to a slight alteration in the optical paths of both the excitation laser and the signal to be collected.

2.3.2 Intensity Calibration

(1) In Raman measurements

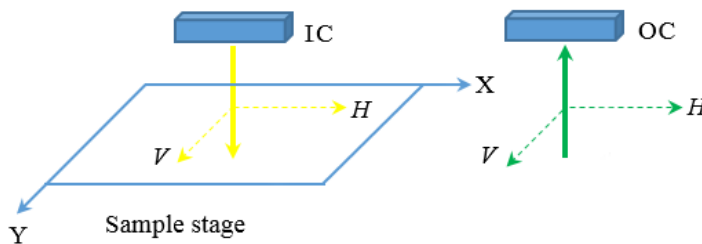


Figure 2.3: Polarization directions selected by polarizer and analyzer inside the optical compartment of the Raman system.

The intensity calibration is a little complex than the frequency calibration, when we conduct polarized Raman measurements. In Figure 2.3, we show the polarization directions that are selected by the polarizer and analyzer. The propagation direction of the excitation laser and collected Raman signal is indicated by solid yellow arrow and green arrow, respectively. The two possible polarization directions of laser, which are selected by the polarizer, are indicated by dotted yellow arrows. On the other hand, the two possible polarization directions of Raman signal, which are selected by the analyzer, are indicated by dotted green arrows. We name these two polarization directions to be “ H ” and “ V ”, for both laser and Raman signal. Since the system responds differently to light of different polarizations, we include two “virtual components” in the figure. The first one, named as IC (standing for input component), represents the system’s overall polarization-dependent response (PDR) to the input excitation laser; and the second one, named as OC (standing for output component), represents the system’s PDR to the collected Raman signal. In other words, we use IC to describe the overall PDR of our system in the laser incidence path; and OC to describe the overall PDR in the signal collection path. Note that a scrambler is supposed to eliminate the difference existing in the OC; however, in our case, it is found that it could not accomplish this goal very well. Thus, we decided to conduct a “manual” intensity calibration.

Under each scattering geometry, four polarization configurations are typically of interest to us. For intensity calibration purpose, we only need to care about the absolute direction of the polarizations: whether it is H or V . On the other hand, the relationship between the polarization direction and the crystal axes is not important. With respect to the translational sample stage, H matches the X direction of stage movement, and V matches

the Y direction. Here, instead of using Porto notations such as $z'(x', x')\bar{z}'$, we use the combination of H and V to indicate all the four polarization configurations that are possible: HH , HV , VH , and VV . For each of the notation, the first letter indicates the polarization direction of the excitation laser, while the second one indicates that of the collected Raman signal. To perform the intensity calibration, we divide the problem into two parts: (1) The laser incidence part, corresponding to the IC mentioned in previous paragraph; and (2) the signal collection part, corresponding to the OC.

(1) Laser incidence part

For the laser incidence part, the laser powers were measured with the laser polarized in either H or V direction. While the input laser power is kept the same, the power incident onto the sample stage will be slightly different. We used a power meter (based on a Si photo-diode, assumed to be symmetric between the two polarizations H and V) to measure the power at the sample stage, which in principle takes care of all the possible polarization dependent effects along the laser incidence path. It is neglected that a potential small change in polarization might occur due to the beam passing through multiple mirrors (in particular for the H polarization). Finally, the relationship between these two laser powers on sample stage, which are polarized in H and V , could be expressed in the following formula:

$$I_{Laser-H}:L_{Laser-V} = P_{HV} \quad (2.3)$$

where $I_{Laser-H}$ and $L_{Laser-V}$ stands for the measured power of the excitation laser, polarized in H and V direction, separately. And the parameter P_{HV} is obtained by a simple division, and its value has been found to be 1.6 for our system.

For the signal collection part, assume that a sample is emitting Raman signals with both H and V polarizations, and the two have the same intensities. However, after these signals are collected at CCD, due to the fact that the system transmission efficiencies are different for the two polarizations, the measured intensities are different. This situation could be expressed by the following formula:

$$I_{Raman-H}:L_{Raman-V} = Q_{HV} \quad (2.4)$$

where $I_{Raman-H}$ and $L_{Raman-V}$ stands for the Raman intensities for signals which are polarized in the H and V direction, respectively.

In order to determine Q_{HV} , we place a high quality (100) Si wafer on the sample stage, and carefully adjusting the orientation of the wafer such that the (110) direction (a cleaved edge) is parallel to either X or Y direction of the stage. Then we measured the Raman spectra in the two polarization configurations VV and HH . According to the selection rule of Si, the Raman peak intensities in these two configurations should be the same. We name these two Raman intensities that were actually measured as I_{Si-VV} and I_{Si-HH} , and the relationship of these two quantities could be expressed by:

$$I_{Si-HH}=I_{Si-VV} \times Q_{HV} \times P_{HV} \quad (2.5)$$

since P_{HV} is already known, we can immediately determine Q_{HV} , which has been found to be ~ 1.11 .

Suppose the Raman intensities in the four polarization configurations are I_{VH} , I_{VV} , I_{HH} , and I_{HV} . In order to directly compare them in terms of their relative intensities, we can correct them with respect to I_{VV} . The corrected intensities will be expressed by the following formulas:

$$I_{C-VH} = I_{VH}/P_{HV} \quad (2.6)$$

$$I_{C-VV} = I_{VV} \quad (2.7)$$

$$I_{C-HH} = I_{HH}/(P_{HV} \times Q_{HV}) \quad (2.8)$$

$$I_{C-HV} = I_{HV}/Q_{HV} \quad (2.9)$$

where the letter “C” in the subscript indicates the intensity has been corrected. These parameters have been further confirmed when we conducted back-scattering polarized Raman measurements on GaSb and InAs, from (001) plane. Theoretically, there is no anisotropy between the two directions [110] and $[\bar{1}10]$, which corresponds to the two directions H and V , in the sample stage plane. In experiments, it was found that the measured anisotropy was less than 1%, which could be attributed to the uncertainty of the measurements. In some cases, we were able to measure the polarization anisotropy by rotating the sample with the sample sitting on a rotational stage. In this case, no correction is required by measuring the spectrum under one fixed polarization configuration: for instance, VV . However, care is needed to make sure the same sample point is measured when the sample is being rotated.

(2) In PL measurements

A baseline subtraction is applied to the PL mapping results, by using the analysis feature provided by the software.

2.4 Other Techniques

(1) SEM imaging

The SEM image was obtained by using a Raith 150 Direct Write E-beam lithography system, which was manufactured by Raith USA Inc., Islip, NY. This system is a lithography tool with an ultra-high resolution. It also has the capability to conduct high resolution SEM imaging, which is our major purpose to use this equipment.

(2) Laser power measurement

The laser power is measured by a compact power and energy console manufactured by Thorlabs, with a part number PM100D. It is capable to measure the power of a monochromatic light source by selecting the wavelength of the light source. The measurable power range is from $0.01\mu\text{W}$ to 50 mW .

CHAPTER 3: RAMAN STUDY ON LATTICE VIBRATION MODES IN InAs/GaSb T2SLS

3.1 An Overview

In this chapter, we present results from micro-Raman study on a series of InAs/GaSb T2SL samples, as well as thick InAs and GaSb epilayers, from both the (001) growth plane and (110) or ($\bar{1}10$) cleaved edges in back-scattering geometry. The SL samples are grown on either InAs or GaSb substrate, while the thick InAs and GaSb epilayers are considered to behave in very similar ways with the corresponding “bulk” materials. It is worthwhile to note that, in order to assign those observed Raman modes, it is critical to use SL samples with two types of substrates and two “bulk” reference samples. On one hand, changing substrate is equivalent to applying strain to the SL, thus providing us an opportunity to examine how the Raman modes respond to strain, which can help to identify their origins. On the other hand, it is found that the Raman cross-sections (RCs) of the two constituents are very different. Hence, by making direct comparison between the “bulk” and SL samples, we can access the relative RCs of different modes, which also help to reveal their identities. Furthermore, polarization analyses allow us to determine the symmetry of the observed Raman mode.

By performing selection rule analyses and comparing two sets of samples as well as making direct comparison with the “bulk” references, we (1) conclude that the previously reported SL-LO phonon mode was a GaSb QC-LO mode, and anticipated InAs C mode is not observable due to a small InAs RC; (2) observe a set of new TO Raman lines

with characteristics of QC, EX, and IF modes. This work for the first time experimentally reveals the signatures of the unique vibration spectrum of the T2SL, and thus provides bench-mark data to test the theory.

3.2 Experimental Details for Raman Measurements

(1) General description

The back-scattering Raman measurements have been conducted at room temperature, by using the Torus 532nm laser. The laser spot size was about $0.72\mu\text{m}$ with the $100\times$ objective lens, thus corresponds to a spatial resolution $\sim 0.36\mu\text{m}$. An excitation laser power $\sim 0.3\text{mW}$ (achieved with ND filter setting to be D2) has been found to be an appropriate laser power not to cause significant sample heating for these SL samples. D1 level excitation (achieved with ND filter setting to be D1), which corresponds to a laser power $\sim 3.4\text{mW}$, was also used in some samples to examine the heating effects. Single point Raman measurements were conducted on the sample surface at areas free of visible defects. In these measurements, single window Raman spectra mode was used, which covers the wavenumber range 50cm^{-1} - 900cm^{-1} . Because there is no grating motion from one data collection to the other, a small peak shift can be observed without the influence of the mechanical backlash.

(2) Polarization configurations in Polarized Raman measurements

In this dissertation work, three scattering geometries are concerned: (001), (110) and $(\bar{1}10)$ back-scattering. Thus, there are twelve polarization configurations in total, which is list below in Table 3.1. In this work, if the polarization direction of the excitation laser and Raman signals are parallel, then we name the polarization configuration as “parallel polarization configuration”. On the other hand, if the two polarization direction

are perpendicular to each other, we name the polarization configuration as “cross polarization configuration”.

Table 3.1: Possible polarization configurations in (001), (110) and $(\bar{1}10)$ back-scattering geometries.

Scattering geometry (back-scattering)	Polarization configurations			
(001) plane incidence	$z'(x', x')\bar{z}'$	$z'(y', y')\bar{z}'$	$z'(x', y')\bar{z}'$	$z'(y', x')\bar{z}'$
(110) plane incidence	$x'(y', y')\bar{x}'$	$x'(z', z')\bar{x}'$	$x'(z', y')\bar{x}'$	$x'(y', z')\bar{x}'$
$(\bar{1}10)$ plane incidence	$y'(x', x')\bar{y}'$	$y'(z', z')\bar{y}'$	$y'(x', z')\bar{y}'$	$y'(z', x')\bar{y}'$

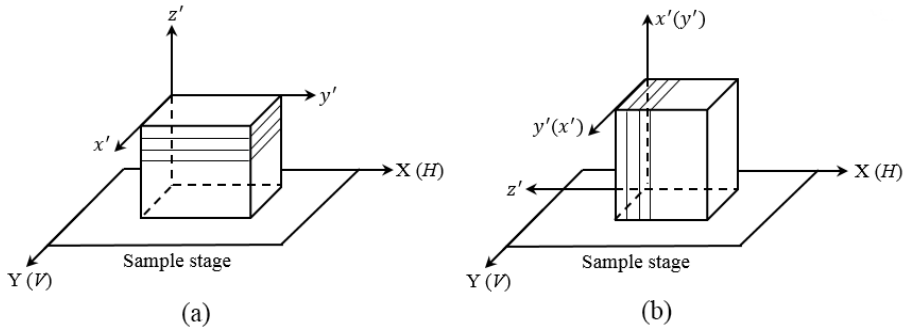


Figure 3.1: Polarization configurations in back-scattering polarized Raman measurements conducted on (a) (001) plane; and (b) (110) and $(\bar{1}10)$ plane. The polarization configuration for $(\bar{1}10)$ incidence is indicated in the bracket.

In experiments, samples are carefully aligned to reach the desired condition with respect to the Raman system, which is shown in Figure 3.1. However, due to the fact that for most of the samples received, the two directions $[110]$ (x') and $[\bar{1}10]$ (y') have not been determined. Thus, there are two possible situations when aligning the samples: for instance, in the (001) case, the x' may coincide with the stage direction X or perpendicular to it (thus coincide with direction Y). In Figure 3.1 (a), we only show one possible case: that is, the

x' direction of sample coincides with the stage direction Y. The other possibility, x' direction of sample coincides with the stage direction X, is not shown in the figure.

On the other hand, as was mentioned in Chapter 2, both polarizer and analyzer are used to select the polarization directions of excitation laser and Raman signal. In each of the scattering geometry, four polarization configurations are possible: HH , HV , VH , and VV . However, due to the fact that we cannot distinguish x' and y' direction, we cannot ensure a one-by-one correspondence between these notations and the Porto notations. For instance, the spectra with notation HH may correspond to $z'(x',x')\bar{z}'$ or $z'(y',y')\bar{z}'$. However, it is found that for all these samples, the spectra are very similar between $z'(x',x')\bar{z}'$ and $z'(y',y')\bar{z}'$, and so for $z'(x',y')\bar{z}'$ and $z'(y',x')\bar{z}'$. In (110) and ($\bar{1}10$) cases, such similarity is also observed, which could be conveniently referred to by Table 3.1: for these two cleaved edge incidence cases, if the polarization configurations lie in the same column, then similarity will always be shown in spectra between the two. Here, the similarity means that we don't need to distinguish [110] and [$\bar{1}10$] direction, for the purpose to assign the resolved phonon modes. Thus, in the following discussions on Raman spectra, if the purpose is to assign the phonon mode, we will still use the Porto notation.

However, the situation will be a little complex when Raman measurements are conducted to explore any anisotropy. Without being able to distinguish [110] or [$\bar{1}10$], we are still able to observe whether one direction/plane shows stronger mode intensity. The only deficiency is that we are not able to figure out, for instance, whether the direction showing stronger mode intensity is [110] or [$\bar{1}10$], if anisotropy exists. Thus, in these anisotropy-related measurements, we will use the notations such as HH and VV , instead of Porto notation.

(3) Spectrum acquisition

For spectrum acquisition, two parameters, exposure time (T) and accumulation number (N) are used, which indicates how the final spectrum is obtained. During each duration of T , a spectrum is obtained and saved to the computer. This process is repeated to reach a total of N times, and the final spectrum is the averaged one over these separated spectra. Both T and N can be set in the software interface. For D2 laser Raman measurements discussed in this chapter and Chapter 4, if not otherwise mentioned, the usual data acquisition parameters were $N=40$ and $T=20$ seconds.

3.3 Some General Observations and Comments

To investigate lattice vibration modes in InAs/GaSb T2SLs, we have studied seven SL samples in total, and thus obtained a large number of Raman spectra. One would be overwhelmed if we try to compare all these samples simultaneously. In order to make the comparison clear and comprehensive, before presenting detailed results regarding the phonon modes observed in SL samples and making assignments, we will firstly show some general observations and comments in this section, as a preparation for the next section.

(1) General consideration on SL spectra, from (001) back-scattering geometry

Figure 3.2 (to be shown on next page) shows a typical set of Raman spectra of a SL sample (G54) obtained under (001) back-scattering geometry. Under this scattering geometry, we have conducted Raman measurements using four polarization configurations: $z'(x',x')\bar{z}'$, $z'(x',y')\bar{z}'$, $z'(y',x')\bar{z}'$ and $z'(y',y')\bar{z}'$. In each of the polarization configuration, two phonon modes are observed, which is resolved $228\sim 228.4\text{cm}^{-1}$ and $238\sim 238.6\text{cm}^{-1}$, respectively. It was found that the spectra of $z'(x',x')\bar{z}'$ and $z'(y',y')\bar{z}'$ are very similar; and so are the spectra of $z'(x',y')\bar{z}'$ and $z'(y',x')\bar{z}'$. These similarities

can be seen by comparing the corresponding spectra from panel (a) and (b) in Figure 3.1. However, there are big differences in the mode intensities between the parallel and cross polarization configurations: the intensities in the two parallel polarization configurations are much larger than those in the two cross ones. For the 238~238.6 cm^{-1} mode in $z'(x',x')\bar{z}'$ and $z'(y',y')\bar{z}'$, the intensities are 1.4~1.5 cps (counts/second), whereas in $z'(x',y')\bar{z}'$ and $z'(y',x')\bar{z}'$, ~0.2 cps. A similar observation could be made for the 228~228.4 cm^{-1} mode, although the intensity difference is somewhat smaller.

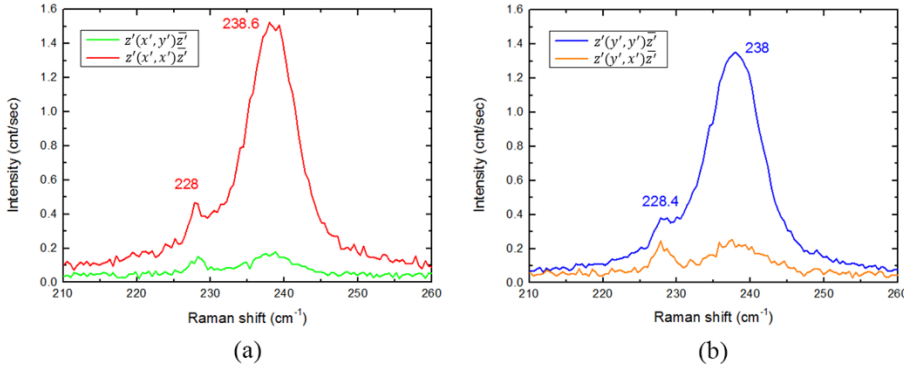


Figure 3.2: Comparing (001) back-scattering Raman spectra of InAs/GaSb SL sample G54, under four polarization configurations: (a) $z'(x',x')\bar{z}'$ and $z'(x',y')\bar{z}'$, and (b) $z'(y',y')\bar{z}'$ and $z'(y',x')\bar{z}'$.

The above observations are consistent with the Raman selection rules presented in Table 1.1, as described in Chapter 1. According to the selection rules, only LO modes are allowed in the two parallel polarization configurations, while forbidden in the two cross ones. Thus, these two observed modes are LO modes, with their intensities much weaker in the two cross polarization configurations.

In the two allowed polarization configurations $z'(x',x')\bar{z}'$ and $z'(y',y')\bar{z}'$, the Raman intensities for LO modes are proportional to either a_{LO}^2 or b_{LO}^2 . Due to the fact that

the two Raman tensor elements a and b are originated from the same tensor element with D_{2d} symmetry, it can be expected that the difference between a^2_{LO} and b^2_{LO} will not be very big. This is in consistency with the similarity of the two spectra obtained under $z'(x', x')\bar{z}'$ and $z'(y', y')\bar{z}'$. On the other hand, the non-zero intensities for the LO modes in the forbidden polarization configurations could be mainly due to two facts: (1) There is a small deviation of the actual incidence direction of excitation laser from the desired z' direction. (2) There are disorders introduced to the SL sample during growth.

Overall, the general observations and comments above hold for all the SL samples we have examined. That is, for all the seven SL samples, two modes are resolved, with the corresponding intensities being much larger in the two parallel polarization configurations than the two cross ones.

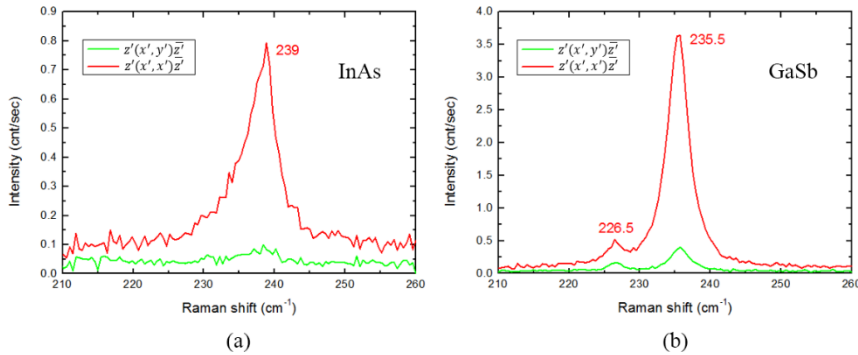


Figure 3.3: Comparing (001) back-scattering Raman spectra in polarization configurations $z'(x', x')\bar{z}'$ and $z'(x', y')\bar{z}'$ for bulk materials: (a) InAs, and (b) GaSb.

As a further confirmation of the Raman selection rules, the spectra of InAs and GaSb are presented in Figure 3.3. Due to the similarity in spectra between $z'(x', x')\bar{z}'$ and $z'(y', y')\bar{z}'$, as well as that between $z'(x', y')\bar{z}'$ and $z'(y', x')\bar{z}'$, only the spectra in $z'(x', x')\bar{z}'$ and $z'(x', y')\bar{z}'$ are shown, for the sake of brevity. Since both these two bulk

materials belong to the symmetry group T_d , according to the selection rules, LO modes are allowed in the two parallel polarization configurations and forbidden in the two cross ones. On the other hand, TO modes are always forbidden. Accordingly, a mode $\sim 239\text{cm}^{-1}$ is resolved in InAs, with the mode frequency matches that of the InAs LO mode [122,123]. Similarly, a mode $\sim 235.5\text{cm}^{-1}$ is resolved in GaSb, matching quite well to the GaSb LO mode in previous results [124]. The intensities for these two modes are much stronger in the parallel configurations than the cross ones, which is clearly shown in the figure. In addition, we are able to resolve a much weaker mode at $\sim 226.5\text{cm}^{-1}$ in GaSb [125], which is the forbidden GaSb TO mode. Also, the Raman intensities are expected to be the same in $z'(x', x')\bar{z}'$ and $z'(y', y')\bar{z}'$, since both the RCs are proportional to $\sim d_{\text{LO}}^2$. This has also been confirmed in our measurements, which will be presented in section 3.3.

(2) General consideration on selection rules for (110) or $(\bar{1}10)$ backscattering geometry

Firstly we note that for the samples we received, [110] and $[\bar{1}10]$ crystallography directions were unfortunately not marked. Therefore, in this work, when not making comparison between the two orientations, we will generally refer to the cleaved edge being studied as the (110) plane; when it is necessary to make comparisons between the two cleaved edge planes, we will then refer the other orthogonal plane as $(\bar{1}10)$ plane. In short, we can examine the possible anisotropy between the two orientations, but cannot tell which one is which. For instance, we are able to observe the RC of specific mode is larger in one plane than in the other one; however, we cannot tell whether the plane of larger RC is (110) or $(\bar{1}10)$ plane. This way of notation also applied to chapter 4, if not otherwise indicated.

Before discussing those Raman spectra obtained in this (110) back-scattering geometry, we want to firstly demonstrate the ability of our Raman system to extract the Raman signals of SL layers on the cleaved edge plane, without any ambiguity.

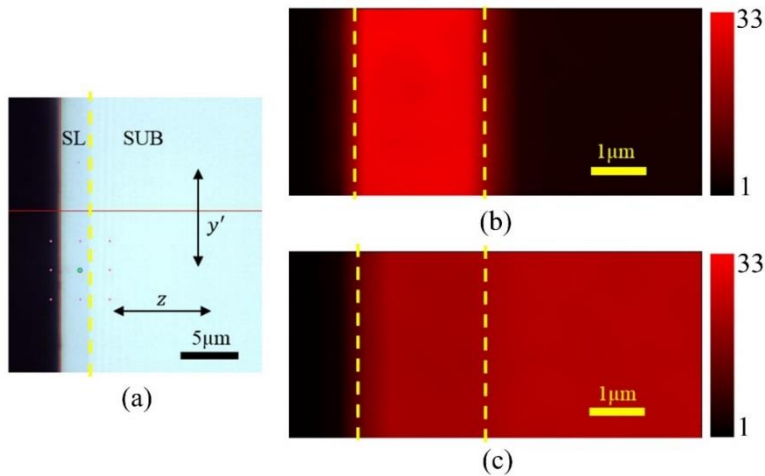


Figure 3.4: Raman spectra and mapping result from the (110) cleaved edge of an InAs/GaSb SL sample grown on InAs substrate (G55). This figure shows the ability to resolve unambiguously the signal from the SL and substrate: (a) optical image under white light illumination, (b) Raman mapping result for the SL mode $\sim 226\text{cm}^{-1}$ that does not exist in the substrate, and (c) Raman mapping result for the mode $\sim 217.5\text{cm}^{-1}$ that exist in both the SL layers and the substrate.

In Figure 3.4 (a) we show an optical image of the cleaved edge plane under white light illumination, showing a visible optical contrast between the SL and substrate, which clearly indicates the boundary between SL and substrate and is emphasized by the yellow dotted line. In Figure 3.4 (b) and (c), we show Raman mapping results on the cleaved edge, in correspondence to two modes resolved in SL layers: $\sim 226\text{cm}^{-1}$ and $\sim 217.5\text{cm}^{-1}$. The mode $\sim 226\text{cm}^{-1}$, as concerned in (b), is a SL EX-TO mode (the assignment of which will be discussed in the next section), which is resolved only in the SL epilayer region. Accordingly, we can see that the map of intensity distribution in (b) shows a clear boundary,

and the intensity on the left side of the boundary is apparently much larger than that on the right side. On the other hand, the mode $\sim 217.5\text{cm}^{-1}$, as concerned in (c), is an InAs QC-TO mode of the SL. This mode is located at nearly the same frequency as that of the bulk InAs TO mode of the InAs substrate. Accordingly, it is observed that the intensity distribution across the SL/substrate boundary is rather uniform, with no apparent boundary. We note that the results shown on Figure 3.4 were obtained at excitation laser power level of D1 to save the time required for Raman mapping.

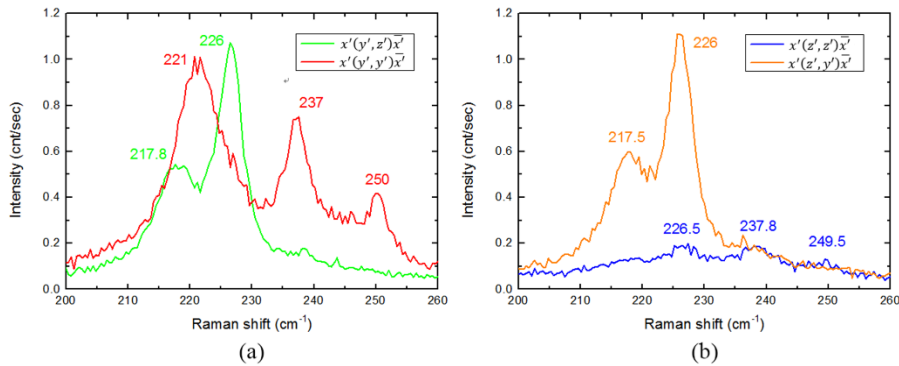


Figure 3.5: Comparing (110) back-scattering Raman spectra of InAs/GaSb SL sample G54, under four polarization configurations: (a) $x'(y', z')\bar{x}'$ and $x'(y', y')\bar{x}'$; and (b) $x'(z', z')\bar{x}'$ and $x'(z', y')\bar{x}'$.

In Figure 3.5, we present a set of Raman spectra belong to the SL sample G54 (the same as shown in Figure 3.2), obtained under (110) back-scattering geometry. We need to recall that according to Raman selection rules, only TO modes are allowed in the (110) incidence case, while the intensities of these modes will depend on the polarization configuration. Thus, it is reasonable to deduct that all the modes resolved in the spectra with considerable mode intensities should be TO modes.

In the two cross polarization configurations $x'(y', z')\bar{x}'$ and $x'(z', y')\bar{x}'$, two modes are resolved, locating at $217.5\sim 217.8\text{cm}^{-1}$ and $\sim 226\text{cm}^{-1}$. Also, it is found that the two spectra are very similar to each other, which could be referred to the corresponding spectra in panel (a) and (b) of Figure 3.5. This can be explained by Raman selection rules, which indicate that the RCs under these two polarization configurations are both proportional to f^2_{TO} .

In the two parallel polarization configurations $x'(y', y')\bar{x}'$ and $x'(z', z')\bar{x}'$, on the other hand, the situation is rather different. In the former configuration, basically three modes are resolved, locating at $\sim 221\text{cm}^{-1}$, $\sim 237\text{cm}^{-1}$, and $\sim 250\text{cm}^{-1}$. These modes have considerable intensities, which are proportional to $\sim b^2_{\text{TO}}$, according to the Raman selection rules. In the latter configuration, also three modes are resolved, locating at $\sim 226.5\text{cm}^{-1}$, $\sim 237.8\text{cm}^{-1}$, and $\sim 249.5\text{cm}^{-1}$; however, with much weaker mode intensities. This is attributed to the fact that the RC under $x'(z', z')\bar{x}'$ is proportional to $\sim c^2_{\text{TO}}$, which is supposed to have a very small magnitude.

In addition, the spectra obtained from $(\bar{1}10)$ backscattering geometry are found to be very similar to spectra mentioned above for (110). That is, the spectrum for $x'(y', y')\bar{x}'$ is very similar to that for $y'(x', x')\bar{y}'$; the spectrum for $x'(z', z')\bar{x}'$ is very similar to that for $y'(z', z')\bar{y}'$; and the spectra corresponding to the other four polarization configurations are also very similar. This experimental observation is also in consistency with the theoretical expectations summarized in Table 1.1. There are, however, some subtle differences, between the (110) and $(\bar{1}10)$ scattering geometry. The differences are related to the expected anisotropy between the [110] and $[\bar{1}10]$ direction in C_{2v} symmetry, which will be discussed in detail in the following section.

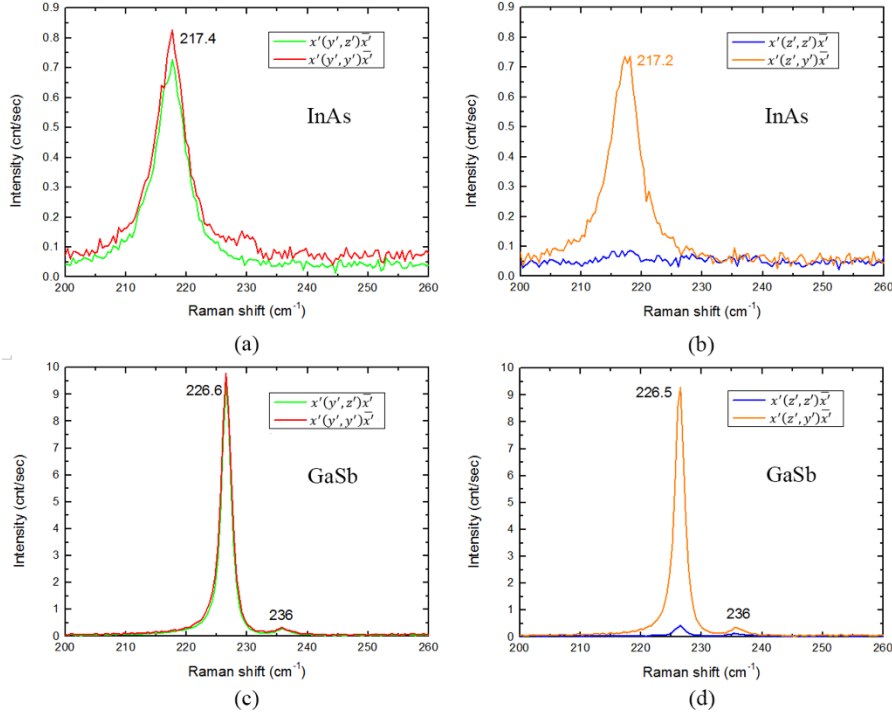


Figure 3.6: Comparing (110) back-scattering Raman spectra of InAs and GaSb bulk epilayers, in different polarization configurations: (a) InAs: $x'(y', z')\bar{x}'$ and $x'(y', y')\bar{x}'$; (b) InAs: $x'(z', y')\bar{x}'$ and $x'(z', z')\bar{x}'$; (c) GaSb: $x'(y', y')\bar{x}'$ and $x'(y', z')\bar{x}'$; (d) GaSb: $x'(z', y')\bar{x}'$ and $x'(z', z')\bar{x}'$.

Like in the (001) back-scattering case, the Raman selection rules are also confirmed by the spectra of bulk InAs and GaSb, as shown as Figure 3.6. Recall that for T_d group, only TO modes are allowed [126], under the three polarization configurations $x'(y', y')\bar{x}'$, $x'(z', y')\bar{x}'$, and $x'(y', z')\bar{x}'$, with equal intensity proportionalities $\sim d_{\text{TO}}^2$. Accordingly, we observe apparent similarities among the spectra of each bulk sample, in these three configurations. For GaSb, there are two modes resolved: the stronger mode (its intensity being larger than 9 cps) at 226.5~226.6 cm^{-1} is the GaSb TO mode, while the much weaker one (its intensity being smaller than 0.4 cps) is the theoretical forbidden GaSb LO mode [125-127]. As for InAs, the only mode that is clearly resolved is the InAs TO mode at

217.2~217.4 cm^{-1} . The forbidden LO mode is not resolved, which could be attributed to the overall smaller RC of this mode.

On the other hand, in $x'(z', z')\bar{x}'$, all modes are forbidden, which is also confirmed by the corresponding spectra. For instance, in GaSb, the TO mode at $\sim 226.5\text{cm}^{-1}$ has an intensity of ~ 9.3 cps in $x'(z', y')\bar{x}'$, which decreases to be less than 0.5 cps in $x'(z', z')\bar{x}'$.

(3) Comparing the SLs grown on same substrates

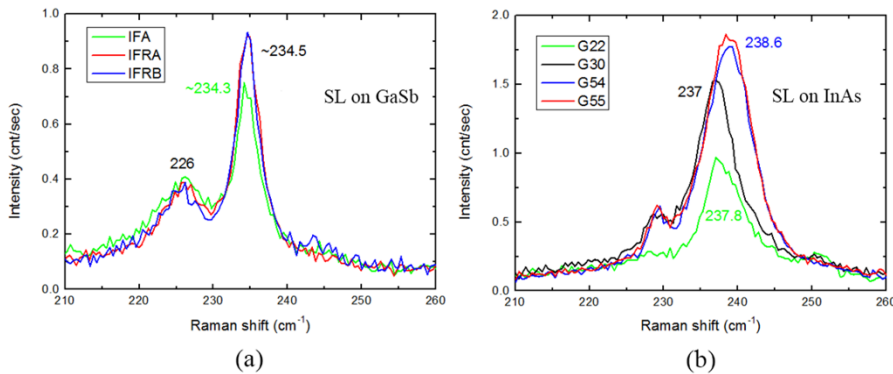


Figure 3.7: Raman spectra comparison for InAs/GaSb SL samples on the same substrate, obtained in $z'(x', x')\bar{z}'$: (a) SL on GaSb substrate, involving sample IFA, IFRA and IFRB; and (b) SL on InAs substrate, involving sample G22, G30, G54 and G55.

Figure 3.7 shows the comparison on Raman spectra obtained in $z'(x', x')\bar{z}'$, among SL samples grown on the same substrate. In Figure 3.7 (a), we compare the SL samples grown on GaSb, involving SL samples IFA, IFRA and IFRB. For these three samples, the thickness of the individual InAs and GaSb layers are nominally the same, and they are only different in the interfacial treatments that were applied. From the figure, we observe that the three spectra are very similar to each other. The major mode observed in SL is located at $\sim 234.5\text{cm}^{-1}$, and the frequency differences among the three SL samples are less than 0.5cm^{-1} . This great similarity in spectra among the SL samples on the same substrate

ensures us that it is reliable to pick one SL sample from the group of samples grown on the same substrate, and use the spectra as typical ones when comparing Raman spectra, for the purpose of assigning the observed phonon modes.

In contrast, when we compare the Raman spectra for the SL samples grown on InAs, which is shown in Figure 3.7 (b), the differences in spectra are more obvious. G22 has the lowest Raman intensities, for both the two resolved modes. This could be due to the fact that this sample has the thinnest SL layers ($\sim 0.5\mu\text{m}$). Thus, the volume which contribute to Raman signals is the smallest for G22, when compare to the other three samples, whose SL thickness is $2.4\sim 2.5\mu\text{m}$. Besides, we observe a much larger frequency differences in the major resolved mode when compared to panel (a), varying from $\sim 237\text{ cm}^{-1}$ in G30 to $\sim 238.6\text{ cm}^{-1}$ in G54 and G55. This larger difference in mode frequencies could be attributed to the structural differences in the SL period, since for these samples, the thickness ratios between individual InAs and GaSb layers are different. For instance, for sample G30, the thickness for individual InAs and GaSb layers are 4.8nm and 3nm , respectively; for sample G54, the thickness for the two layers are 5.45nm and 2.43nm . For sample G55, which has the similar spectrum as G54, the two thickness parameters are 5.14nm and 2.43nm . Despite the fact that the wavenumber difference shown in the SL samples grown on InAs substrate is larger, it is still sufficient to pick only one SL sample for the purpose of mode assignments.

Overall, within the samples grown on the same substrate (which could be either InAs or GaSb), the spectra for the samples are very similar to each other. However, slight differences are inevitable, which are due to differences in structural details, such as different strain in the samples and/or different interfacial treatments applied during SL

growth. These differences are extremely important when concerning the fine differences among the samples, but will not affect the discussions on mode assignments. Thus, under each polarization configuration, it is reasonable to pick only one sample from each set of SL samples, which is grown on either InAs or GaSb substrate, when trying to assign the observed Raman modes.

3.4 Micro-Raman Investigation on Lattice Vibration Modes in InAs/GaSb T2SL

Below we discuss the Raman mode assignments by applying polarization analyses and comparing the SL spectra with those of bulk references. Based on statements mentioned in section 3.3, we choose one SL sample on either InAs or GaSb substrate, and compare them with the corresponding spectra of InAs and GaSb reference samples.

3.4.1 (001) Back-scattering

(1) Lattice vibrations and phonon mode assignments

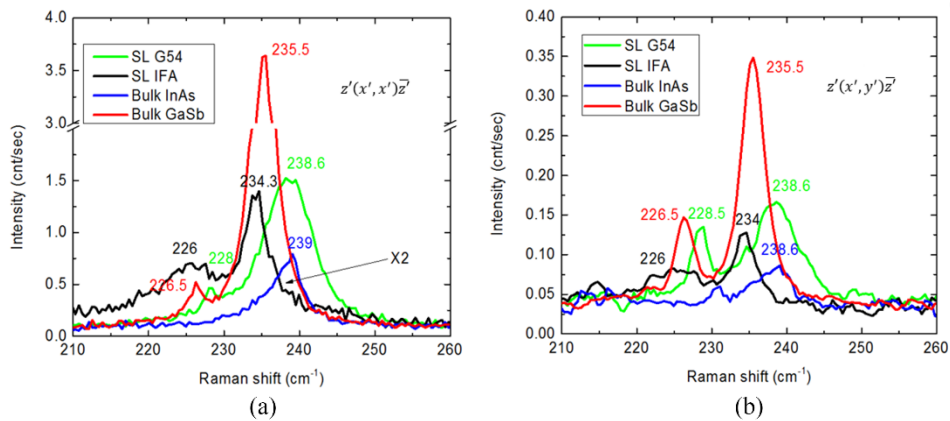


Figure 3.8: (001) backscattering Raman spectra of InAs/GaSb SLs, compared with those of InAs and GaSb thick epilayers in two polarization configurations: (a) $z'(x', x')\bar{z}$ and (b) $z'(x', y')\bar{z}$.

For the sake of brevity and clarity in presenting the data, in Figure 3.8, only the spectra of four samples are shown, which compares Raman spectra with two polarization

configurations $z'(x',x')\bar{z}'$ and $z'(x',y')\bar{z}'$. These samples are: G54 (T2SL on InAs substrate), IFA (T2SL on GaSb substrate), InAs, and GaSb.

First of all, it is beneficial to notice that the RC of GaSb is substantially larger than that of InAs, with a peak intensity ratio about 5:1 for their LO modes at 235.5cm^{-1} and 239cm^{-1} , respectively. This finding implies that the InAs-like modes are less likely to be observed than the GaSb-like modes in the SL samples, which is an important clue for identifying the SL Raman modes.

Second, the primary SL peak is found at $\sim 238.6\text{cm}^{-1}$ or $\sim 234.3\text{cm}^{-1}$ in the SL sample on InAs and GaSb substrate, respectively. The peak position varies only slightly within the SL samples on the same substrate (less than 0.5cm^{-1} when the structure of SL period stays the same), but greatly when the substrate changes, because of the different epitaxial strain in these two sets of samples. The SL mode resolved in sample IFA (T2SL on GaSb substrate) matches the predicted GaSb QC-LO mode, with a wavenumber slightly below that of the GaSb LO mode [46,63]. For the SL mode in sample G54 (T2SL on InAs substrate), despite the fact that it has a wavenumber close to that of InAs LO mode $\sim 239\text{cm}^{-1}$ [43], it is not appropriate to attribute this mode to the InAs C-LO mode that has been theoretically predicted [63]. This SL mode is, in fact, the same GaSb QC-LO mode as in the SL grown on GaSb, but has been blue shifted due to the compressive strain in the SL on InAs substrate. To exclude the possibility of this mode being the InAs C-LO, we can do a simple deduction: for the lowest order consideration based on the volume of GaSb in the SL samples, the peak intensity should be simply determined by the fraction of GaSb in the SL. Recall that the RC of GaSb LO modes in the bulk are much larger than that of InAs LO modes, since the SL mode in G54 (the SL sample on InAs substrate) shows an intensity

lies between that of the bulk GaSb and InAs, it is consistent with its assignment as a GaSb QC-LO mode. On the other hand, if it were an InAs C-LO mode, the intensity would be below that of the bulk InAs LO modes, which contradicts with the actual observation. Thus, this major SL peak is assigned as the GaSb QC-LO mode. According to the selection rules shown in Table 1.1, this mode should have A_1 symmetry. Besides, it is observed that for this mode, the peak resolved in the GaSb-substrate SL sample has a lower intensity when compared to the InAs-substrate SL sample. We note that there are additional cap layers in the GaSb-substrate SL samples (an InAs layer with a thickness of 20nm, and a GaSb layer with a thickness of 5nm), while there is no cap layers in the InAs-substrate samples. Thus, this intensity difference is mainly attributed to the absorption of excitation laser and Raman signals by the cap layers in the GaSb-substrate sample.

In addition to the major SL peak, a weaker peak at $\sim 228\text{cm}^{-1}$ in the SL sample on InAs substrate or $\sim 226\text{cm}^{-1}$ in that on GaSb substrate is observed. This peak has a wavenumber close to that of GaSb TO mode, and its small intensity may indicate that the mode is forbidden. By taking the Raman selection rules into consideration, this mode could be attributed to the forbidden GaSb derived TO mode. However, we are not able to exclude other possible assignments for this peak. When compared to the primary SL peak, the width of this peak is obviously larger and its relative intensity is enhanced, in particular for the SL on GaSb. Hence, this peak might also contain some unresolved EX modes. In addition, people have reported the observation of coupled LO phonon-intersubband plasmon modes, which resulting in a similar wavenumber, in InAs/GaSb quantum well [123]. In their results, the peak intensities is also enhanced as compared to the forbidden TO modes, and it is claimed that the peak intensity depends on both carrier concentration and the wavelength

of the excitation laser. Thus, the coupled LO phonon-intersubband plasmon mode could also contribute to the intensity of this mode.

In contrast to the clearly observed GaSb QC-LO mode, the predicted InAs confined modes [46,64] are not observed in our work. This could be possibly attributed to the small RC of InAs bulk. That is, since the InAs LO mode has a much smaller intensity than that of GaSb, the intensity of the InAs confined mode in SLs should be even smaller, thus it is not resolved in the spectra when Raman back-scattering is conducted on (001) plane.

(2) Possible anisotropy between $[110]$ and $[\bar{1}10]$ direction

As mentioned in previous discussion, due to the symmetry reduction from D_{2d} to C_{2v} , an anisotropy is introduced into the SL, between x' and y' : i.e., a_{LO} and b_{LO} , as shown in Table 1.1. On the other hand, in InAs and GaSb bulks with T_d symmetry, x' and y' should be equivalent, which is shown in Table 1.2. In spectra shown in the previous content, it is observed that the mode intensity may be different in the two parallel polarization configurations (for instance, in Figure 3.2, the intensity of the GaSb QC LO mode is different between $z'(x', x')\bar{z}'$ and $z'(y', y')\bar{z}'$), which may indicate the anisotropy between the $[110]$ and $[\bar{1}10]$ direction. However, there are some inevitable experimental uncertainties, such as the slight deviation of the actual sample orientation from the perfect $[110]$ or $[\bar{1}10]$ direction, alignments of the polarizer and analyzer, excitation laser power fluctuation, etc.; which consequently make the results less reliable. To minimize the uncertainty, we have decided to conduct a set of two measurements: (1) perform a Raman measurement with a fixed parallel polarization configuration, specifically, in the “VV” configuration; (2) rotate the sample by 90 degree, and conduct another Raman measurement on the same sample site, the configuration of which could be notated as “HH”.

To further test the accuracy and reliability, we also conduct these set of measurements on the InAs and GaSb bulk epilayers, which are expected to be isotropic. By following these procedures and comparing the mode intensities, we are able to examine the potential anisotropy. If the observed anisotropy is more significant than the accuracy based on the measurements performed on InAs and GaSb, the anisotropy is confirmed.

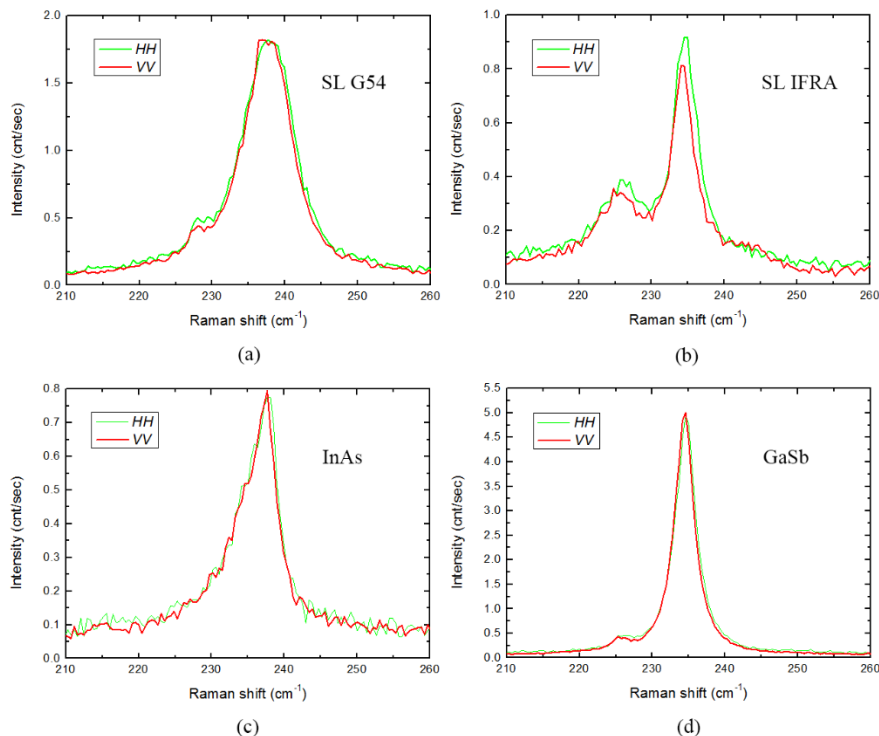


Figure 3.9: Comparison of Raman spectra measured in configuration *HH* and *VV* for (a) SL G55, (b) SL IFRA, (c) thick InAs epilayer, and (d) thick GaSb epilayer.

In Figure 3.9, we compare the spectra corresponding to *HH* and *VV* configurations, at (001) plane, involving two SL samples G55 (neutral-IF SL on InAs substrate) and IFRA (SL on GaSb substrate, with thin-InSb IF enforced), as well as the InAs and GaSb bulk epilayers. It should be noted that for the SL sample G55, there was no additional growth treatment applied to the interface during growth. Thus, the potential anisotropy could be

mainly attributed to the difference between a_{LO} and b_{LO} , and it is suitable to examine the symmetry deduction from D_{2d} to C_{2v} by using this sample. On the other hand, in IFRA, for instance, thin InSb IFs were enforced during the sample growth. This interfacial modification can be also examined more carefully with this approach to explore anisotropy.

By examining the allowed LO mode in InAs and GaSb, it is found that the anisotropy is not apparent for these two bulk materials, as expected. For instance, the anisotropy is very small (within 1%), as shown in panel (c) for InAs. At the same time, for the two SL samples, we also compare the intensity of the GaSb QC-LO mode between the two directions. In G55, it is found that the difference, if any, is less than ~1%, which is within the experimental uncertainty. Thus, we conclude that the anisotropy between the two Raman tensor element a_{LO} and b_{LO} is negligible, from the (001) plane. However, we observe some anisotropy in IFRA, which shows a difference ~10%. This intensity difference could not be attributed to the difference in a_{LO} and b_{LO} , but possibly related to the IF treatment applied to the SL.

3.4.2 (110) and $(\bar{1}10)$ Cleaved Edge Back-scattering

(1) Lattice vibrations and phonon mode assignments

Shown in Figure 3.10 (shown on next page) are the typical results for the two SL samples, respectively, on InAs and GaSb substrate, compared directly with the “bulk” references, obtained from one of the cleaved edge planes. Due to the similarity between the spectra obtained from two cleaved edges, only spectra from one of them are presented. Further comparison between the two cleaved edges will be presented later. As was mentioned previously, for T_d symmetry, TO modes are allowed in three equivalent configurations $x'(y', z')\bar{x}'$, $x'(z', y')\bar{x}'$, and $x'(y', y')\bar{x}'$, but forbidden in $x'(z', z')\bar{x}'$.

Accordingly, we observe that, for the “bulk” samples, a TO mode at $\sim 226.5\text{cm}^{-1}$ with a weak LO mode at $\sim 236\text{cm}^{-1}$ are observed for GaSb, and a TO mode at $\sim 217.4\text{cm}^{-1}$ is observed for InAs. The GaSb RC is again much larger than InAs ($\sim 14:1$). This fact, again, turns out to be a significant evidence when assigning the phonon modes.

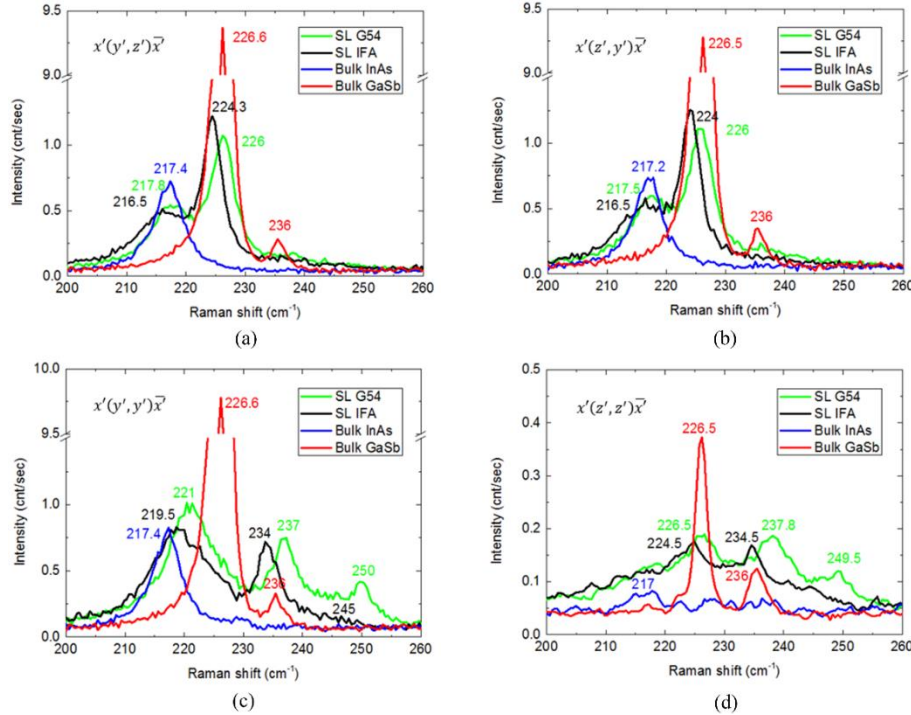


Figure 3.10: Comparing (110) back-scattering Raman spectra for the same samples as in Figure 3.8, in four polarization configurations: (a) $x'(y',z')\bar{x}$, (b) $x'(z',y')\bar{x}$, (c) $x'(y',y')\bar{x}$ and (d) $x'(z',z')\bar{x}$.

For SLs, the spectra of $x'(y',z')\bar{x}$ and $x'(z',y')\bar{x}$ are essentially the same, by comparing the corresponding spectra from panels (a) and (b): two major peaks are resolved at $\sim 226\text{cm}^{-1}$ and $217.5\sim 217.8\text{cm}^{-1}$ for the SL on InAs, and 224.3cm^{-1} and $\sim 216.5\text{cm}^{-1}$ for the SL on GaSb. The Raman selection rules indicate that these modes should have $B_2(y')$ symmetry. The lower frequency mode can be assigned as an InAs QC-TO mode based on its frequency in the SL sample on InAs substrate, as well as its intensity being lower than

the bulk InAs. The higher frequency mode should be assigned as an EX-TO mode rather than an expected GaSb C-TO [46,47], based on two considerations: (1) its intensity is about 1/8 of the bulk GaSb, while the GaSb volume fraction in SL is about 1/3; and (2) the frequency difference for the mode resolved in the SL sample on GaSb with respect to the bulk GaSb TO mode is significantly larger than those of calculated GaSb QC or C modes [7,10]. Like the situation in the (001) incidence case, here again we observe the strain effect: for the SL on InAs, the EX-TO mode is blue-shifted (incidentally matching the TO mode of the bulk GaSb) due to the compressive strain; for the SL on GaSb, the InAs QC-TO mode is red-shifted due to the tensile strain. It is observed that the InAs QC-TO mode is less sensitive to the strain than the GaSb QC-LO mode, which is consistent with the strain effects in the bulks [128,129].

For $x'(y', y')\bar{x}'$, shown in Figure 3.10 (c), three additional peaks are observed: 221cm^{-1} , 237cm^{-1} , and 250cm^{-1} for the SL on InAs, and 219.5cm^{-1} , 234cm^{-1} , and $\sim 245\text{cm}^{-1}$ for the SL on GaSb. Again these are the same set of Raman modes, but shifted against each other due to the epitaxial strain. The Raman selection rules indicate that these modes should have $A_1(z')$ symmetry. The lowest frequency mode at 221cm^{-1} or 219.5cm^{-1} can be attributed to an EX-TO mode, with both its intensity and frequency falling between the two bulk TO modes. Because this mode is derived from the bulk TO modes, there is not an obvious A_1 LO counterpart in the (001) back-scattering measurement. In fact, it is a broad band that appears to comprise unresolved components on the high frequency side. By deconvoluting this broadened peak into two components, we get another weak peak at $\sim 227\text{cm}^{-1}$ or 224cm^{-1} , in SLs on InAs substrate and SLs on GaSb substrate, respectively. This peak is close to the B_2 symmetry EX-TO mode, which is observed in $x'(y', z')\bar{x}'$ but

forbidden in $x'(y', y')\bar{x}'$. The highest frequency mode at 250cm^{-1} or $\sim 245\text{cm}^{-1}$ is close to the predicted GaAs IF_1 -TO mode with A_1 symmetry [47]. However, the LO counterpart for this IF mode is not well resolved in the (001) back-scattering measurements for sample G54, indicating that the cleaved edge has higher sensitivity for probing the IF mode. The behavior of the middle mode is peculiar: its frequency 237cm^{-1} or 234cm^{-1} is above all the bulk TO modes, and in fact rather close to the GaSb QC-LO mode at 238.6cm^{-1} or 234.3cm^{-1} , respectively for SLs on InAs and GaSb substrate, when measured from the (001) plane; however, its intensity is much stronger than the forbidden bulk GaSb LO mode, and actually comparable to the EX-TO modes. Additionally, the strain shift of this mode is substantially larger than those TO type modes. Apparently, this mode cannot be readily assigned as any of the predicted SL modes [7-10]. It should be interpreted as a transverse counterpart of the GaSb QC-LO with A_1 symmetry split due to the phonon-polariton effect. And it is also the only mode showing observable anisotropy between x' and y' , which will be discussed later. A similar phenomenon was observed for GaAs/AlAs SL when measured from the (110) plane in a forward scattering geometry, a strong LO-like peak was observed in the $y'(x', x')y'$ configuration (which is equivalent to $x'(y', y')x'$ in this work) [130].

For $x'(z', z')\bar{x}'$, as shown in Figure 3.10 (d), two weak modes were resolved: $\sim 226.5\text{cm}^{-1}$ and $\sim 237.8\text{cm}^{-1}$ in SL on InAs; and $\sim 224.5\text{cm}^{-1}$ and $\sim 234.5\text{cm}^{-1}$ in SL on GaSb. For T_d or D_{2d} symmetry, all modes are forbidden in this configuration. However, when it comes to C_{2v} symmetry, the $A_1(z')$ mode is the only mode that allowed, due to the c component of $A_1(z')$ induced by symmetry lowering. Therefore, these modes could either arise from the anticipated weak $A_1(z')$ or be the vestiges of the EX-TO modes observed in $x'(y', z')\bar{x}'$ and $x'(y', y')\bar{x}'$.

In order to further summarize the findings from the cleaved edge and to compare these spectra with those obtained from the (001) plane, we re-draw the corresponding spectra in Figure 3.11 (a) and (b), which is intended to compare (001) and the cleaved edge spectra for the four distinct polarization configurations, respectively, for the two SL samples. By doing this, we can highlight the relative positions and intensities of different modes.

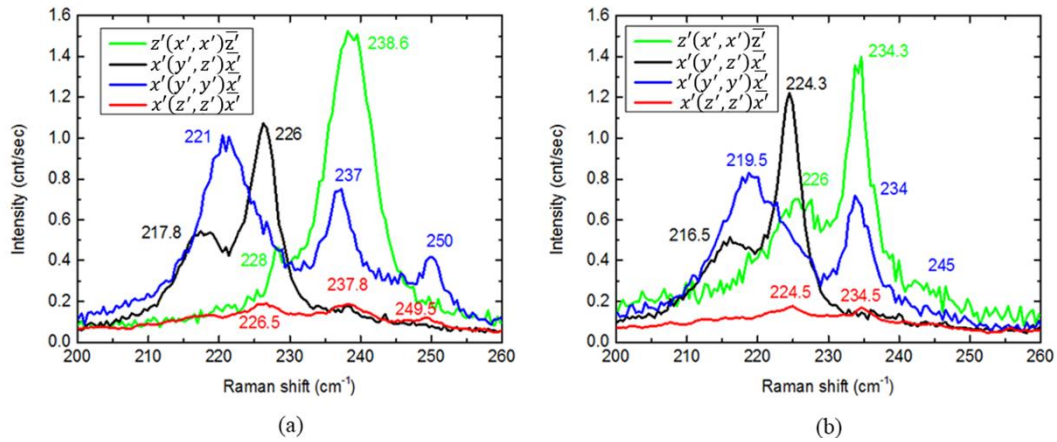


Figure 3.11: Comparison of spectra obtained in different polarization configurations, for (a) SL on InAs and (b) SL on GaSb substrate.

(2) Anisotropy between (110) and $(\bar{1}\bar{1}0)$

So far we have discussed the results from one cleaved edge, which has been assumed to be (110) plane. We now examine the possible anisotropy between $x'(y', y')x'$ and $y'(x', x')y'$, which is theoretically expected for C_{2v} [45]. By mounting two cleaved edge pieces of (110) and $(\bar{1}\bar{1}0)$ side by side and measuring them under the same conditions, we can detect anisotropy in the order of 1%.

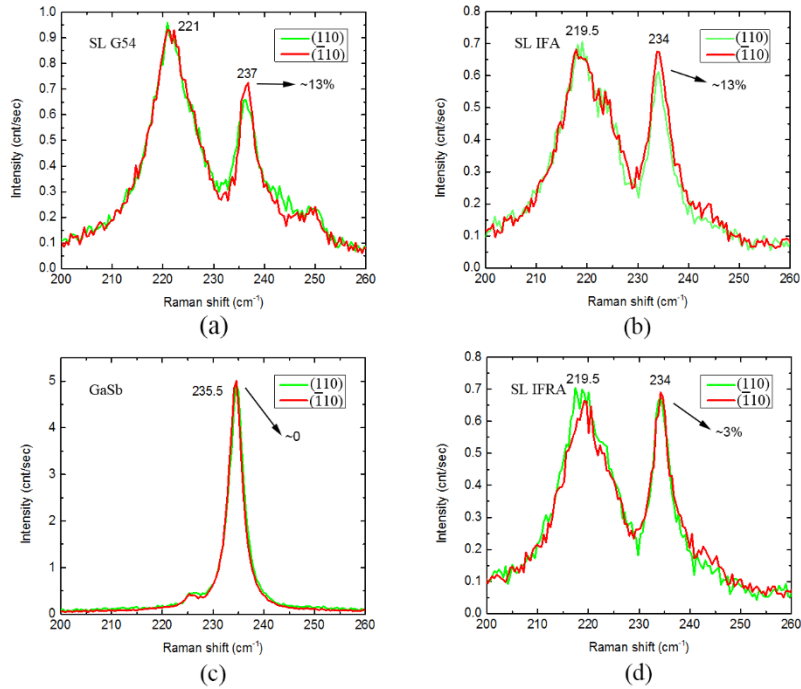


Figure 3.12: Comparison of Raman spectra measured from two cleaved edges (110) and $\bar{1}\bar{1}0$ for: (a) SL G54, (b) SL IFA, (c) thick GaSb epilayer, and (d) SL IFRA.

Similar as in the (001) plane case, we realize again, that structural treatment that have been applied to SL samples may cause a slight but non-negligible structural deviation from the C_{2v} symmetry. Thus, it is decided to firstly examine the SL samples that nominally do not have any deviation from C_{2v} symmetry, which include sample G54 and IFA. The former SL sample is a neutral-IF SL on InAs substrate, while the latter one is a neutral-IF SL on GaSb substrate. We have found only one SL Raman mode, locating at either 237cm^{-1} (G54, SL on InAs) or 234cm^{-1} (IFA, SL on GaSb), exhibits significant intensity anisotropy ~13% between (110) and $\bar{1}\bar{1}0$, as shown in Figure 3.12 (a) and (b). In contrast, on the same spectrum, the $\sim 221\text{cm}^{-1}$ (G54) or $\sim 219.5\text{cm}^{-1}$ peak (IFA), shows no apparent anisotropy. Since the observation is the same for SLs on both InAs and GaSb substrate, it

can be concluded that the anisotropy demonstrated by this 237cm^{-1} (G54) or 234cm^{-1} (IFA) mode is real.

To further confirm the reliability, the spectra of bulk GaSb are shown in panel (c), which turns out to be indeed isotropic. In addition, the anisotropy in SL alters when the rigid C_{2v} symmetry is destroyed, which could be referred to the spectra of IFRA in panel (d). SL IFRA is a GaSb-substrate-SL sample with only InSb IFs, in which a modified interface (thin InSb IF other than neutral IF) is enforced. When compared to IFA, a substantially reduced anisotropy is exhibited in IFRA, $\sim 3\%$. Therefore, we may conclude that the effect of symmetry reduction from D_{2d} to C_{2v} is minimal for most situations, nevertheless, it is still observable for certain modes. This anisotropy is another indication of the phonon-polariton nature of this mode that alters the basic Raman selection rules.

3.5 High Power Effects

In previous section, we discuss the phonon mode assignments based on Raman measurements with D2 laser power, in which case the laser power is $\sim 0.3\text{mW}$ when incident on the sample. On the other hand, we have also used D1 laser (the laser power $\sim 3.4\text{mW}$) to excite the SLs, thus got an opportunity to compare the spectra obtained by using D1 and D2 laser powers, respectively.

In Figure 3.13 (shown on next page), we show the comparison between D1 spectra and D2 spectra obtained in polarization configuration $x'(y', y')\bar{x}'$, for the same four samples as shown in Figure 3.10, from the (110) plane. Note that for each sample, the mode intensity in D2 spectra has been enlarged, to make the comparison clearer.

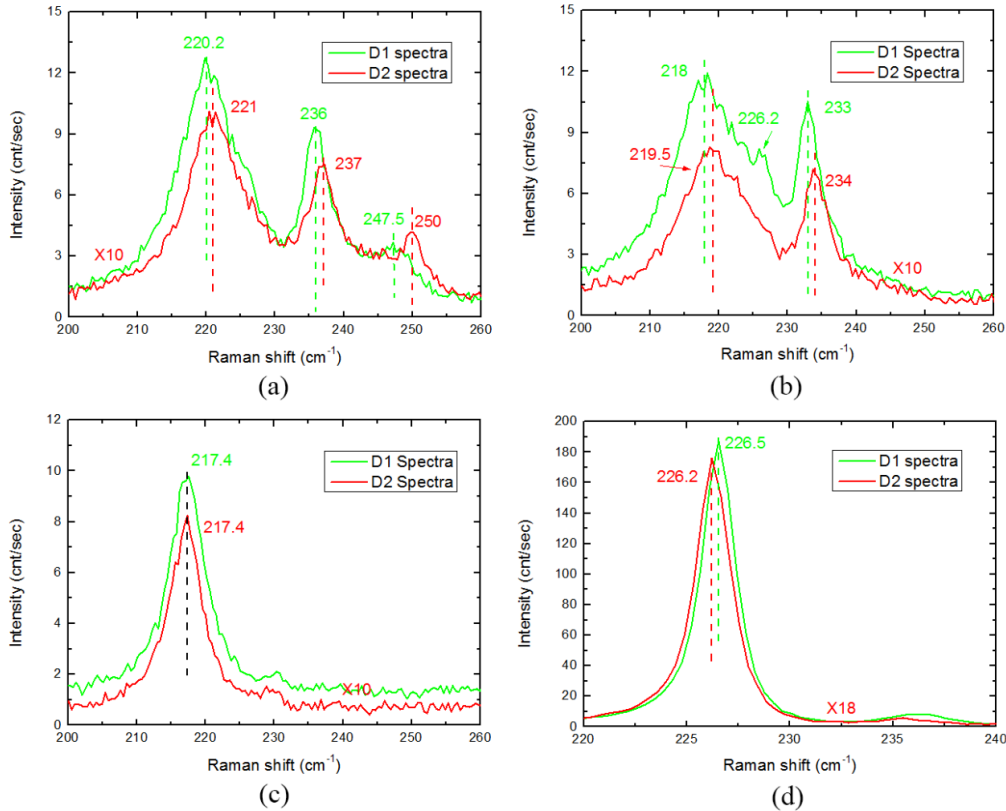


Figure 3.13: Comparing $x'(y', y')\bar{x}'$ spectra by D1 and D2 laser excitation, for (a) SL G54, (b) SL IFA, (c) InAs bulk, and (d) GaSb bulk.

Obviously, in SL samples, we observe redshifts in Raman frequencies in D1 spectra when compared to D2, while the amount of shift varies from mode to mode. For instance, in SL G54, the EX mode at $\sim 221\text{cm}^{-1}$ in D2 is shifted to $\sim 220.2\text{cm}^{-1}$ in D1 spectra, resulting in a wavenumber difference $\sim 0.8\text{cm}^{-1}$. A larger redshift is observed for the IF mode: from $\sim 250\text{cm}^{-1}$ in D2 to $\sim 247.5\text{cm}^{-1}$ in D1, thus resulting in a redshift of $\sim 2.5\text{cm}^{-1}$. In another SL sample, IFA, we make similar observations.

On the other hand, from panel (c) and (d), it is clear that for the two bulk samples, the mode frequency shift is not obvious. In InAs, the InAs TO mode at $\sim 217.4\text{cm}^{-1}$ shows no shift between D1 and D2 case. In GaSb, the GaSb TO mode is blue shifted slightly in

D1 spectra, with a difference $\sim 0.3\text{cm}^{-1}$. This shift is much smaller than those observed in the SL samples and comparable to experimental uncertainties.

We conclude that, in SL samples, laser heating usually leads to a clear red shift in phonon frequency, and the magnitude of shift varies from mode to mode. In the bulk materials, on the other hand, the frequency shift due to laser heating is much less obvious, or not observable. This different influence of laser heating on SL samples and the constituent bulks is likely be due to the thermal conductivity difference between the SL and bulk materials, and lower thermal conductivity is expected for the SLs. This difference also indicates the importance of using sufficiently low laser power (in our case, D2 laser) to study the phonon modes of these SL samples. On the other hand, if high power laser is used, for instance, D1 laser is used, the red shift in phonon modes resolved in SL samples would provide misleading information for phonon modes assignments.

3.6 Conclusions

In summary, we have concluded that the previously reported Raman mode observed in the (001) back-scattering is a GaSb QC-LO mode with A_1 symmetry. No obvious anisotropy between the $[110]$ and $[\bar{1}\bar{1}0]$ is observed, when examined from the (001) plane.

From the (110) or $(\bar{1}\bar{1}0)$ cleaved edge, we have observed at least five new Raman modes: one EX-TO and one InAs QC-TO mode, with B_2 or B_1 symmetry; one EX-TO, one IF_1 -TO, and a phonon-polariton TO mode associated with the GaSb QC-LO mode, all with A_1 symmetry. The phonon-polariton mode is observed to show apparent anisotropy between the (110) or $(\bar{1}\bar{1}0)$ plane, which is expected for a structure with C_{2v} biaxial symmetry. All the other modes, on the other hand, behave as though having D_{2d} uniaxial

symmetry. In addition, no predicted confined mode has been observed, suggesting the need for an improved lattice dynamics theory.

Overall, we have present a comprehensive examination of all four types of phonon modes in InAs/GaSb T2SL. The observation of a set of SL phonon modes from the cleaved edge indicates a very good correlation between the theoretical expectations and experimental findings, which also suggests a systematic method of using micro-Raman to study the lattice dynamics of T2SL and related materials. These findings regarding lattice vibrations will provide valuable information for the fundamental understanding the material properties: for instance, the derived information about the electron-phonon coupling will be critical to assess the lately proposed quantum transport applications that are ultimately determined by the electron-phonon interaction [131,132].

CHAPTER 4: RAMAN STUDY ON LATTICE VIBRATION MODES IN InAs/InAsSb T2SLS

4.1 Overview

As shown in Chapter 3, polarized micro-Raman spectroscopy aided with Raman selection rules is a very effective way to investigate the lattice vibration modes in InAs/GaSb T2SLS. As a further exploration, we use generally the same method to study the lattice vibration modes in InAs/InAsSb T2SLS: performing micro-Raman study on the SLs from both the (001) growth plane and (110) or ($\bar{1}10$) cleaved edges, in back-scattering geometry. The measurements were conducted at room temperature, with D2 level 532nm laser used as the excitation source. Under the same condition, Raman measurements on related materials, such as the InAs bulk and the InAsSb alloy sample, are also conducted for comparison purpose. The examined SL samples are different in SL period, such as the thicknesses of individual constituent layers. Also, Ga doping have been applied to some of the SL samples, intended to explore any new features resulted from it.

4.2 General Observations and Comments

Before going into the details of phonon modes assignments, we firstly summarize some general observations and comments in this section, which serves as a preparation for the next section.

- (1) General comments on alloy and SL Raman spectra from (001) back-scattering geometry

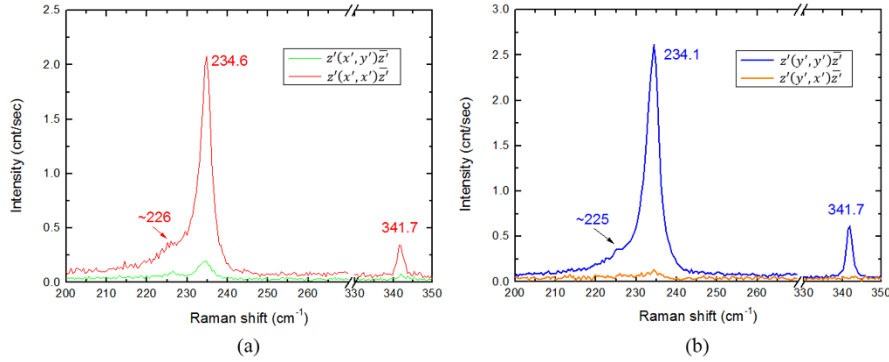


Figure 4.1: Comparing (001) back-scattering Raman spectra of InAsSb alloy (B1784), under four polarization configurations: (a) $z'(x', x')\bar{z}'$ and $z'(x', y')\bar{z}'$, and (b) $z'(y', y')\bar{z}'$ and $z'(y', x')\bar{z}'$.

Figure 4.1 shows a typical set of Raman spectra of an alloy sample (B1784) obtained from (001) back-scattering geometry, under four polarization configurations: $z'(x', x')\bar{z}'$, $z'(x', y')\bar{z}'$, $z'(y', x')\bar{z}'$ and $z'(y', y')\bar{z}'$. For InAsSb alloys, we approximate the symmetry to be T_d , and have observed very good correlation between the spectra results and the Raman selection rules. In the spectra, two modes resulting from the alloy layers are resolved, locating at $234.1\sim 234.6\text{cm}^{-1}$ and $225\sim 226\text{cm}^{-1}$, with peak intensities being much stronger in the parallel polarization configurations than the cross ones. In the selection rules for T_d symmetry, only LO modes are allowed, in $z'(x', x')\bar{z}'$ and $z'(y', y')\bar{z}'$, with the same RC proportionalities $\sim d_{\text{LO}}^2$. Thus, the modes resolved at $\sim 234.6\text{cm}^{-1}$ in $z'(x', x')\bar{z}'$ and 234.1cm^{-1} in $z'(y', y')\bar{z}'$ are the same LO mode. Also, an anisotropy is observed between the two directions x' and y' , which is unexpected for the T_d symmetry or a truly random alloy. In addition, a mode $\sim 341.7\text{cm}^{-1}$ is also resolved in the two parallel polarization configurations, which is reasonably assigned to be the AlSb LO mode [133], due to the AlSb capping layer in the sample.

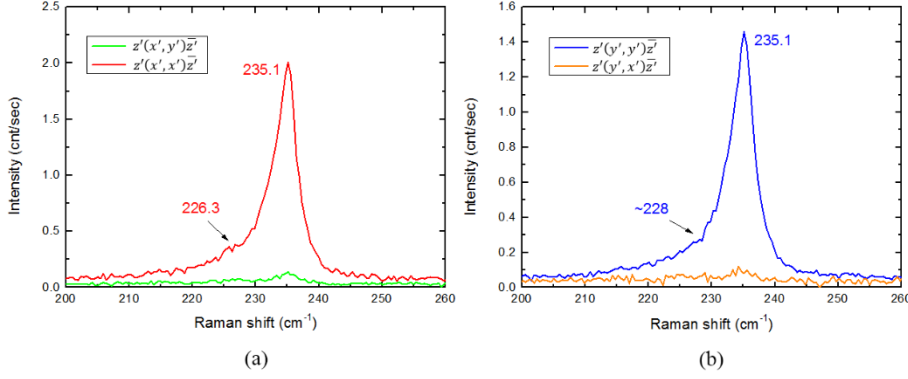


Figure 4.2: Comparing (001) back-scattering Raman spectra of InAs/InAsSb SL (B1871), under the same condition as in Figure 4.1.

Figure 4.2 shows a typical set of Raman spectra of an SL sample (B1871) obtained under the same condition as in Figure 4.1. In each of the polarization configuration, two phonon modes resulting from the SL layers are observed: a major mode resolved around $\sim 235.1 \text{ cm}^{-1}$ and a weaker mode at around $226\sim 228 \text{ cm}^{-1}$, respectively. Apparently, the intensities of two phonon modes are much larger in the parallel configurations, which become very weak in the cross ones: take the major mode as an example, it shows an intensity larger than ~ 1.4 cps in the parallel configurations, which decreases to less than 0.15 cps in the cross configurations. Besides, the spectra of $z'(x', x')\bar{z}'$ and $z'(y', y')\bar{z}'$ are generally very similar, and so are the spectra of $z'(x', y')\bar{z}'$ and $z'(y', x')\bar{z}'$. These similarities can be observed by comparing the corresponding spectra from panel (a) and (b) in the figure. Similar as in the alloy case, an anisotropy between x' and y' is also observed, which will be discussed in the next section.

Recall the selection rules shown in Table 1.3 in Chapter 1, for D_{2d} symmetry, TO modes are always forbidden, while LO modes are only allowed in the two parallel-polarization configurations. With the observations mentioned in last paragraph, in both configurations, the major mode $\sim 235.1 \text{ cm}^{-1}$ should be a LO mode with $B_2(z)$ symmetry.

Again, for D_{2d} symmetry, the RCs are expected to be the same in the two parallel configurations, $z'(x', x')\bar{z}'$ and $z'(y', y')\bar{z}'$, with the same proportionality of d_{LO}^2 . However, in the spectra shown in Figure 4.2, there is an obvious difference in intensity between the two configurations for the $\sim 235.1\text{cm}^{-1}$ mode. This finding is unexpected, and we will discuss the anisotropy between the two directions x' and y' in the following sections. At this step, we need to note that even though the InAs/GaSb SL is expected to have a lower symmetry, the anisotropy was found to be actually very weak and only observable for one mode (see Figure 3.12 (a) and (b)).

On the other hand, the non-zero intensities for the LO modes in the two cross polarization configurations could be mainly due to three facts: (1) The actual incidence direction of excitation laser may be slightly deviated from the desired z' direction. (2) There are disorders introduced to the SL sample during growth. (3) There is a deviation of the actual SL symmetry from the ideal D_{2d} symmetry.

Overall, the observations and comments above generally hold true for all the SL samples that have been examined. That is, (1) these two modes are always resolved in all of the SL samples, although there may be some frequency shifts; and (2) the mode intensities are much larger in the two parallel polarizations than the two cross ones.

(2) General consideration on SL spectra from (110) or $(\bar{1}\bar{1}0)$ backscattering geometry

As indicated in Chapter 3, the Raman measurements can always extract the signals from the SL without any ambiguity, when the thickness of the SL region is sufficiently large, for instance, $\sim 1\mu\text{m}$. On the other hand, if the SL layer is $< 1\mu\text{m}$, we may expect a portion of the collected signals to be from the substrate layer. The situation is getting worse

when the thickness of the SL layers goes down to $\sim 0.3\text{--}0.5\mu\text{m}$ (for sample G89 and G87), in which the influence of the substrate Raman signals could not be avoided.

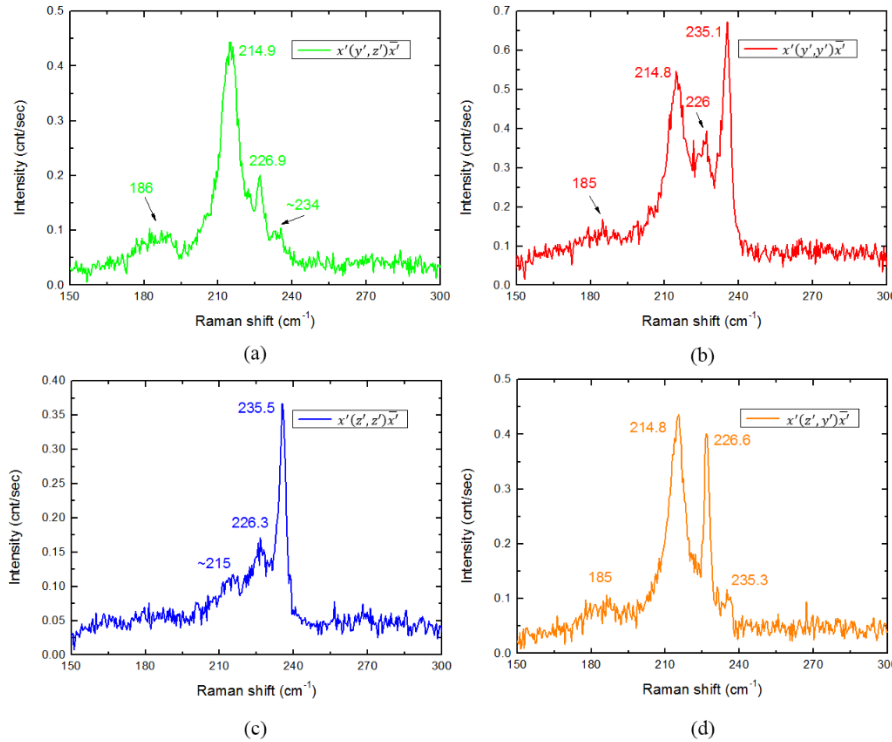


Figure 4.3: Comparing (110) back-scattering Raman spectra of InAs/InAsSb SL (B1871), in polarization configurations: (a) $x'(y',z')\bar{x}'$, (b) $x'(y',y')\bar{x}'$, (c) $x'(z',z')\bar{x}'$, and (d) $x'(z',y')\bar{x}'$.

In Figure 4.3, we present a set of Raman spectra of the SL sample B1871 (the same one as shown in Figure 4.2), obtained under (110) back-scattering geometry. We need to recall that according to Raman selection rules, only TO modes are allowed in this case, while the mode intensity will depend on the corresponding polarization configuration. Thus, it is reasonable to deduct that all the modes resolved in the spectra with considerable intensities, to be TO modes.

In the two cross polarization configurations $x'(y', z')\bar{x}'$ and $x'(z', y')\bar{x}'$, two modes are resolved, locating at $214.8\sim 214.9\text{cm}^{-1}$ and $226.6\sim 226.9\text{cm}^{-1}$. Also, it is found that, despite some peak intensity differences, the two spectra are generally similar to each other. This can be explained by the Raman selection rules, which indicate that the RCs under these two polarization configurations are both proportional to e^2_{TO} .

In the two parallel polarization configurations $x'(y', y')\bar{x}'$ and $x'(z', z')\bar{x}'$, except the two modes mentioned in the paragraph above, a new mode is resolved at $235.1\sim 235.5\text{cm}^{-1}$. According to the selection rules of D_{2d} , the RC is $\sim d^2_{\text{TO}}$ for $x'(y', y')\bar{x}'$, which is decreased to zero for $x'(z', z')\bar{x}'$. Correspondingly, in spectra, we can see that the peak intensities are weaker in $x'(z', z')\bar{x}'$ than in $x'(y', y')\bar{x}'$. However, the intensity decrease in the forbidden configuration is not as much as expected, which is attributed to the deviation of the actual SL symmetry from the ideal D_{2d} symmetry. Most significantly, a fairly strong Raman mode at 235.1 cm^{-1} appears at nearly the same frequency as the LO mode observed in the (001) backscattering geometry. In this geometry, the D_{2d} Raman selection rules suggest that the $B_2(z)$ LO mode (i.e., with \mathbf{k} in the z' direction) is forbidden, because it cannot satisfy the \mathbf{k} conservation in the (110) backscattering geometry. This consideration is valid for a uniform crystal. However, for a superlattice, quantized or standing-wave phonon modes with $|k_z| = m\pi/d$ (m stands for integer, d is the corresponding layer thickness) have net $k_z = 0$ and small $k_{[110]}$, thus can induce the scattering, which explains the appearance of the LO mode in the (110) backscattering [134]. This mode has a LO frequency even though it is strictly speaking a TO mode of the SL. Again, the qualitative comments and observations mentioned above apply to all the SL samples.

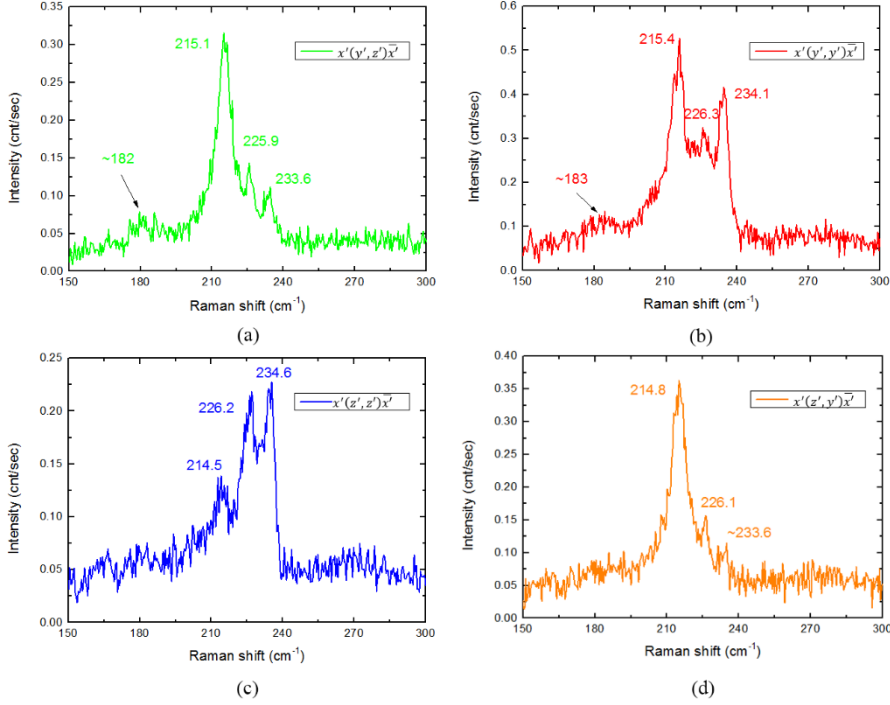


Figure 4.4: Comparing (110) back-scattering Raman spectra of InAs/InAsSb alloy (B1784), in configurations: (a) $x'(y', z')\bar{x}'$, (b) $x'(y', y')\bar{x}'$, (c) $x'(z', z')\bar{x}'$ and (d) $x'(z', y')\bar{x}'$.

In Figure 4.4, we show the set of spectra obtained from the alloy sample B1784 (same as in Figure 4.1), under the same conditions as in Figure 4.3. Under this scattering geometry, for T_d symmetry, only TO modes are allowed. The RC is the same, $\sim d^2_{TO}$, in the three polarization configurations $x'(y', y')\bar{x}'$, $x'(y', z')\bar{x}'$ and $x'(z', y')\bar{x}'$. On the other hand, it goes to zero in $x'(z', z')\bar{x}'$. In these spectra, three modes are resolved, locating at $\sim 215\text{cm}^{-1}$, $\sim 226\text{cm}^{-1}$, and $\sim 234\text{cm}^{-1}$, respectively. Moreover, the peak intensities of each mode are generally in the similar level in the three Raman allowed configurations, which decreases in the forbidden one. Thus, these modes with considerable intensity are generally to be assigned as TO modes. However, it should be noted that, similar as in the SL case, the peak intensity difference is not as big as what the selection rules indicate between the allowed and forbidden configurations. Again, in the two parallel configurations, the

forbidden LO mode at $\sim 234 \text{ cm}^{-1}$ is observed, similar as in the SL's case. Although this is not a SL structure, disordering induced by alloying could lead to scattering and mixing of different k_z modes, which could give rise to the similar effect in the SL, although to a smaller magnitude, as shown in Figure. 4.4 (b) where the LO mode remains weaker than the TO mode, in contrast to the case of the SL, as shown in Figure. 4.3 (b), where the forbidden LO mode becomes stronger than the allowed TO mode.

(3) Comparing the SLs grown on same substrates

Similar as in Chapter 3, we have used one SL sample, grown by either MBE or MOCVD technique, when making assignments for the resolved phonon modes. This method is confirmed since we observe a general similarity among the spectra of different samples, in the same polarization configuration. As a confirmation, in Figure 4.5 (shown on next page), the Raman spectra corresponding to sample B1854, B1775, B1816, and B1871 are compared, in polarization configuration $x'(y', z')\bar{x}'$. Despite some differences in mode frequency and peak intensity, the four spectral profiles are very similar to each other. Note that the frequency difference for the mode locating in the range of $\sim 214.9 \sim 216.4 \text{ cm}^{-1}$ is $\sim 1.5 \text{ cm}^{-1}$. This difference, which may provide significant information regarding the structural difference in the samples, will not affect the mode assignments.

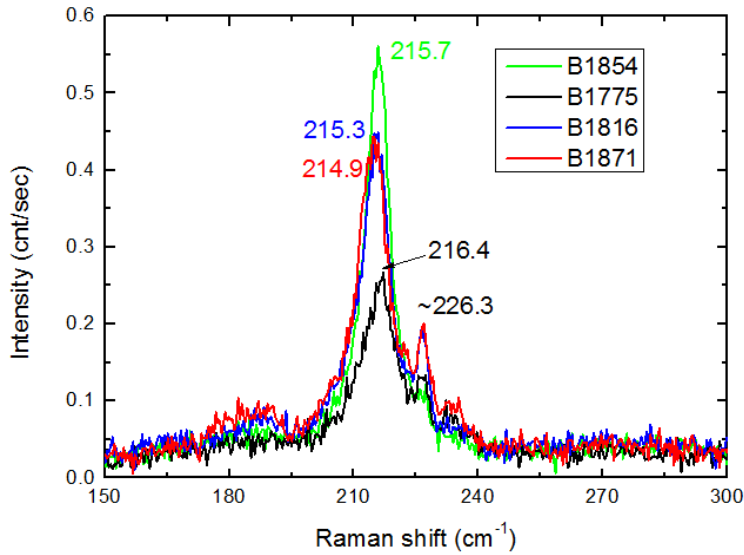


Figure 4.5: Comparison on Raman spectra for MBE InAs/InAsSb SL samples B1854, B1775, B1816, and B1871, in polarization configuration $x'(y', z')\bar{x}'$.

Overall, the similarity among the spectra of SL samples under the same condition is observed for both (001) and (110) back-scattering geometries, in every polarization configuration. Thus, we are ensured that it is sufficient to pick one MBE SL sample and one MOCVD sample when assigning the observed Raman modes.

4.3 Micro-Raman Investigation on Lattice Vibration Modes in InAs/InAsSb T2SLs

Below we discuss the Raman mode assignments by applying polarization analyses and comparing the SL spectra with those of related materials. It should be noted that, for these InAs/InAsSb T2SLs, InAs bulk and InAsSb alloy are the SL' constituents, thus it is necessary to include both the bulk and alloy in the comparison. Based on the remarks given in section 4.2, we choose one MBE SL sample and one MOCVD SL sample, and compare their spectra with those of InAs bulk and InAsSb alloy samples.

4.3.1 (001) Back-scattering

(1) Lattice vibrations and phonon mode assignments in Ga Free samples

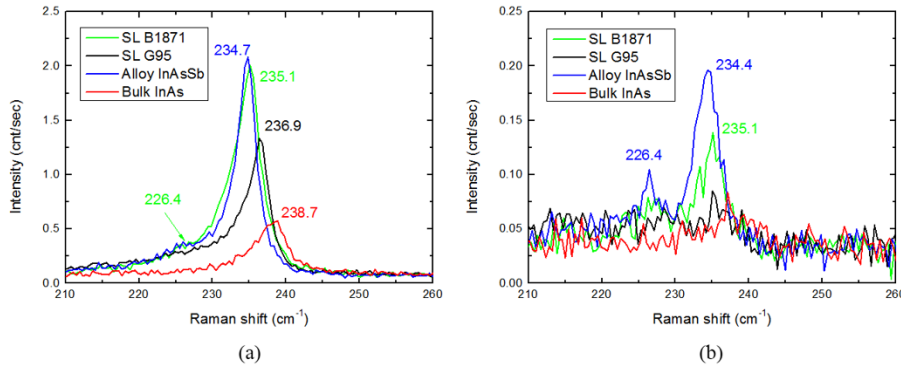


Figure 4.6: (001) back-scattering Raman spectra of InAs/InAsSb SLs, compared with those of InAs bulk and InAsSb alloys in two polarization configurations: (a) $z'(x', x')\bar{z}'$ and (b) $z'(x', y')\bar{z}'$.

For the sake of brevity and clarity in presenting the data, only the spectra of four samples, SL B1871 (MBE T2SL on GaSb substrate), SL G95 (MOCVD T2SL on GaSb substrate), alloy B1784 (MBE InAsSb alloy on GaSb substrate) and InAs bulk, are shown in Figure 4.6, which compares Raman spectra obtained in two polarization configurations $z'(x', x')\bar{z}'$ and $z'(x', y')\bar{z}'$. These samples have been carefully chosen to make the comparison, since they all have a similar epilayer thickness of $\sim 1 \mu\text{m}$, thus making it applicable to compare the mode intensity when necessary. In addition, the two SLs are sharing three general similarities: (1) similarity in SL period: the thickness ratios between the InAs and InAsSb layers are very close; (2) similarity in Sb composition: $x = 0.239$ for B1871 and $x = 0.237$ for G95; and (3) No intentional Ga doping, which is also the case for the alloy sample B1784. Since all the four samples are Ga free, we only include the spectra of bulk InAs for comparison here.

For the SL samples, in $z'(x', x')\bar{z}'$, a primary SL peak is found at $\sim 235.1 \text{ cm}^{-1}$ with an intensity ~ 2.0 cps in the MBE SL sample, or $\sim 236.9 \text{ cm}^{-1}$ with an intensity ~ 1.33 cps in the MOCVD SL sample, respectively. As discussed in the previous section, this primary

SL mode should be a LO mode, with the symmetry of $B_2(z)$. In contrast, the InAsSb LO mode is resolved at 234.7cm^{-1} with an intensity ~ 2.1 cps, and the InAs LO mode is resolved at $\sim 238.7\text{cm}^{-1}$ with an intensity ~ 0.59 cps, respectively, in the alloy and bulk sample. We noticed that the SL LO mode is red-shifted as compared to the bulk, with mode intensity considerably enhanced. This observation also holds for the InAsSb LO mode. The smaller wavenumber in the SL LO mode is expected, since Sb is added into InAs to form an alloy. However, we cannot consider these modes as same as the InAsSb LO mode resolved in InAsSb alloys. In fact, despite that the Sb compositions ($x_{\text{Sb}} \approx 0.24$) of the two SLs are higher than that of the alloy sample ($x_{\text{Sb}} \approx 0.09$), their Raman frequencies are higher than that of the alloy. According to a previous report [75], the frequency of this alloy mode has shown a linear dependence on the Sb composition x_{Sb} , which has been fitted well by the equation $\nu_{L1} = 238 - 32x_{\text{Sb}}$ ($0 \leq x_{\text{Sb}} \leq 1$). By using 238.7cm^{-1} instead of 238cm^{-1} in the equation, for $x_{\text{Sb}} \approx 0.24$ (for the two SLs), the expected InAsSb alloy mode should be located around 231cm^{-1} . Clearly, the observed SL modes are substantially different from this alloy mode.

If taking into account the fact that the InAsSb layer in the SL is under slight compressive strain, the InAsSb-like mode will be slightly blue-shifted, compared to that of a free-standing InAsSb. Similar effects have been observed in $\text{Ge}_x\text{Si}_{1-x}/\text{Si}$ SL on Si substrate, where the strain caused a blue shift in the $\text{Ge}_x\text{Si}_{1-x}$ like mode resolved in SLs [135]. For the alloy sample, the expected LO phonon frequency will be 235.8cm^{-1} , which is in reasonable agreement with the measured value of 234.7cm^{-1} . Note that this alloy sample was intended to be lattice-matched with the GaSb substrate, but might not be

perfectly matched. Thus, it could be expected that the strain in the alloy is smaller than that in the SL samples.

Generally, the above observation holds for all the SL and alloy samples that have been examined. That is, the LO mode resolved in SL usually has a larger frequency than the alloy LO mode. The comparison is summarized in Figure 4.7, which plots the frequency of the LO mode vs. Sb composition x_{sb} for all the SL and alloy samples. The dotted linear line shows the fitting result in the literature [75], by using our value 238.7cm^{-1} instead of 238cm^{-1} in the original equation $\nu_{L1} = 238 - 32x_{sb}$ ($0 \leq x_{sb} \leq 1$).

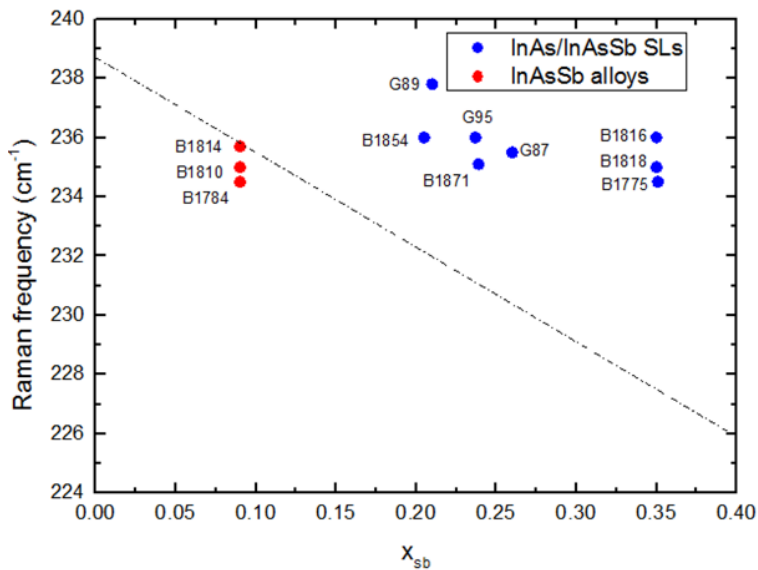


Figure 4.7: Frequency for the LO mode resolved in InAs/InAsSb SL and InAsSb alloy samples, in (001) back-scattering geometry.

Here, we will refer to the LO phone mode resolved in the SL as a SL LO mode. We can summarize three interesting properties of this SL mode and make some comments: (1) in this scattering geometry, this mode follows the similar selection rules as the LO mode in InAs and InAsSb alloy, although the frequency is significantly higher than that expected

in the alloy with the same composition. (2) The SL mode intensity is considerably enhanced as compared to that of InAs bulk. Considering that these samples have the similar thicknesses, the enhancement is likely to be related to higher RC of InSb, which remains to be verified after we can acquire an InSb reference sample. Additionally, although the two SL samples are supposed to have very similar structures, their Raman frequencies differ by nearly 2cm^{-1} . More accurate structural analyses are required to further address the difference. However, this is beyond the scope of this work.

In addition to the major SL mode, a shoulder at $\sim 226\text{cm}^{-1}$ is also resolved in the SL samples, as well as in the alloy sample. This mode is not clearly resolved, and the intensity is generally very low. Thus, it is attributed to the disorder-activated optical (DAO) phonon mode, which has been previously found in the alloys [75].

In contrast to the clearly observed SL mode, the InSb like LO mode, which has been observed in the InAsSb alloys mentioned in literature [75], is not resolved in our cases, for both SL sample and alloy samples. This could be possibly attributed to the relatively small Sb composition, as well as the relatively low excitation laser power. Especially, for the alloy sample, the Sb composition is very low, $x_{sb} \sim 0.09$.

(2) An additional phonon mode due to Ga doping

In general, all the SL samples are sharing similar spectra profiles, no matter whether Ga is intentionally doped or not. However, it is also found that specific Ga doping may lead to a new phonon mode in the SL. In Figure 4.8 (shown on next page), we compare the Raman spectra under two polarization configurations $z'(x', x')\bar{z}'$ and $z'(x', y')\bar{z}'$. To make the comparison clearer, we only include three SL samples, B1775 (MBE T2SL on GaSb substrate, no Ga doping applied), B1816 (MBE T2SL on GaSb substrate, Ga doped at the

center of the InAsSb layer in each SL period) and B1818 (MBE T2SL on GaSb substrate with delta Ga doping applied: Ga is doped at the interface of the InAs and InAsSb layer of the SL). Note that the Sb composition x_{sb} for the three samples are nearly the same, ~ 0.35 .

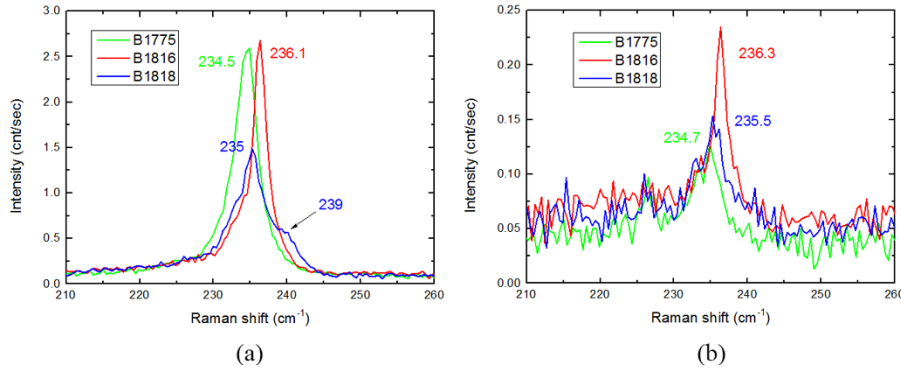


Figure 4.8: Comparing (001) back-scattering Raman spectra of InAs/InAsSb SLs, among sample B1775, B1816 and B1818 in polarization configurations: (a) $z'(x', x')\bar{z}'$ and (b) $z'(x', y')\bar{z}'$.

Despite the frequency differences in the SL LO mode, the most obvious difference among the samples is that there is a phonon mode resolved $\sim 239\text{cm}^{-1}$ in B1818, which is not resolved in the other two SL samples. It should be noted that although Figure 4.8 only show three SL samples, the observation comment holds for all the SL samples, as well as the InAsSb alloy samples. In other words, this mode is solely resolved in SL sample B1818. Since the intensity of this mode is much larger in $z'(x', x')\bar{z}'$ than $z'(x', y')\bar{z}'$, it is also a LO mode. Interestingly, under the same experimental condition, this mode has a frequency and peak intensity very close to that of InAs bulk (238.7cm^{-1}), since intensity for both the two peaks are $\sim 0.5\text{cps}$. We note that the Sb composition of the corresponding sample (B1818) is $x_{sb}=0.35$, which should lead to an InAsSb mode with a wavenumber around $\sim 227.5\text{cm}^{-1}$ in the alloy according to the literature data given earlier. Thus, the possibility

of relating this mode to Sb composition can be excluded. Secondly, this mode is not directly due to the possible GaSb bonds introduced by Ga doping, since the GaSb LO mode in GaSb bulk sample is located at $\sim 236\text{cm}^{-1}$, under the same condition. At this step, we conclude that only specific Ga doping results in this mode, since in SL sample B1816, which is only different from B1818 by the Ga doping treatment, this $\sim 239\text{cm}^{-1}$ mode is not resolved. Thus, although the origin of this mode is still unknown, we can correlate this mode directly to the delta Ga doping applied to the SL sample. This finding, also indicates the powerful ability of Raman spectroscopy to reveal fine structural variations in SL samples. This finding should be further confirmed in the future by investigating similar samples.

(3) Anisotropy consideration between $[110]$ and $[\bar{1}10]$ direction

As mentioned in previous discussion, an anisotropy is not expected in the SL samples between x' and y' , unless there is a significant deviation of the actual SL symmetry from D_{2d} symmetry. By using the same method as conducted in the case of InAs/GaSb T2SLs, different levels of anisotropy are observed throughout the SLs samples, as well as the alloy samples.

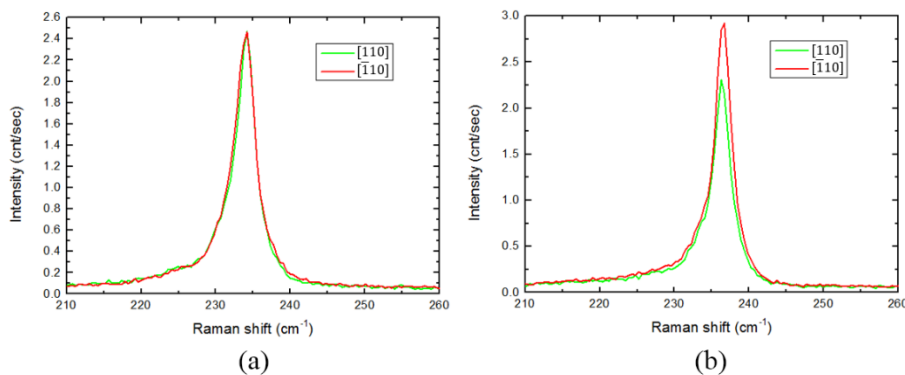


Figure 4.9: Comparing Raman spectra to explore the anisotropy between $[110]$ and $[\bar{1}10]$, for: (a) SL B1775 and (b) SL B1816.

In Figure 4.9, we show the spectra comparison between $z'(x', x')\bar{z}'$ and $z'(y', y')\bar{z}'$ to explore the anisotropy between [110] and $[\bar{1}10]$ direction, for SL sample B1775 and B1818, respectively. In B1775, it is clear that there is no obvious anisotropy between the two directions. In B1818, on the other hand, an apparent anisotropy is observed, with an intensity difference $\sim 16\%$ for the SL LO mode. Table 4.1 presents a complete list of anisotropy results for SL samples and alloy samples.

Table 4.1: Anisotropy results for InAs/InAsSb T2SL and InAsSb alloy samples.

Sample	x (Sb)	Anisotropy Ratio	Direction for stronger intensity
B1775	0.351	1.00	N/A
B1854	0.205	1.10	$[\bar{1}10]$
3-2295	0.237	1.17	[110]
3-2289	0.21	1.18	
B1871	0.239	1.20	[110]
B1818	0.35	1.26	
B1816	0.35	1.27	$[\bar{1}10]$
3-2287	0.26	1.35	
B1810	0.09	1.00	
B1784	0.09	1.24	
B1814	0.09	2.00	

4.3.2 (110) Cleaved Edge Back-scattering

(1) Lattice vibrations and phonon mode assignments for Ga free SLs

Shown in Figure 4.10 (shown on next page) are the typical spectra for the MBE and MOCVD SL samples, obtained from one of the cleaved edges; for comparison purpose, the spectra of InAsSb alloy and InAs bulk is also included. According to the Raman selection rules for D_{2d} symmetry, TO mode is allowed in the three polarization configurations $x'(y', z')\bar{x}'$, $x'(z', y')\bar{x}'$, and $x'(y', y')\bar{x}'$, but forbidden in $x'(z', z')\bar{x}'$.

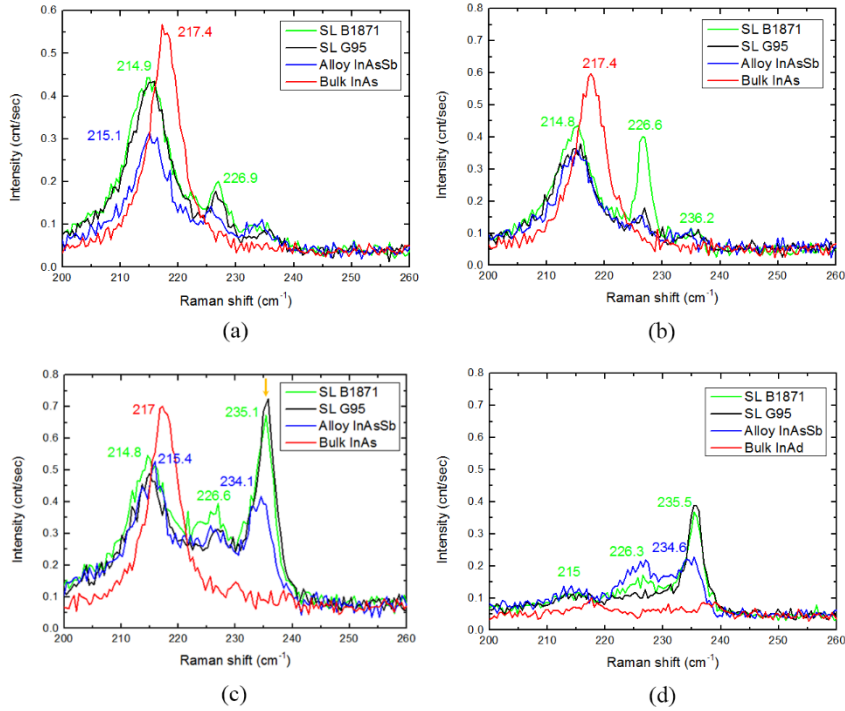


Figure 4.10: Comparing (110) back-scattering Raman spectra for the same samples as in Figure 4.6, in four polarization configurations: (a) $x'(y', z')\bar{x}$, (b) $x'(z', y')\bar{x}$, (c) $x'(y', y')\bar{x}$ and (d) $x'(z', z')\bar{x}$.

For the SLs, in total three TO modes are resolved. The first mode is resolved at $\sim 214.8\text{cm}^{-1}$ for both the MBE SL sample and the MOCVD one. In the three allowed configurations, the mode intensity is $\sim 0.35\sim 0.55$ cps, which decreases to ~ 0.15 cps in the forbidden configuration $x'(z', z')\bar{x}$. For comparison, in the alloy sample B1784, a mode is resolved at $\sim 215.1\sim 215.4\text{cm}^{-1}$, which is assigned to be the InAsSb TO mode. In the InAs bulk, an InAs TO mode $\sim 217.4\text{cm}^{-1}$ is also resolved. Generally, these three modes are behaving in a similar way, which is expected from the selection rules. When comparing the mode frequency and intensity among the SLs, alloy and bulk, under any Raman allowed configurations, it is observed that the mode in SLs and alloy is red shifted with respect to the bulk mode, and the intensity is decreased. However, it should be noted that again, the mode in SL does not behave in exactly the same way as the InAsSb TO mode in InAsSb

alloy does, since the mode resolved in SLs has a considerably larger frequency than the expected one from the literature data [75]. With $x_{sb} \approx 0.24$ for these two SLs, by using 217.4cm^{-1} instead of 219cm^{-1} in Li's formula fitting the InAsSb TO mode ($\nu_{T1} = 219 - 27x$), the expected mode is $\sim 210.9\text{cm}^{-1}$. In contrast, the actual TO mode is located at $214.8\sim 214.9\text{cm}^{-1}$ in the SL samples. On the other hand, the expected TO mode will be $\sim 215.0\text{cm}^{-1}$ for the alloy sample B1784, which is very close to the measured value of $\sim 215.1\sim 215.4\text{cm}^{-1}$.

Similar to the case from the (001) plane, we name this mode as a SL TO mode, which has been red shifted with respect to the bulk InAs TO mode due to InAs and InSb alloying, but also has a considerable larger frequency than the alloy TO mode resolved in a free-standing alloy sample. In Figure 4.11, we shows the frequency of this TO mode resolved in all the SL samples and the alloy samples. The dotted linear line shows the fitting result in literature [75], by using our value 217.4cm^{-1} instead of 219cm^{-1} in the original equation $\nu_{T1} = 219 - 27x_{sb}$.

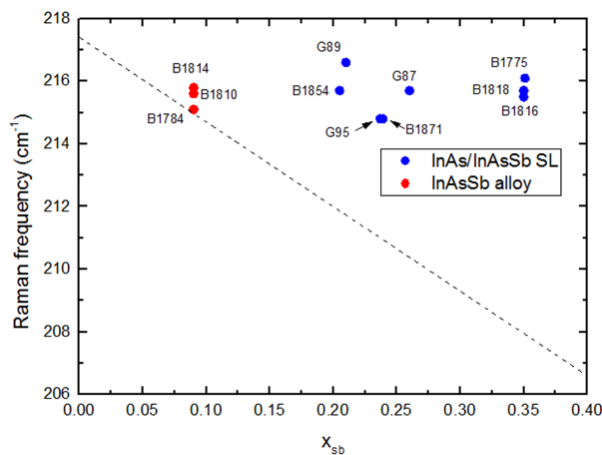


Figure 4.11: Mode frequency for the TO mode due to InAs and InSb alloying, resolved in InAs/InAsSb SL samples and InAsSb alloy samples, in (110) back-scattering geometry.

For this SL TO mode, a very interesting finding is that, the frequencies of this TO mode are very close for the two SL samples. On the other hand, there is an obvious frequency difference in the SL LO mode between the two SLs, which is resolved in (001) back-scattering measurements. This difference is possibly to be related to the different symmetries that these two modes have. That is, for the SL LO mode, its symmetry is $B_2(z)$; for the SL TO mode, its symmetry is $E(x)$ or $E(y)$.

The second mode resolved in SL samples is locating at $\sim 226.6\sim 226.9\text{cm}^{-1}$, which is always weak ($\sim 0.2\text{cps}$) and quite noisy in the three allowed polarization configurations. Note that the much larger peak intensity shown in sample B1871 in panel (b) is due to the unintentional collection of Raman signals from its GaSb substrate layers during measurements. However, the mode intensity is enhanced at the forbidden configuration, reaching nearly to $\sim 0.4\text{cps}$. Recall that a mode with similar frequency is resolved at the (001) plane, at roughly 226.4cm^{-1} , which is also not well resolved. Thus, we assign this mode resolved at the (110) plane to be the DAO phonon as well. Note that in the alloy, a mode with a similar frequency is also resolved, which is consistent with the mode assignment.

The third resolved mode is locating at $\sim 235.1\text{cm}^{-1}$ in $x'(y', y')\bar{x}'$, with an intensity of $\sim 0.7\text{cps}$. To emphasize, this mode is labeled by an orange arrow in Figure 4.10, panel (c). With a slightly different wavenumber of $\sim 235.5\text{cm}^{-1}$, this mode is also resolved in $x'(z', z')\bar{x}'$. Firstly, this mode could not be readily related to the TO mode originating from any related constituents: InAs, InAsSb alloy, or InSb (since In-Sb bonds are possible). The reasoning is obvious: InAs TO mode is located at $\sim 217\text{cm}^{-1}$, while the InSb TO mode and InAsSb TO mode in InAsSb alloy should have even smaller wavenumbers; in contract, this

mode is located at $\sim 235.1 \text{ cm}^{-1}$. On the other hand, we need to recall that a LO mode with a similar frequency is resolved at the (001) plane: for B1871, the mode is located at 235.1 cm^{-1} ; for G95, the mode is located at 236.9 cm^{-1} . The underlying mechanism has been given in section 4.2. It is interesting to note that this mode is stronger in the SL than in the alloy, the former of which has regular modulation along the z' axis; and its intensity is even stronger than the allowed TO mode, which is rather unusual. Although such mode has been reported in GaAs/AlAs SLs [130] and also observed in InAs/GaSb T2SLs as discussed in Chapter 3, they were always weaker than the TO modes. Recall that these modes are forbidden in the bulk crystal, but allowed in these artificial SL structures, due to the fact that there are regular modulations introduced along the growth direction of the SLs. These modulations make the net z-component of the wave vector going to zero but the (110) component of the wave vector to be a small value, which induces the scattering.

(2) Effect of Ga doping

In Figure 4.12 (shown on next page), we compare the (100)-plane spectra of the same three samples shown in Figure 4.10. Recall that in (001) plane Raman measurements, a LO mode due to delta Ga doping is resolved, with a frequency $\sim 239 \text{ cm}^{-1}$, which indicates that specific Ga doping treatment could result in new phonon modes. Thus, we also want to explore whether the delta Ga doping applied in B1818 could result in any new mode resolved in this scattering geometry. However, other than some small wavenumber differences in the mode resolved, there is no additional mode resolved that could be directly related to delta Ga doping, which is very different from the finding in the (001) plane.

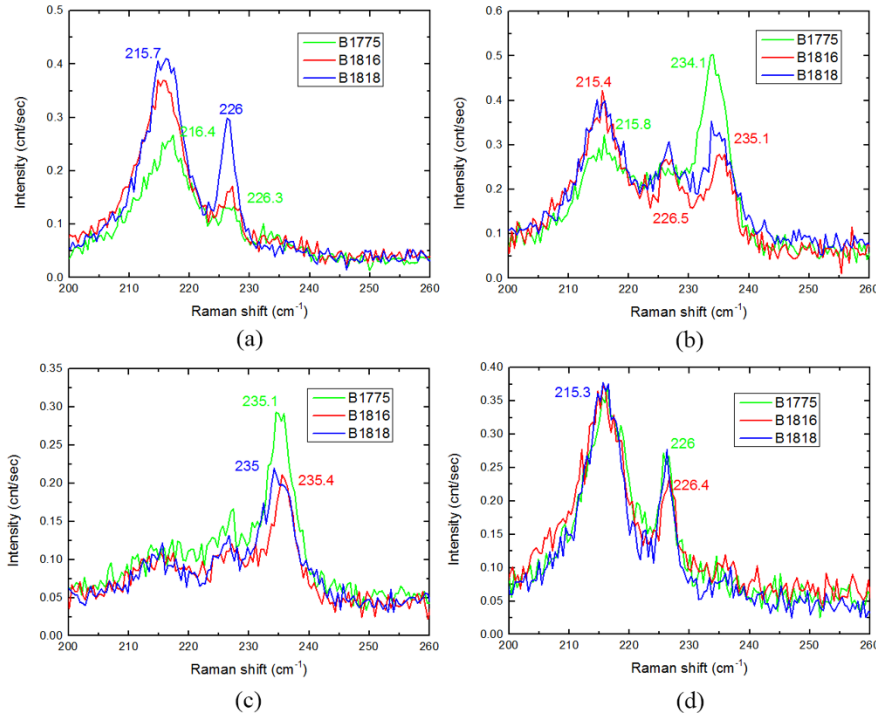


Figure 4.12: Comparing (110) back-scattering Raman spectra of InAs/InAsSb SLs, among SL samples B1775, B1816 and B1818 in polarization configurations: (a) $x'(y', z')\bar{x}'$, (b) $x'(z', y')\bar{x}'$, (c) $x'(y', y')\bar{x}'$ and (d) $x'(z', z')\bar{x}'$.

4.3.3 Comparison with InAs/GaSb T2SLs

As the two SL systems share similarities in some aspects while also possess differences in other aspects, it is interesting to make a comparison between the InAs/GaSb T2SL with InAs/ InAsSb T2SL, regarding their Raman spectra. However, since the two systems are different in several aspects, such as SL constituents, SL symmetry, whether there is a common-atom-interface or not; it is not practical to conduct comparisons regarding the exact mode frequency or intensity. Instead, we can make a general comparison regarding the spectra profiles, which is helpful in better understanding these two systems. Especially, we pay attention to the (110) plane, in which case two apparent differences are shown between the two systems. (1) In polarization configuration $x'(y', y')\bar{x}'$, there is a new mode resolved in the InAs/GaSb SL system, which could not

be related to any confined or quasi-confined TO or LO mode of the constituent. For instance, in InAs/GaSb T2SL sample IFA, the 219.5cm^{-1} mode is resolved and assigned as a SL EX mode. The mode frequency could not be related to the existing mode of any constituents. On the other hand, no such mode is resolved in the InAs/InAsSb SL system.

(2) In the InAs/GaSb SL system, the quasi-confined InAs TO mode (which is closely related to one of the SL's constituent, InAs) is only resolved in $x'(y', z')\bar{x}'$ and $x'(z', y')\bar{x}'$, which disappears in $x'(y', y')\bar{x}'$. For instance, in IFA, the InAs QC TO mode $\sim 216.5\text{cm}^{-1}$ is only resolved in $x'(y', z')\bar{x}'$ and $x'(z', y')\bar{x}'$. This finding indicates a clear difference between $x'(y', y')\bar{x}'$ and the two cross configurations, for C_{2v} symmetry. On the other hand, the SL TO mode that is closely related to InAs and InSb alloying is resolved in all the three configurations mentioned above. For instance, in InAs/InAsSb T2SL sample B1871, the 214.8cm^{-1} mode is resolved in all three configurations, with the intensities also being in similar levels. This difference between the two SL systems is possibly attributed to the difference in symmetry.

In addition to these differences, the two systems, also share some similarities. The most notable finding is the feature resolved in $x'(y', y')\bar{x}'$, which is assigned to be a transverse counterpart of the corresponding LO mode.

4.4 Conclusions

In the InAs/InAsSb T2SLs, a LO and TO mode, resulting directly from InAs and InSb alloying, are resolved from the (001) and (110) plane, respectively. These modes are named as SL LO and TO mode, respectively; and both modes are found to be red shifted with respect to the InAs bulk LO or TO mode, respectively. However, their frequencies do not match what would be expected from the respective alloy modes based on the literature

data for InAsSb alloys. Instead, the frequencies of both modes are blue shifted with respect to the alloys modes, which is partially related to the in-plane compressive strain in the InAsSb layer of the SL.

From the (110) plane, a TO mode is resolved in both SLs and InAsSb alloys, with a frequency close to the LO mode resolved from the (001) plane. This mode is assigned as a transverse counterpart of the LO mode due to phonon confinement effect in the SL and disorder scattering in the alloy. A similar phenomenon is observed in the case of InAs/GaSb T2SLs.

In addition, a comparison between the two SL systems, InAs/GaSb SL system and InAs/InAsSb SL system is conducted. An obvious difference regarding general Raman spectral profile is observed between these two SL system, which is attributed to the fact that these two systems have different symmetries, C_{2v} and D_{2d} , respectively. On the other hand, a general similarity is also observed between these two systems, that is, a transverse counterpart of the LO mode is resolved in the cleaved edge plane. This is attributed to the fact that in both systems, there is a regular modulation introduced along the SL growth direction. In order to better understand these resolved modes, more work is needed, which requires both theoretical and experimental efforts.

CHAPTER 5: PL STUDY ON EXTENDED DEFECTS IN CdTe EPILAYERS

5.1 Overview

In this chapter, confocal micro-photoluminescence (μ -PL) mapping was applied to investigate the effects of extended defects in a set of six CdTe epilayers, which had been grown on (211) Si substrates with different numbers of annealing cycle N [104]. In the obtained PL maps, usually a large number of PL dark spots were observed, and the PL dark spot density (PL-DSD) were counted. The results from PL methods are compared with those from other characterization methods, such as x-ray diffraction (XRD) linewidth and etch pit density (EPD) by chemical etching. Especially, correlation between the PL dark spots and etch pits is also conducted.

Generally, it is found that the PL-DSD decreases with an increasing number of annealing cycles, which is consistent with the general trend that increases in the number of annealing cycles lead to reduction of the X-ray diffraction (XRD) linewidth and etch pit density (EPD). The detailed discussion and comparison is presented in section 5.3.

In order to further correlated the PL dark spots and etch pits, we conducted a direct comparison between the etch pits imaged by scanning electron microscope (SEM) and PL dark spots on the same sample area, which is presented in section 5.4. This direct comparison results in two important observations: (1) the PL-DSD is substantially higher than the EPD, and (2) not all etch pits appear as dark spots in PL maps. These findings suggest that PL mapping is a more sensitive technique for revealing the extended defects

that are actually detrimental to photo-generated carriers, in addition to the apparent advantages of being non-invasive.

5.2 Experimental Procedures

The PL measurements have been conducted at room temperature, with the excitation wavelength being 532nm, resulting in a spatial resolution of $\sim 0.36 \mu\text{m}$ with the $100\times$ lens. D2 ND filter was used, and the excitation laser power was $\sim 0.3\text{mW}$.

For each of the examined sample, the mapping areas were carefully chosen so that they were free of visible surface defects. The mapping area was $20 \mu\text{m} \times 20 \mu\text{m}$, with a step size of $0.5 \mu\text{m}$. Thus, a total of $41 \times 41 = 1681$ sites on the epilayer are examined by single-window PL measurements, which is centered at 822nm with a $\sim 22\text{nm}$ bandwidth. The $\sim 822\text{nm}$ PL peak corresponds to the excitonic emission of CdTe at room temperature [136].

As mentioned in section 2.1, both XRD and chemical etching had been conducted on the same samples, in order to make a comparison with the PL data. However, because the samples used for chemical etching and PL were separated pieces of the same sample, it would not be possible to make one-to-one comparison between the defects revealed by chemical etching and PL mapping. This is a major shortcoming of the conventional research practice that we refer to as a “parallel mode”. Therefore, in order to further correlate the PL dark spots to specific structural defects, such as dislocations, we have selected the sample with annealing circle $N=8$ to perform a correlated study in a “series mode”. For this particular case, the series mode means to perform the PL and etching on the same area of one sample, and perform the non-invasive PL mapping before conducting the invasive chemical etching. After PL mapping, the sample was chemically etched using a conventional Everson etching to reveal etch pits [137]. The etch pits were observed under

the optical microscope by using the 100 \times objective lens. To observe them with better resolution, SEM was used. The accelerating voltage was 10kV, the aperture size was 30 μm , and the magnification was 2480. A laser was used to generate markers on this epilayer, so that we were able to identify the area after etching, which ensured that the subsequent comparisons between PL and SEM results were reliable.

5.3 General PL Results and Discussion

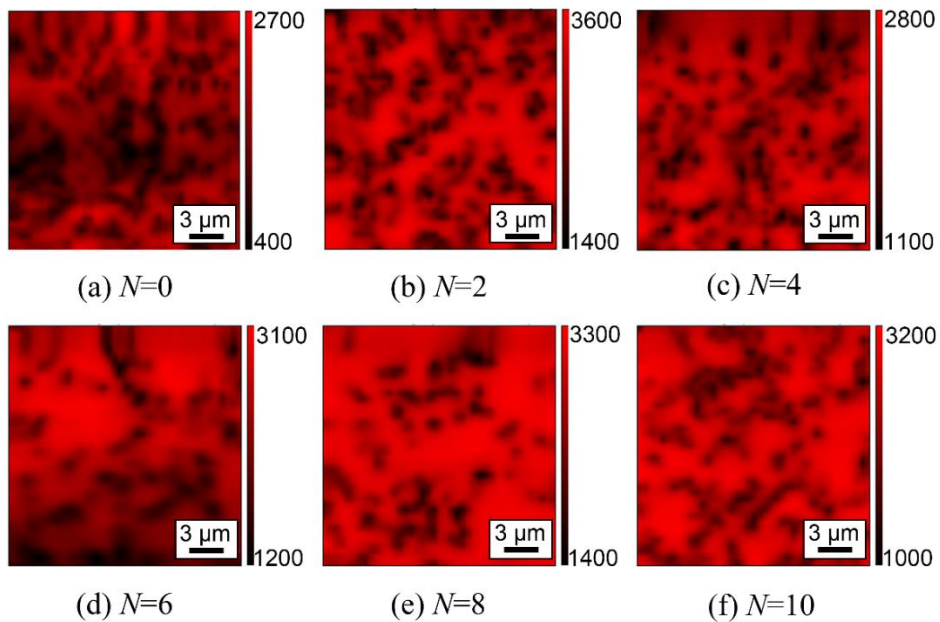


Figure 5.1: PL intensity maps of CdTe epilayers with different annealing cycles N : (a) $N=0$, (b) $N=2$, (c) $N=4$, (d) $N=6$, (e) $N=8$, and (f) $N=10$. The area is $20\ \mu\text{m} \times 20\ \mu\text{m}$.

Figure 5.1 summarizes the PL mapping data for six samples with annealing cycles of $N = 0, 2, 4, 6, 8,$ and 10 . In general, a large number of PL dark spots were resolved in each of the maps, which corresponds to sites of low PL intensities. These dark spots were likely to be associated with extended defects residing in the surface of the epilayers. However, it is also obvious that the PL-DSD varies from sample to sample. For instance,

the PL-DSD in the epilayer with $N = 0$ is apparently larger than that in the epilayer with $N = 6$. A general trend was clearly observed: the PL-DSD reduces with an increasing number of annealing cycles, although the trend is non-monotonic. This observation was generally consistent with the reduction in EPD and XRD linewidth upon increasing the number of annealing cycles [104].

Table 5.1 Summary of characterization results of CdTe epilayers grown on Si-(211) substrates.

Sample	Annealing Cycles (N)	XRD FWHM (Arcsec)	EPD (10^7cm^{-2})	PL-DSD (10^7cm^{-2})	Averaged PL Intensity (Normalized)
32207	0	110	2.7	5.6	0.527
32707	2	86	1.6	3.95	0.964
40307	4	79	0.98	3.65	0.753
32807	6	56	0.13	2.675	0.799
32607	8	61	0.077	2.325	1.000
32307	10	58	0.043	3.375	0.911

By these PL maps, we can count the PL-DSD for each epilayer. In Table 2.6, we have sample information and characterization results of XRD and chemical etching. In this chapter, we add the PL mapping results into the table, and present below as Table 5.1, which provides a clear comparison for the results obtained from PL, XRD, and chemical etching. Note that two columns of PL data are listed in the table: PL-DSD and averaged PL intensity. At this step, we only consider the column of PL-DSD. It is assumed that the PL-DSD should hold a proportionality with the extended defect density. Accordingly, it is found that the optimal annealing circle is $N_{\text{op-PL}} = 8$, which corresponds to the lowest PL-DSD. It is also shown from Table 5.1, that the optimal annealing cycle number was different in different measurements. That is, $N_{\text{op-XRD}} = 6$ for XRD method, and $N_{\text{op-EPD}} =$

10 for chemical etching method, respectively. The variation could be due to the fact that different properties were probed in these measurements, but might also be due to the inhomogeneity of the examined epilayer, because different pieces of samples were used in the three independent measurements.

Although the PL results are generally consistent with the observed trend between the EPD and annealing cycles (both EPD and PL-DSD tend to decrease with increasing N), there is a quantitative difference between these two techniques. From Table 5.1, we can see that the PL-DSD seems to be somewhat higher than the corresponding EPD of the same sample. For instance, for the epilayer with $N = 8$, the PL-DSD is ~ 20 times as large as the EPD for the $N = 8$ epilayer. This discrepancy could be due to the sensitivity difference between the two techniques, but may also be related to the fact that the EPD and PL-DSD were not measured from the exactly same area.

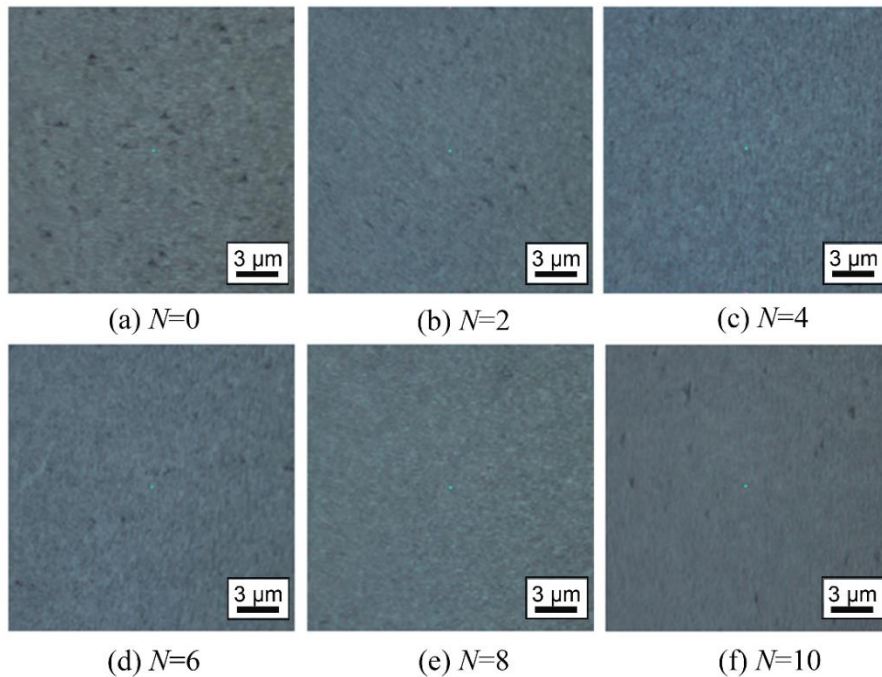


Figure 5.2: Optical image for samples with different annealing cycles N : (a) $N=0$, (b) $N=2$, (c) $N=4$, (d) $N=6$, (e) $N=8$, and (f) $N=10$.

Figure 5.2 contains representative optical images of these six samples after chemical etching, under $100\times$ objective lens. The etch pits are the triangular shaped pits in this figure. When considering the density level, there is a very good qualitative correspondence between the PL dark spots and the etch pits shown in the optical images. For instance, for the $N=0$ epilayer which has the largest PL-DSD, its EPD in the optical image is also the largest. On the other hand, for the $N=8$ epilayer has the lowest PL-DSD, the corresponding EPD is also the lowest. Besides, this epilayer also has the smoothest surface after etching. However, we could not make any direct comparisons, since the sample areas shown in Figure 5.1 did not correspond to those shown in Figure 5.2.

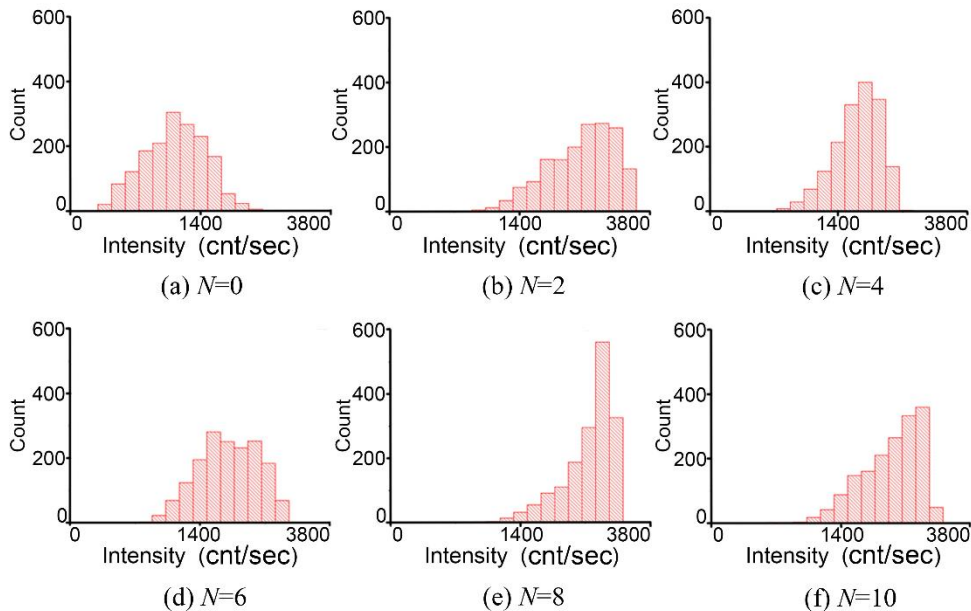


Figure 5.3: Histogram plots of the PL mapping data shown in Figure 5.1. Note that the axis ranges are the same for all plots.

To make more quantitative discussions, we generate the histogram plots of the PL mapping data in Figure 5.1, and show them in Figure 5.3. It provides clear statistical insight into the PL mapping results and useful quantitative information. For instance, we can

obtain the spatially averaged PL intensities for all the samples, which are also summarized in Table 5.1. The spatially averaged PL intensity increases with increasing the number of annealing cycles, and is maximized at $N = 8$. However, similar as the PL-DSD discussed previously, this averaged PL intensity also does not necessarily follow a simple monotonic dependence on N . Besides, it is worthwhile to note that among the six samples, the $N = 8$ epilayer not only showed the highest averaged PL intensity but also the sharpest distribution in the histogram plot. That is, there were more tested sites on the surface showing high intensity PL signals in this $N = 8$ sample than the other five. For instance, in the epilayer with $N = 0$, the PL intensities roughly follow a Lorentz profile, and its FWHM is larger than 800. On the other hand, in the epilayer with $N = 8$, the PL intensities form a profile in which the peak could not be simulated by a simple model such as Gaussian or Lorentzian function, but certainly shows a peak with the narrowest peak width among the six epilayers.

5.4. Direct Comparison between PL Dark Spots and Etch Pits

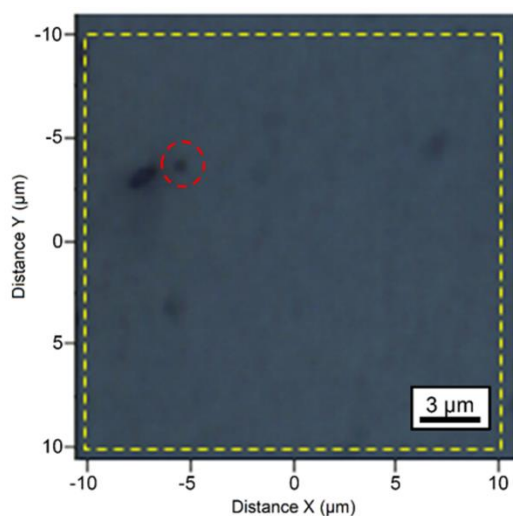


Figure 5.4: Optical image (under 100× objective lens) for sample 32607.

In order to further examine the possible correlation between the PL dark spots and the etch pits, we need to compare them in exactly the same area. To achieve this goal, we identified (with appropriate laser markers) a $20\mu\text{m}\times 20\mu\text{m}$ area, which is free of any apparent surface defects, on the epilayer with $N=8$ (sample #32607). In Figure 5.4, we show the optical image of this area after chemical etching. From this figure, although without high resolution, we are still able to observe some triangular etch pits. For instance, a etch pit is locating at the upper left part of the figure at approximately $(-5\mu\text{m}, -3.5\mu\text{m})$, as indicated by the red dotted circle on the graph. It should be noted that a much larger dark spot, centered at around $(-7\mu\text{m}, -3\mu\text{m})$ next to the just mentioned etch pit is actually not an etch pit. By comparing the optical image with the SEM image shown in Figure 5.5 (b), we see clearly that these two spots are of different origin.

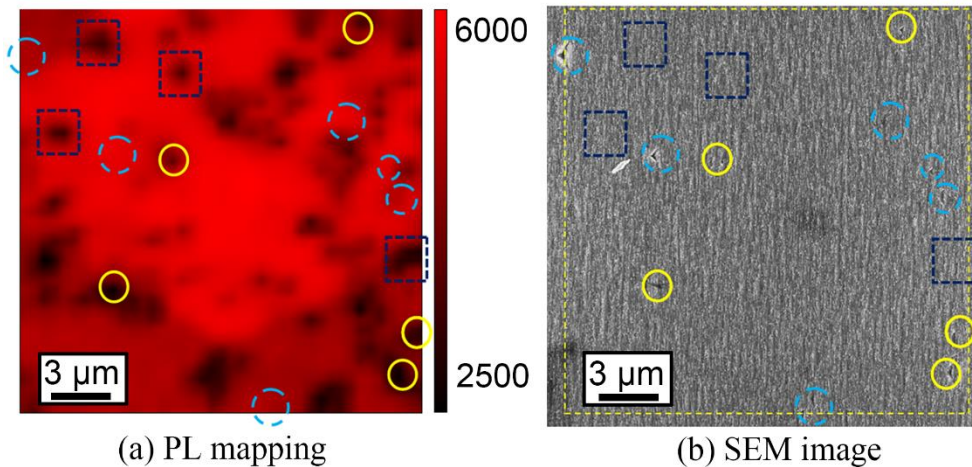


Figure 5.5: Comparison of PL intensity mapping (before etching) with SEM image (after etching) for sample 032607 ($N=8$). The area is the same one as shown in Figure 5.4.

Figure 5.5 is intended to present a direct comparison between the PL mapping results and the after-etching SEM image, which both were taken from the same area shown

in Figure 5.4. Note that in the SEM image shown in Figure 5.5 (b), the two darker regions, one near the center and the other at the lower left corner of the SEM image, were both due to unintended electron beam damage during the SEM image acquisition.

With the comparison of the PL and chemical etching results, we have unambiguously confirmed that the PL-DSD is substantially higher than the EPD, as found previously on the same sample but not the same area. The 11 etch pits counted in the SEM image within the PL mapping area yields an EPD $\sim 2.75 \times 10^6 \text{ cm}^{-2}$, which is somewhat higher than the value given in Table 5.1 (in Table 5.1, $\sim 0.77 \times 10^6 \text{ cm}^{-2}$). This difference is within a reasonable level, and could be attributed to the non-uniformity in the epilayer. On the other hand, the PL-DSD counted from the same area is $\sim 2.1 \times 10^7 \text{ cm}^{-2}$, which is much larger than the EPD. Thus, we may conclude that for the same area under examination, the PL-DSD will always be considerably larger than the EPD.

To further explore the relationship between the PL dark spot and etch pit, we try to correlate these two by comparing their locations shown in Figure 5.5 (a) and (b). When doing so, three scenarios were observed: (1) There is a clear match between an etch pit and a PL dark spot. Solid circles in both panel (a) and (b) are used to indicate the etch pits matched to PL dark spots, at the same locations (within the experimental accuracy of the PL scan). This indicates that some defects, which could possibly be assumed to dislocations, would result in low PL intensities. (2) Etch pits could not be clearly matched to any PL dark spot, even though the overall PL-DSD is significantly higher than EPD. Dotted circles are used to indicate such etch pits. The fact that a number of etch pits cannot be correlated to appropriate PL dark spots suggests that not all defects are equally detrimental to the photo-generated carriers. In fact, some of the defects could even be benign, thus they will

not lead to obvious intensity drops in the PL maps. In addition, the result also indicates that the PL method may not be able to reveal all the dislocation type defects, if it is assumed that all the etch pits are originated from dislocations. (3) PL dark spots do not show as etch pits: a number of PL dark spots have been resolved at locations that are free of etch pits. To prevent the figure from being too messy, we have only indicated some of these PL dark spots, by using dotted squares. One possibility of the excessive number of PL dark spots over the etch pits could be that there are other types of defects in the epilayer, which can manifest themselves in the PL map as dark spots. These defects may or may not be dislocations, but will definitely affect the device performance in PV or IR detection applications by causing non-radiative recombination of the photo-generated carriers.

Apparently more work is required to understand the implications of these results, such as using other techniques and making correlations. There are several techniques that would be helpful in further studies: for instance, structural characterization of an individual defect by using high resolution TEM and micro-Raman spectroscopy, in conjunction with laser beam induced current (LBIC) measurement, and so on. Nevertheless, the findings discussed in this chapter suggest that the PL method offers a much higher sensitivity than chemical etching. PL, as a result of carrier radiative recombination, is more powerful in identifying defects which have considerable influence on non-radiative recombination of photo-generated carriers, and thus harmful to the material's luminescence and transport process. Chemical etching, on the other hand, is a method merely reflects the structural quality, thus fail to show the same degree of relevance to the device performance as PL does.

5.5 Conclusions

In summary, we have used confocal μ -PL microscopy to study extended defects in CdTe epilayers grown on Si (211) substrates with different numbers of annealing cycles. In general, the PL mapping results show the similar trends as EPD and XRD linewidth, demonstrating that an increasing annealing number N will generally lead to lower defect densities. However, there are differences regarding the optimal annealing cycle for the three methods, for instance, $N_{\text{op-PL}} = 8$, compared to $N_{\text{op-XRD}} = 6$ and $N_{\text{op-EPD}} = 10$. Besides, a direct comparison between the etch pits (imaged by SEM) and PL dark spots on the same sample area have shown that (1) the PL-DSD is substantially higher than EPD, and (2) not all etch pits appear as dark spots in PL maps, and (3) there are some defects in the epilayers, although not shown as etch pits, also give rise to PL dark spots.

The results above show that μ -PL mapping in conjunction with statistical analysis provides an effective and non-destructive method to evaluate the extended defect density in a semiconductor epilayer, CdTe in particular. The findings also suggest that PL mapping is a more sensitive technique for revealing the extended defects that are actually detrimental to photo-generated carriers, in addition to the more apparent advantages of being non-invasive.

To further correlate the μ -PL mapping data to other characterizations, more work is required. By utilizing techniques such as reflectance, Raman, electroluminescence (EL), LBIC, HRTEM, a more comprehensive understanding of the material could be offered.

CHAPTER 6: CONCLUSIONS AND FUTURE WORK

6.1 Conclusions

In this dissertation work, we have successfully used micro-Raman spectroscopy to investigate the lattice vibration properties of the InAs/GaSb T2SLs and InAs/InAsSb T2SLs, which demonstrates strong ability in probing structural characteristics of III-V T2SLs. On the other hand, we have use micro-PL spectroscopy to conduct defect studies on CdTe epilayers, which demonstrates higher sensitivity in probing defects that are closely related to device performance.

6.1.1 Micro-Raman Study on Lattice Vibrations in InAs/GaSb T2SLs and InAs/ InAsSb T2SLs

For both InAs/GaSb T2SLs and InAs/InAsSb T2SLs, we have conducted a series of room temperature micro-Raman measurements using 532nm laser, with sufficiently low excitation power which prevents observable thermal effects. By using polarization analyses and comparing the SL spectra with spectra of related materials, we are able to make several important observations in each type of T2SLs.

In the InAs/GaSb T2SL, from the (110) or $(\bar{1}10)$ cleaved edge, we have observed at least five new Raman modes, which have been assigned as interface (IF), quasi-confined (QC), or extended (EX) mode, thus for the first time confirms the existence of these QC and EX phonon modes that have long been predicted in theory but never identified in experiments. These modes are: one EX-TO and one InAs QC-TO mode, with B_2 or B_1

symmetry; one EX-TO, one IF₁-TO, and a phonon-polariton TO mode associated with the GaSb QC-LO mode, all with A₁ symmetry. The phonon-polariton mode is observed to show apparent anisotropy between the (110) or ($\bar{1}10$) plane, which is expected for a structure with C_{2v} biaxial symmetry. All the other modes, on the other hand, behave as though having D_{2d} uniaxial symmetry, with no obvious anisotropy observed in Raman spectra. In addition, no predicted confined (C) mode has been observed, suggesting the need for an improved lattice dynamics theory. At the (001) plane, it is found that the major SL mode, which was previously referred to as SL LO mode, is more accurate to be assigned as a GaSb QC-LO mode. In addition, no obvious anisotropy between the [110] and [$\bar{1}10$] is observed.

These findings regarding lattice vibrations will provide valuable information for fundamental understanding of the material properties: for instance, the derived information about the electron-phonon coupling will be critical to assess the lately proposed quantum transport applications that are ultimately determined by the electron-phonon interaction [131,132].

In InAs/InAsSb T2SLs, we are also able to make several important observations. A LO and TO mode, resulting directly from InAs and InSb alloying is resolved from the (001) and (110) plane, respectively. These modes are red shifted with respect to the InAs LO or TO mode, and follows similar selection rules as the LO or TO mode in InAs bulk and InAsSb alloy. However, interesting new properties have been observed for these modes:

- (1) The mode frequency for these two modes are significantly larger than what would be expected from the respective alloy modes based on the literature data for InAsSb alloys.
- (2) an obvious mode intensity enhancement in the LO mode as compared to the bulk

material is observed, which could possibly be attributed to larger RC of InSb, but needs further work to confirm.

At the (001) plane, a new feature $\sim 239\text{cm}^{-1}$ is resolved, which could be directly correlated with delta Ga doping applied to one SL sample. This finding also demonstrates the ability of micro-Raman to probe fine structural variations in the SLs. On the other hand, at the (110) plane, no such correlation could be made.

Similar as the case of InAs/GaSb T2SL, in both InAs/InAsSb SLs and InAsSb alloys, we are able to resolve a mode with its frequency closer to that of the forbidden LO mode, at (110) plane, in polarization configuration $x'(y', y')\bar{x}'$ and $x'(z', z')\bar{x}'$. For SL, the appearance of this mode could be explained by the regular modulation along z' : those quantized or standing-wave phonon modes with $|k_z| = m\pi/d$ have net $k_z = 0$ and small $k_{[110]}$, thus the corresponding Raman scattering is induced. On the other hand, the similar phenomena in alloys could be explained by the disordering induced by alloy, rather than the regular modulation in the SL case. Consequently, the relative mode intensity in alloy is tend to be weaker than in SL. Also, we observe that in some SLs, the intensity of this mode is even stronger than the allowed TO mode, which is rather unusual.

Furthermore, we have also conducted a general spectra comparison between the InAs/GaSb T2SL and InAs/InAsSb T2SL. The most notable similarity between the two systems is the transverse counterpart of the corresponding LO mode, as mentioned in previous paragraphs. On the other hand, apparent differences are also observed. In (110) plane, two apparent differences are shown between the two systems: (1) In configuration $x'(y', y')\bar{x}'$, there is a SL EX mode resolved in the InAs/GaSb SL system, which could not be related to any confined or quasi-confined TO or LO mode of the constituent, with

the mode frequency could not be related to the existing mode of any constituent. On the other hand, no such mode is resolved in the InAs/InAsSb SL system. (2) In the InAs/GaSb SL system, the quasi-confined InAs TO mode (which is closely related to one of the SL's constituent) is only resolved in $x'(y', z')\bar{x}'$ and $x'(z', y')\bar{x}'$, but disappears in $x'(y', y')\bar{x}'$. This finding indicates an evident difference between $x'(y', y')\bar{x}'$ and the two cross configurations, for C_{2v} symmetry. On the other hand, the SL TO mode (which is closely related to the SL's constituent) is resolved in all the three allowed configurations, with similar mode intensities. This difference between the two SL systems is possibly attributed to the difference in symmetries of these two systems.

6.1.2 Micro-PL Study on Extended Defects in CdTe Epilayers

For the CdTe epilayers with relatively high defect density levels, we have used confocal micro-PL microscopy to study the behaviors of the extended defects in it and correlate the PL findings with other techniques. In general, the PL mapping results show similar trends as EPD and XRD linewidth, demonstrating that an increasing annealing number N will generally lead to lower defect densities. However, there are differences regarding the optimal annealing cycle for the three methods: for instance, $N_{\text{op-PL}}=8$, compared to $N_{\text{op-XRD}}=6$ and $N_{\text{op-EPD}}=10$.

Besides, a direct comparison between the etch pits (revealed by chemical etching and presumed to be dislocations) and PL dark spots on the same sample area have shown that (1) the PL-DSD is substantially higher than EPD, which possibly indicates a higher sensitivity of PL in probing defects that are actually detrimental to radiative recombination in the epilayer; (2) not all etch pits appear as dark spots in PL maps, which indicate benign behaviors of some defects during the radiative recombination process; and (3) there are

some of defects, which does not manifest itself as dislocations, but still have adverse impact on the luminescence process, and will eventually influence device performance.

6.2 Future Work

6.2.1 Micro-Raman Study on InAs/GaSb and InAs/InAsSb T2SLs

In the future, we intend to conduct Raman measurements to further explore the structural differences in the SLs. For instance, recall that we have been able to resolve a Raman feature directly related to Ga doping of specific type (in this work, delta Ga doping), which demonstrates the potential ability of Raman to probe fine structural differences. Thus, we are interested to further explore the variation in Raman spectra with respect to different types of structural differences in SL samples, such as different Ga doping, different interfacial treatment, and so on.

In this work, we are able to observe the anisotropy between $[110]$ and $[\bar{1}10]$, as well as that between (110) and $(\bar{1}10)$, by using micro-Raman. In the future, we would like to correlate the anisotropy shown in Raman with results of other techniques, such as TEM; and also explore the correlation between this anisotropy with material quality and/or device performance.

6.2.2 Micro-PL Study on Defects in Semiconductor Epilayers

In this work, micro-PL spectroscopy is majorly used for statistical analyses, which provide a general estimate on the defect densities relating closely to the non-radiative combination of photo-generated carriers. To obtain further understanding of the defect's behavior, it is necessary to correlate the PL results with other techniques, among which the light-beam-induced-current (LBIC) is the one we are mostly interested in, since the LBIC technique is also directly related to the recombination process of the photo-generated

carriers. As a further advantage, bias voltages could be applied in the LBIC process, which makes the corresponding result even more important in estimating the influence of defects on device performance.

When the defect density of the epilayers becomes sufficiently low, it is practical to conduct micro-PL study on single isolated defects, and working on theoretical models to describe the behaviors of defects, such as extracting the carrier diffusion length, and so on.

REFERENCES

- [1] C. V. Raman, *Indian J. Phys.* 2, 12 (1928).
- [2] C. D. Allred and R. L. McCreery, *Applied Spectroscopy* 44, 1229 (1990).
- [3] C. Eliasson, N. Macleod, and P. Matousek, *Analytical chemistry* 79, 8185 (2007).
- [4] A. Tokmakoff, M. Lang, D. Larsen, G. Fleming, V. Chernyak, and S. Mukamel, *Phys. Rev. Lett.* 79, 2702 (1997).
- [5] B. Stoicheff, *Canadian Journal of Physics* 35, 730 (1957).
- [6] B. P. Stoicheff, *Canadian Journal of Physics* 32, 339 (1954).
- [7] E. del Corro, H. Terrones, A. Elias, C. Fantini, S. Feng, M. A. Nguyen, T. E. Mallouk, M. Terrones, and M. A. Pimenta, *ACS Nano* 8, 9629 (2014).
- [8] J. Kash, J. Tsang, and J. Hvam, *Phys. Rev. Lett.* 54, 2151 (1985).
- [9] M. S. Dresselhaus, G. Dresselhaus, R. Saito, and A. Jorio, *Physics reports* 409, 47 (2005).
- [10] S. Klemmt et al., *Phys. Rev. Lett.* 114, 186403 (2015).
- [11] E. Honea, A. Ogura, D. Peale, C. Felix, C. Murray, K. Raghavachari, W. Sprenger, M. Jarrold, and W. Brown, *The Journal of chemical physics* 110, 12161 (1999).
- [12] J. Ferraro and K. Nakamoto, *Introductory Raman Spectroscopy* (Academic Press, 1994).
- [13] R. Loudon, *Adv. Phys.* 13, 423 (1964).
- [14] G. W. King, *Spectroscopy and molecular structure* (Holt, Rinehart and Winston, New York, 1964).
- [15] H. Eyring, J. Walter, and G. E. Kimball, *Quantum Chemistry* (John Wiley And Sons Inc., 1944).
- [16] B. P. Gaber, V. Miskowski, and T. G. Spiro, *Journal of the American Chemical Society* 96, 6868 (1974).
- [17] F. S. Parker, *Applications of Infrared, Raman, and Resonance Raman Spectroscopy in Biochemistry* (Springer, 1983), 1 edn.

- [18] P. Hildebrandt and M. Stockburger, *The Journal of Physical Chemistry* 88, 5935 (1984).
- [19] J. Hollas, *Modern Spectroscopy* (Wiley, 2004), 4 edn.
- [20] B. Reed, *Quantum Mechanics* (Jones & Bartlett Learning, 2007).
- [21] M. fox, *Optical Properties of Solids* (OUP Oxford, 2001), 2 nd edn.
- [22] S. Chou et al., *Phys. Rev. Lett.* 94, 127402 (2005).
- [23] L. Carlos, R. Sá Ferreira, R. Pereira, M. Assuncao, and V. de Zea Bermudez, *The Journal of Physical Chemistry B* 108, 14924 (2004).
- [24] T. Koida, S. Chichibu, A. Uedono, A. Tsukazaki, M. Kawasaki, T. Sota, Y. Segawa, and H. Koinuma, *Applied Physics Letters* 82, 532 (2003).
- [25] S. Ostapenko, I. Tarasov, J. Kalejs, C. Haessler, and E. Reisner, *Semiconductor science and technology* 15, 840 (2000).
- [26] J. Weber and M. I. Alonso, *Physical Review B* 40, 5683 (1989).
- [27] J. Wu, W. Walukiewicz, K. Yu, J. Ager Iii, E. Haller, H. Lu, W. J. Schaff, Y. Saito, and Y. Nanishi, *Applied Physics Letters* 80, 3967 (2002).
- [28] J. Brault, M. Gendry, G. Grenet, G. Hollinger, J. Olivares, B. Salem, T. Benyattou, and G. Bremond, *J. Appl. Phys.* 92, 506 (2002).
- [29] Z. M. Liao, H. Z. Zhang, Y. B. Zhou, J. Xu, J. M. Zhang, and D. P. Yu, *Physics Letters A* 372, 4505 (2008).
- [30] D. Bavykin, E. Savinov, and V. Parmon, *Langmuir* 15, 4722 (1999).
- [31] V. E. Borisenko, *Physics, Chemistry and Application of Nanostructures: Review and Short Notes to Nanomeeting '99 : Minsk, Belarus 17-21 May 1999* (World Scientific, 1999).
- [32] H. Kroemer, *Physica E* 20, 196 (2004).
- [33] H. Sakaki, L. L. Chang, R. Ludeke, C. A. Chang, G. A. Saihalasz, and L. Esaki, *Appl. Phys. Lett.* 31, 211 (1977).
- [34] W. R. Frensley and H. Kroemer, *Phys. Rev. B* 16, 2642 (1977).
- [35] W. A. Harrison, *Journal of Vacuum Science & Technology* 14, 1016 (1977).

- [36] A. Sood, J. Menendez, M. Cardona, and K. Ploog, *Phys Rev Lett* 54, 2115 (1985).
- [37] Z. Popović, M. Cardona, E. Richter, D. Strauch, L. Tapfer, and K. Ploog, *Phys. Rev. B* 41, 5904 (1990).
- [38] I. Sela, L. A. Samoska, C. R. Bolognesi, A. C. Gossard, and H. Kroemer, *Phys. Rev. B* 46, 7200 (1992).
- [39] P. Castrillo, G. Armelles, and J. Barbolla, *Solid State Commun.* 98, 307 (1996).
- [40] S. Adachi, *GaAs and Related Materials: Bulk Semiconducting and Superlattice Properties* (World Scientific, 1994).
- [41] J. L. T. Waugh and G. Dolling, *Physical Review* 132, 2410 (1963).
- [42] *In Group IV Elements, IV-IV and III-V Compounds. Part a - Lattice Properties*, edited by O. Madelung, U. Rössler, and M. Schulz (Springer Berlin Heidelberg, 2001), pp. 1.
- [43] R. Carles, N. Saintericq, J. B. Renucci, M. A. Renucci, and A. Zwick, *Phys. Rev. B* 22, 4804 (1980).
- [44] M. K. Farr, J. G. Traylor, and S. K. Sinha, *Phys. Rev. B* 11, 1587 (1975).
- [45] S. G. Lyapin, P. C. Klipstein, N. J. Mason, and P. J. Walker, *Phys Rev Lett* 74, 3285 (1995).
- [46] D. Berdekas and G. Kanellis, *Phys. Rev. B* 43, 9976 (1991).
- [47] A. Fasolino, E. Molinari, and J. C. Maan, *Phys. Rev. B* 33, 8889 (1986).
- [48] J. Wang and Y. Zhang, *J. Appl. Phys.* 116, 214301 (2014).
- [49] D. Smith and C. Mailhot, *J. Appl. Phys.* 62, 2545 (1987).
- [50] E. A. Plis, *Advances in Electronics* 2014 (2014).
- [51] C. H. Grein, P. M. Young, M. E. Flatte, and H. Ehrenreich, *J. Appl. Phys.* 78, 7143 (1995).
- [52] Y. Wei, A. Gin, M. Razeghi, and G. J. Brown, *Appl. Phys. Lett.* 80, 3262 (2002).
- [53] C. Cervera, I. Ribet-Mohamed, R. Taalat, J. P. Perez, P. Christol, and J. B. Rodriguez, *Journal of Elec Materi* 41, 2714 (2012).
- [54] B.M. Nguyen, D. Hoffman, P.Y. Delaunay, and M. Razeghi, *Appl. Phys. Lett.* 91,

- 163511 (2007).
- [55] Y. Naveh and B. Laikhtman, *Phys Rev Lett* 77, 900 (1996).
- [56] D. I. Pikulin and T. Hyart, *Phys Rev Lett* 112, 176403 (2014).
- [57] C. Liu, T. L. Hughes, X.-L. Qi, K. Wang, and S.-C. Zhang, *Phys Rev Lett* 100, 236601 (2008).
- [58] W. Pan, J. F. Klem, J. K. Kim, M. Thalakulam, M. J. Cich, and S. K. Lyo, *Appl. Phys. Lett.* 102, 033504 (2013).
- [59] K. Suzuki, Y. Harada, K. Onomitsu, and K. Muraki, *Phys. Rev. B* 87, 235311 (2013).
- [60] I. Knez, C. T. Rettner, S.-H. Yang, S. S. P. Parkin, L. Du, R.-R. Du, and G. Sullivan, *Physical Review Letters* 112, 026602 (2014).
- [61] P. C. Klipstein, *Phys. Rev. B* 91, 035310 (2015).
- [62] J. B. Khurgin and I. Vurgaftman, *Appl. Phys. Lett.* 104 (2014).
- [63] A. Fasolino, E. Molinari, and J. C. Maan, *Superlattices Microstruct.* 3, 117 (1987).
- [64] A. Fasolino, E. Molinari, and J. C. Maan, *Phys. Rev. B* 39, 3923 (1989).
- [65] J. Menéndez, *J. Lumines.* 44, 285 (1989).
- [66] C. Lopez, R. J. Springett, R. J. Nicholas, P. J. Walker, N. J. Mason, and W. Hayes, *Surf. Sci.* 267, 176 (1992).
- [67] J. R. Waterman, B. V. Shanabrook, R. J. Wagner, M. J. Yang, J. L. Davis, and J. P. Omaggio, *Semicond. Sci. Technol.* 8, S106 (1993).
- [68] M. Inoue, M. Yano, H. Furuse, N. Nasu, and Y. Iwai, *Semicond. Sci. Technol.* 8, S121 (1993).
- [69] D. Behr, J. Wagner, J. Schmitz, N. Herres, J. D. Ralston, P. Koidl, M. Ramsteiner, L. Schrottke, and G. Jungk, *Appl. Phys. Lett.* 65, 2972 (1994).
- [70] N. Herres, F. Fuchs, J. Schmitz, K. M. Pavlov, J. Wagner, J. D. Ralston, P. Koidl, C. Gadaleta, and G. Scamarcio, *Phys. Rev. B* 53, 15688 (1996).
- [71] L. G. Li, S. M. Liu, S. Luo, T. Yang, L. J. Wang, F. Q. Liu, X. L. Ye, B. Xu, and Z. G. Wang, *Nanoscale Res. Lett.* 7, 1, 160 (2012).
- [72] P. C. Klipstein, Y. Livneh, A. Glozman, S. Grossman, O. Klin, N. Snapi, and E. Weiss,

- Journal of Elec Materi 43, 2984 (2014).
- [73] D. Zuo et al., *Appl. Phys. Lett.* 106, 071107 (2015).
- [74] S. P. Svensson, D. Donetsky, D. Wang, H. Hier, F. J. Crowne, and G. Belenky, *J. Cryst. Growth* 334, 103 (2011).
- [75] Y. Li, S. Dosanjh, I. Ferguson, A. Norman, A. De Oliveira, R. Stradling, and R. Zallen, *Semiconductor science and technology* 7, 567 (1992).
- [76] Y. T. Cherng, K. Y. Ma, and G. B. Stringfellow, *Applied Physics Letters* 53, 886 (1988).
- [77] P. Galtier, J. Chevallier, M. Zigone, and G. Martinez, *Physical Review B* 30, 726 (1984).
- [78] V. S. Gorelik, R. N. Khashimov, and A. P. Vidanov, *Soviet Physics Semiconductors-Ussr* 18, 879 (1984).
- [79] Y. T. Cherng, M. J. Jou, H. R. Jen, and G. B. Stringfellow, *Journal of Applied Physics* 63, 5444 (1988).
- [80] K. Kakimoto and T. Katoda, *Applied Physics Letters* 40, 826 (1982).
- [81] R. Carles, N. Saintericq, A. Zwick, M. A. Renucci, and J. B. Renucci, *Journal De Physique* 42, 105 (1981).
- [82] A. Rohatgi, S. A. Ringel, R. Sudharsanan, P. V. Meyers, C. H. Liu, and V. Ramanathan, *Solar Cells* 27, 219 (1989).
- [83] A. Bosio, N. Romeo, S. Mazzamuto, and V. Canevari, *Progress in Crystal Growth and Characterization of Materials* 52, 247 (2006).
- [84] A. Romeo, M. Terheggen, D. Abou-Ras, D. Batzner, F. Haug, M. Kalin, D. Rudmann, and A. Tiwari, *Progress in photovoltaics* 12, 93 (2004).
- [85] T. Chu, S. S. Chu, C. Ferekides, C. Wu, J. Britt, and C. Wang, *J. Appl. Phys.* 70, 7608 (1991).
- [86] X. Wu, *Solar energy* 77, 803 (2004).
- [87] K. Chopra, P. Paulson, and V. Dutta, *Progress in Photovoltaics* 12, 69 (2004).
- [88] FIRST SOLAR BUILDS THE HIGHEST EFFICIENCY THIN FILM PV CELL ON RECORD, <http://investor.firstsolar.com/releasedetail.cfm?ReleaseID=864426>.
- [89] P.Y. Su, R. Dahal, G.C. Wang, S. Zhang, T.M. Lu, and I. Bhat, *J. Electron. Mater.* 44,

- 3118 (2015).
- [90] R. Zia, F. Saleemi, S. Naseem, and Z. Kayani, *Energy Reports* 1, 58 (2015).
- [91] R. Sporcken, S. Sivananthan, K. Mahavadi, G. Monfroy, M. Boukerche, and J. Faurie, *Appl. Phys. Lett.* 55, 1879 (1989).
- [92] J. Cheung and T. Magee, *Journal of Vacuum Science & Technology A* 1, 1604 (1983).
- [93] R. Korenstein, P. Madison, and P. Hallock, *Journal of Vacuum Science & Technology B* 10, 1370 (1992).
- [94] R. N. Bicknell, R. W. Yanka, N. C. Giles, J. F. Schetzina, T. J. Magee, C. Leung, and H. Kawayoshi, *Appl. Phys. Lett.* 44, 313 (1984).
- [95] D. Smith, T. McGill, and J. Schulman, *Appl. Phys. Lett.* 43, 180 (1983).
- [96] W. Akutagawa, K. Zanio, and J. Mayer, *Nuclear Instruments and Methods* 55, 383 (1967).
- [97] M. Richter and P. Siffert, *Nuclear Instruments and Methods in Physics Research Section A: Accelerators, Spectrometers, Detectors and Associated Equipment* 322, 529 (1992).
- [98] M. Fiederle, T. Feltgen, J. Meinhardt, M. Rogalla, and K. Benz, *J. Cryst. Growth* 197, 635 (1999).
- [99] Y. Eisen and A. Shor, *J. Cryst. Growth* 184, 1302 (1998).
- [100] B. Zhang et al., *Nano Letters* 15, 4381 (2015).
- [101] T. H. Gfroerer, C. M. Crowley, C. M. Read, and M. W. Wanlass, *J. Appl. Phys.* 111, 4, 093712 (2012).
- [102] M.W. Chu, I. Szafraniak, R. Scholz, C. Harnagea, D. Hesse, M. Alexe, and U. Gösele, *Nature materials* 3, 87 (2004).
- [103] G. Eneman, E. Simoen, R. Delhougne, P. Verheyen, R. Loo, and K. De Meyer, *Appl. Phys. Lett.* 87, 2112 (2005).
- [104] Y. Chen, S. Farrell, G. Brill, P. Wijewarnasuriya, and N. Dhar, *J. Cryst. Growth* 310, 5303 (2008).
- [105] Y. Yan, M. M. Al-Jassim, and K. M. Jones, *Thin Solid Films* 389, 75 (2001).
- [106] Z. C. Feng, A. Mascarenhas, and W. J. Choyke, *Journal of Luminescence* 35, 329

(1986).

- [107] C. B. Davis, D. D. Allred, A. Reyesmena, J. Gonzalezhernandez, O. Gonzalez, B. C. Hess, and W. P. Allred, *Phys. Rev. B* 47, 13363 (1993).
- [108] C. R. Corwine, J. R. Sites, T. A. Gessert, W. K. Metzger, P. Dippo, J. Li, A. Duda, and G. Teeter, *Appl. Phys. Lett.* 86, 3, 221909 (2005).
- [109] V. Consonni, G. Feuillet, and S. Renet, *J. Appl. Phys.* 99, 3502 (2006).
- [110] A. Gukasyan, A. Kvit, Y. Klevkov, and S. Oktyabrsky, *Solid State Communications* 97, 897 (1996).
- [111] B. Fluegel, K. Alberi, M. J. DiNezza, S. Liu, Y. H. Zhang, and A. Mascarenhas, *Physical Review Applied* 2, 034010 (2014).
- [112] F. S. d'Aragona, *Journal of the Electrochemical Society* 119, 948 (1972).
- [113] T. Kozawa, T. Kachi, T. Ohwaki, Y. Taga, N. Koide, and M. Koike, *Journal of the Electrochemical Society* 143, L17 (1996).
- [114] Y. Gaillard, C. Tromas, and J. Woiregard, *Acta materialia* 51, 1059 (2003).
- [115] T. H. Gfroerer, Y. Zhang, and M. W. Wanlass, *Appl. Phys. Lett.* 102, 4, 012114 (2013).
- [116] F. Chen, Y. Zhang, T. H. Gfroerer, A. N. Finger, and M. W. Wanlass, in *Photovoltaic Specialists Conference (PVSC), 2013 IEEE 39th* (2013), pp. 1402.
- [117] Y. Huang et al., *Appl. Phys. Lett.* 99, 3, 011109 (2011).
- [118] D. Zuo, P. F. Qiao, D. Wasserman, and S. L. Chuang, *Appl. Phys. Lett.* 102, 4, 141107 (2013).
- [119] Y. Chen, G. Brill, and N. Dhar, *J. Cryst. Growth* 252, 270 (2003).
- [120] M. Minsky, *Scanning* 10, 11 (1988).
- [121] <http://www.horiba.com/us/en/scientific/products/raman-spectroscopy/raman-academy/raman-faqs/what-is-the-spatial-resolution-of-a-raman-microscope/>.
- [122] R. Borroff, R. Merlin, A. Chin, and P. K. Bhattacharya, *Appl. Phys. Lett.* 53, 1652 (1988).
- [123] Y. B. Li, V. Tsoukala, R. A. Stradling, R. L. Williams, S. J. Chung, I. Kamiya, and A. G. Norman, *Semicond. Sci. Technol.* 8, 2205 (1993).

- [124] M. B. S. W. K. Liu, *Thin Films: Heteroepitaxial Systems* (World Scientific, 1999), p. 424.
- [125] C. E. M. Campos and P. S. Pizani, *Appl. Surf. Sci.* 200, 111 (2002).
- [126] P. Yu and M. Cardona, *Fundamentals of Semiconductors* (Springer, 2010), 4th ed.
- [127] T. Sekine, K. Uchinokura, and E. Matsuura, *Solid State Commun.* 18, 1337 (1976).
- [128] B. Jusserand, P. Voisin, M. Voos, L. L. Chang, E. E. Mendez, and L. Esaki, *Appl. Phys. Lett.* 46, 678 (1985).
- [129] M. J. Yang, R. J. Wagner, B. V. Shanabrook, W. J. Moore, J. R. Waterman, C. H. Yang, and M. Fatemi, *Appl. Phys. Lett.* 63, 3434 (1993).
- [130] A. Fainstein, P. Etchegoin, M. P. Chamberlain, M. Cardona, K. Totemeyer, and K. Eberl, *Phys. Rev. B* 51, 14448 (1995).
- [131] F. Rossi and T. Kuhn, *Reviews of Modern Physics* 74, 895 (2002).
- [132] A. Thränhardt, S. Kuckenburg, A. Knorr, T. Meier, and S. W. Koch, *Phys. Rev. B* 62, 2706 (2000).
- [133] M. O. Manasreh, *Antimonide-Related Strained-Layer Heterostructures* (CRC Press, 1997).
- [134] R. Hessmer, A. Huber, T. Egeler, M. Haines, G. Trankle, G. Weimann, and G. Abstreiter, *Phys. Rev. B* 46, 4071 (1992).
- [135] F. Cerdeira, A. Pinczuk, J. C. Bean, B. Batlogg, and B. A. Wilson, *Applied Physics Letters* 45, 1138 (1984).
- [136] N. C. Gilestaylor, R. N. Bicknell, D. K. Blanks, T. H. Myers, and J. F. Schetzina, *J. Vac. Sci. Technol. A-Vac. Surf. Films* 3, 76 (1985).
- [137] W. J. Everson, C. K. Ard, J. L. Sepich, B. E. Dean, G. T. Neugebauer, and H. F. Schaake, *J. Electron. Mater.* 24, 505 (1995).

APPENDIX: LIST OF PUBLICATIONS AND PRESENTATIONS

- [1] Henan Liu, Naili Yue, Yong Zhang, Pengfei Qiao, Daniel Zuo, Ben Kesler, Shun Lien Chuang, Jae-Hyun Ryou, James D. Justice, and Russell Dupuis, Lattice vibration modes in type-II superlattice InAs/GaSb with no-common-atom interface and overlapping vibration spectra, *Phys. Rev. B* 91, 235317 (2015).
- [2] Henan Liu, Yong Zhang, Yuanping Chen and Priyalal S. Wijewarnasuriya, Confocal micro-PL mapping of defects in CdTe epilayers grown on Si (211) substrates with different annealing cycles, *J. Electron. Mat.* 43, 2854 (2014).
- [3] Bingpo Zhang, Ping Lu, Henan Liu, Lin Jiao, Zhenyu Ye, M. Jaime, F.F. Balakirev, Huiqiu Yuan, Huizhen Wu, Wei Pan, and Yong Zhang, Quantum Oscillations in a Two-Dimensional Electron Gas at the Rocksalt/Zincblende Interface of PbTe/CdTe (111) Heterostructures, *Nano Lett.* (2015).
- [4] Henan Liu, Qiong Chen, Hui-Seon Kim, Nam-Gyu Park, and Yong Zhang, Effects of domain size in polycrystalline perovskite organic-inorganic hybrids investigated by spatially resolved optical spectroscopy, 42th IEEE Photovoltaic Specialists Conference (Orleans, 2015). (accepted)
- [5] Henan Liu, Naili Yue, Yong Zhang, Pengfei Qiao, Daniel Zuo, Ben Kesler, Shun Lien Chuang, Jae-Hyun Ryou, James D. Justice, Russell Dupuis and Amy Liu. Superlattice modes in InAs/GaSb type II superlattices investigated by cleaved edge polarized micro-Raman measurements. ICSNN 2014 Meeting.
- [6] Henan Liu, Yong Zhang, Shun Lien Chuang, Russell Dupuis and Amy Liu. Micro-Raman study of InAs/GaSb superlattices from front and cleaved edge. APS 2013 March Meeting.